# Advanced Technologies for Nuclear Emergency Response

Lead Guest Editor: Sheng Fang
Guest Editors: Denis Quélo, Jiangang Zhang, and Yongsheng Ling

# Advanced Technologies for Nuclear Emergency Response

# Advanced Technologies for Nuclear Emergency Response

Lead Guest Editor: Sheng Fang
Guest Editors: Denis Quélo, Jiangang Zhang, and Yongsheng Ling

# Contents

*Research Article*

# Study on Probabilistic Safety Goals for Multimodule High-Temperature Gas-Cooled Reactor Based on Chinese Societal Risks

**Jinghan Zhang** (ID)**, Jun Zhao** (ID)**, and Jiejuan Tong** (ID)

*Tsinghua University, Institute of Nuclear and New Energy Technology, Beijing 100084, China*

Correspondence should be addressed to Jiejuan Tong; tongjj@mail.tsinghua.edu.cn

Nuclear safety goal is the basic standard for limiting the operational risks of nuclear power plants. The statistics of societal risks are the basis for nuclear safety goals. Core damage frequency (CDF) and large early release frequency (LERF) are typical probabilistic safety goals that are used in the regulation of water-cooled reactors currently. In fact, Chinese current probabilistic safety goals refer to the Nuclear Regulatory Commission (NRC) and the International Atomic Energy Agency (IAEA), and they are not based on Chinese societal risks. And the CDF and LERF proposed for water reactor are not suitable for high-temperature gas-cooled reactors (HTGR), because the design of HTGR is very different from that of water reactor. And current nuclear safety goals are established for single reactor rather than unit or site. Therefore, in this paper, the development of the safety goal of NRC was investigated firstly; then, the societal risks in China were investigated in order to establish the correlation between the probabilistic safety goal of multimodule HTGR and Chinese societal risks. In the end, some other matters about multireactor site were discussed in detail.

## 1. Introduction

Nuclear energy is a special kind of energy source with many advantages and it is conducive to solving the energy crisis [1]. However, a large amount of radioactive materials will be produced when using nuclear energy, and they seriously threaten the surroundings. So far, there have been three major nuclear accidents in the world: the Three Mile Island nuclear accident in the United States, the Chernobyl nuclear accident in the former Soviet Union, and the Fukushima nuclear accident in Japan. Each nuclear accident seriously damaged human health and the surrounding environment [2]. Due to the adverse effects of a nuclear accident, we need to ensure the safe design, safe construction, and safe operation of nuclear power plants to reassure the public's concerns and doubts.

Nuclear safety goals are set to control the severity of the adverse effects on the public and environment when nuclear power plants are in operation or accidents occur. On the one

hand, the safety goals can be used to guide the design, operation, and management of nuclear power plants, to establish a set of effective protection measures in nuclear power plants to protect personnel, society, and the environment from radioactive hazards. On the other hand, reasonable safety goals can promote public understanding of the safety of nuclear energy and have a positive impact on the development of nuclear energy. In order to promote the realization of nuclear safety goals and to make the safety goals more applicable in the actual design and management of nuclear power plants, the subsidiary numerical safety goals are always defined and used as surrogate safety goals for qualitative and quantitative safety goals. Core damage frequency (CDF) and large early release frequency (LERF) are the typical probabilistic safety goals that are used to evaluate the safety of water-cooled reactors [3].

The modular pebble-bed high-temperature gas-cooled reactor (HTR-PM) is in the construction in China as a demonstration project. It includes one turbine and two

reactors, and two reactors are used to drive one turbine [4]. The typical CDF and LERF which has been developed based on the characteristics of water-cooled reactors are not applicable to HTR-PM due to the unique design concept of high-temperature reactor (HTR). The most important difference is that core damage will not happen in the HTR. Therefore, the probabilistic safety goal of HTR-PM has been reestablished by China National Nuclear Safety Administration (NNSA); that is, "the cumulative frequency of all beyond design basis accident sequences that lead to off-site (including plant boundary) personal effective dose exceeding 50 mSv shall be less than $10^{-6}/(r \cdot y)$." It should be noted that this safety goal is dedicated to HTR-PM project and it is focused on single reactor rather than unit (two reactors and one turbine). In order to promote the development of multimodule HTGR, the probabilistic safety goal based on the "unit" or "plant" must be studied.

According to the method of nuclear safety goal formulation, the societal risks statistics are the basis for nuclear safety goals. At present, the probabilistic safety goals (CDF and LERF) of Chinese nuclear power plants refer to the American nuclear safety goals, which are based on the societal risks of the United States rather than the societal risks of China. Therefore, it is necessary to investigate Chinese societal risks based on the mortality rate of statistical data to provide a basis for the probabilistic safety goals of multimodule HTGR.

This paper aims to study the probabilistic safety goals of multimodule HTGR to support the probabilistic safety assessment of high-temperature gas-cooled reactors. In Section 2, the existing nuclear safety goals in the International Atomic Energy Agency (IAEA), the United States Nuclear Regulatory Commission (NRC), and China have been investigated to provide technical references for verifying the value of the probabilistic safety goals of HTGR. And the formulation and evolution of United States National Nuclear Regulatory Commission (USNRC) has been studied in order to guide the development of probabilistic safety goals of multimodule HTGR. In Section 3, the societal risks in China and other countries have been investigated in detail to provide the basis for determining the value of the probabilistic safety goals of multimodule HTGR. In Section 4, the key aspects of development of probabilistic safety goals of multimodule HTGR have been studied, and the correlation between the probabilistic safety goals and Chinese societal risks has been established. The last section is the discussion and conclusion.

## 2. Evolution of Safety Goals

### 2.1. Overview of Existing Safety Goals.

In a report published by the Organization for Economic Cooperation and Development/Nuclear Energy, probabilistic safety goals include the following four categories: core damage frequency (CDF); release frequencies, such as large release frequency (LRF) and large early release frequency (LERF); frequency of doses; and criteria on containment failure frequency (CFF) [3]. At present, many countries or organizations have formulated the probabilistic safety goals, including International Atomic

Energy Agency (IAEA) [5], US Nuclear Users Request Documentation (URD) [6], European Utility Requirement (EUR) [7], and European Pressurized Reactor (EPR) [8].

In this section, the probabilistic safety goals in IAEA, the US, and China were introduced, and the comparisons between the nuclear safety goals in China and the US were given.

(1) IAEA adopted the probabilistic safety goals of the US directly after the Chernobyl nuclear accident in 1986. During 1988–2001, IAEA issued INSAG-3, INSAG-12, NS-G-1, and NS-G-1.2 for nuclear safety goals [9–12]. Current probabilistic safety goals of IAEA are as follows: for existing reactors, $CDF < 10^{-4}/(\text{reactor} \cdot \text{year})$ $(\text{reactor} \cdot \text{year}, \ r \cdot y)$, $LERF < 10^{-5}/(r \cdot y)$; for new reactors, $CDF < 10^{-5}/(r \cdot y)$, eliminate radioactive large release practically that require early off-site emergency response.

(2) The US is the first to quantify nuclear safety goals and combine deterministic theory and probabilistic theory in the study of technical safety goals. In 1986, Nuclear Regulatory Commission (NRC) issued the final nuclear power plant safety goals policy statement, which determined qualitative safety goals, quantitative safety goals, and subsidiary safety goals [13–15]. Current probabilistic safety goals of the US are as follows: for existing reactors, $CDF < 10^{-4}/(r \cdot y)$, $LERF < 10^{-5}/(r \cdot y)$.

(3) Chinese nuclear safety goals mainly refer to the nuclear safety goals of US and IAEA. Many laws and regulations have been issued in China, including HAF 102–1991, HAF102-2004, HAD102/17–2006, the 12th Five-Year Plan for Nuclear Safety, HAF102-2016, and the 12th Five-Year Plan for Nuclear Safety [16–19]. Current probabilistic safety goals in China are as follows: for existing reactors, $CDF < 10^{-4}/(r \cdot y)$, $LERF < 10^{-5}/(r \cdot y)$; for new reactors, $CDF < 10^{-5}/(r \cdot y)$, $LERF < 10^{-6}/(r \cdot y)$.

The nuclear safety goal systems in China and the United States are shown in Figure 1. We compared the nuclear safety goals of China and the US from protection and prevention, qualitative safety goal, quantitative safety goal, and subsidiary safety goal. In fact, there is no specific quantitative safety goal in China.

### 2.2. Probabilistic Safety Goals of NRC.

In this section, the evolution of safety goals of NRC was investigated, including the relationship between CDF and LERF with quantitative health objective (QHO).

### 2.2.1. Overview of Probabilistic Safety Goals of NRC.

In 1979, the Three Mile Island nuclear accident occurred in the United States. After the accident, the proposal of establishing nuclear power reactor quantitative safety goals and perfecting safety principles was put forward. In 1980, the NRC issued a response to set nuclear safety goals. In 1981, the
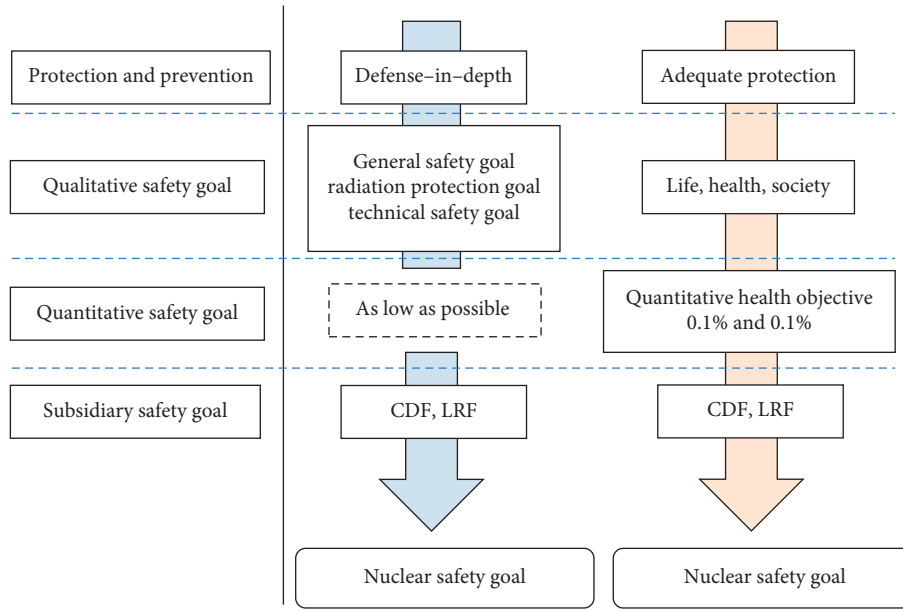
FIGURE 1: Nuclear safety goal systems in China and the United States.

NRC formulated a draft nuclear safety goals policy statement based on the results of expert seminars [13]. In 1983, the NRC issued a formal nuclear safety goals policy statement based on the results of discussions in various industries [14]. In 1986, the NRC issued a final nuclear safety goals policy statement and provided two qualitative safety goals and two quantitative safety goals [15].

Individual qualitative safety goal (IQSG) means prompt fatalities risks to an average individual in the vicinity of a nuclear power plant caused by reactor accidents. Societal qualitative safety goal (SQSG) means cancer fatalities to the population in the area of a nuclear power plant caused by nuclear power plant operation. Because the qualitative safety goal cannot be used to guide the design and operation of nuclear power plant (NPP), two quantitative safety goals have been proposed based on the two 0.1% rule, which include early quantitative health objective (EQHO) and latent quantitative health objective (LQHO). The EQHO and LQHO have been derived from the societal risk of America; that is, the risk to residents of NPP cannot exceed other existing societal risks obviously; this is the so-called "two 0.1% rule." The risk to the average individual in the vicinity of a nuclear power plant of prompt fatalities that might result from reactor accidents should not exceed 0.1% of the sum of prompt fatality risks resulting from other accidents to which members of the US population are generally exposed. The risk to the population in the area near a nuclear power plant of cancer fatalities that might result from nuclear power plant operation should not exceed 0.1% of the sum of cancer fatality risks resulting from all other causes [15].

CDF and LERF as subsidiary safety goals used to be surrogate safety goals of LQHO and EQHO, respectively, since the applicability of quantitative safety goals is still poor. The unit of CDF and LERF is per reactor year (r·y). The unit of the individual fatality risk is per year ($y$). Based on the later assessments of the sites, surrounding environment, and demographic conditions of nuclear power plants in the US, CDF $< 10^{-4}/(r \cdot y)$ and LERF $< 10^{-5}/(r \cdot y)$ meet the 0.1% and 0.1% quantitative safety goals. The relationship among nuclear safety goals in the US is shown in Figure 2. The quantitative safety goals (IQSG and SQSG) mean that the operation of nuclear power plants will not cause obvious additional risks to the life and health of the public. Qualitative safety goals (EQHO and LQHO) are measured/achieved through quantitative safety goals. Subsidiary safety goals (LERF and CDF) make quantitative safety goals more specific and easier to implement.

### 2.2.2. LERF and EQHO [20].

LERF $< 10^{-5}/(r \cdot y)$ is a subsidiary goal of early quantitative health objectives (EQHO) for early prompt fatalities. The rationality of substituting LERF for EQHO is demonstrated as follows.

According to the data survey for nuclear safety goals, the individual risk of prompt fatality caused by all other accidents is $5 \times 10^{-4}/y$ in the US. These accidents include traffic accidents, production accidents, and other accidents. According to the 0.1% in the early quantitative health objective (EQHO), the individual early risk (IER$_{EQHO}$) caused by nuclear power plant accidents need to be less than $5 \times 10^{-7}/(r \cdot y)$. The vicinity of a nuclear power plant means an extension of 1 mile from the boundary of the nuclear power plant. Individual early risk (IER) is

$$\text{IER} = \sum_{1}^{M} \frac{(\text{EF}_m * \text{LERF}_m)}{\text{TP}(1)}, \qquad (1)$$

where $\text{EF}_m$ is the number of early prompt fatalities within 1 mile caused by accident sequence $m$; $\text{LERF}_m$ is the frequency of fatal early large release caused by accident sequence $m$; and $\text{TP}(1)$ is the total population within 1 mile of the nuclear power plant.

Figure 2: The relationship among nuclear safety goals in the US.

Then, in the population $TP(1)$, the number of early prompt fatalities caused by accident sequence $m$ is given by

$$EF_m = CPEF_m * TP(1). \qquad (2)$$

$CPEF_m$ is the conditional probability of early prompt fatalities caused by accident sequence $m$, meaning the conditional probability of one person's early fatality caused by a radioactive release nuclear accident.

According to formulae (1) and (2), the individual early prompt fatality risk is

$$IER = \sum_{1}^{M} CPEF_m * LERF_m. \qquad (3)$$
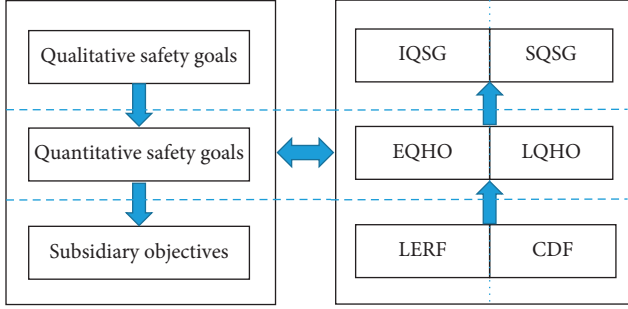
Suppose a worst accident sequence $m$, which has the greatest impact on early prompt fatalities risk. This accident sequence $m$ corresponds to a large break in the containment, and an unscrubbed release occurred before the surrounding population were effectively evacuated. According to the Surry PRA in NUREG-1150, the CPEF of the worst accident sequence is $3 \times 10^{-2}$.

Put $CPEF = 3 \times 10^{-2}$ and the safety goal value $LERF = 1 \times 10^{-5}/(r \cdot y)$ into formula (3). Then, when the worst accident sequence $m$ occurs, the individual early prompt fatality risk is

$$\begin{aligned} IER_m &= \left(3 \times 10^{-2}\right) \times \left(10^{-5}\right) = 3 \times 10^{-7}/(r \cdot y) < IER_{EQHO} \\ &= 5 \times 10^{-7}/(r \cdot y). \end{aligned}$$
$$(4)$$

Therefore, using $LERF < 10^{-5}/(r \cdot y)$ as a subsidiary goal of early quantitative health objectives (EQHO) for early prompt fatalities is acceptable.

2.2.3. CDF and QHO [20]. $CDF < 10^{-4}/(r \cdot y)$ is a subsidiary goal of latent quantitative health objectives (LQHO) for latent cancer fatalities. The rationality of substituting CDF for LQHO is demonstrated as follows.

According to the data survey for nuclear safety goals, the individual risk of cancer fatality from all other causes is $2 \times 10^{-3}/y$ in the US. According to the 0.1% in the latent quantitative health objective (LQHO), the individual latent risk ($ILR_{LQHO}$) caused by nuclear power plant operations need to be less than $2 \times 10^{-6}/(r \cdot y)$. The area of a nuclear power plant means an extension of 10 mile from the boundary of the nuclear power plant. Individual latent risk (ILR) is

$$ILR = \sum_{1}^{N} \frac{(LF_n * LLRF_n)}{TP(10)}, \qquad (5)$$

where $LF_n$ is the number of latent cancer fatalities within 10 miles caused by accident sequence $n$; $LLRF_n$ is the frequency of cancerogenic off-site individual doses caused by accident sequence $n$; and $TP(10)$ is the total population within 10 miles of the nuclear power plant.

Then, in the population $TP(10)$, the number of latent cancer fatalities caused by accident sequence $n$ is given by

$$LF_n = CPLF_n * TP(10), \qquad (6)$$

where $CPLF_n$ is the conditional probability of latent cancer fatalities caused by accident sequence $n$.

According to formulae (5) and (6), the individual latent cancer risk is

$$ILR = \sum_{1}^{N} CPLF_n * LLRF_n. \qquad (7)$$

Suppose a worst accident sequence $n$, which has the greatest impact on latent cancer fatalities risk. This accident sequence $n$ corresponds to a large opening in the containment, and an unscrubbed release occurred after the surrounding population were effectively evacuated. Suppose the worst accident occurs in an open containment; the conditional large latent release probability for accident sequence $n$ ($CLLRP_n$) is 1.0.

Then,

$$LLRF_n = CDF_n * CLLRP_n = CDF_n * 1.0 = CDF_n. \qquad (8)$$

Putting formula (8) into formula (7), the risk of individual latent cancer fatality risk is

$$ILR_n = CPLF_n * CDF_n. \qquad (9)$$

According to the Surry PRA in NUREG-1150, the CPLF of the worst accident sequence is $4 \times 10^{-3}$.

Put $CPLF = 4 \times 10^{-3}$ and the safety goal value $CDF = 1 \times 10^{-4}/(r \cdot y)$ into formula (6). Then, when the worst accident sequence $n$ occurs, the individual latent cancer fatality risk is

$$\begin{aligned} ILR_n &= \left(4 \times 10^{-3}\right) \times \left(10^{-4}\right) = 4 \times 10^{-7}/(r \cdot y) < ILR_{LQHO} \\ &= 2 \times 10^{-6}/(r \cdot y). \end{aligned}$$
$$(10)$$

Therefore, using $CDF < 10^{-4}/(r \cdot y)$ as a subsidiary goal of latent quantitative health objectives (LQHO) for latent cancer fatalities is acceptable.

## 3. Investigation into Chinese Societal Risk

According to the process of determining probabilistic safety goals of USNRC, probabilistic safety goals are based on societal risks. Chinese current probabilistic safety goals refer

to NRC and IAEA, and they are not based on Chinese societal risks. Therefore, we need to investigate the Chinese societal risks firstly and then formulate and verify probabilistic safety goals based on Chinese societal risks.

The data about the societal risk (i.e., mortality rate) can be obtained from the Chinese government and international organizations. Chinese statistics include the National Economic and Societal Development Statistical Bulletin and China's Health Statistical Yearbook [21, 22]. International organizations' statistics include World Health Organization's data [23] and World Bank's data [24].

According to the contents of probabilistic safety goals, we focus on early prompt fatalities and latent cancer fatalities caused by nuclear power plant operation which can be represented by accident mortality and cancer mortality in society, respectively.

In this section, the general overview of Chinese society was investigated firstly, including the analysis about main causes of fatalities in Chinese society, and then make a comparison between the death rate of China and several other countries.

### 3.1. Main Causes of Fatalities in China.
The total population of China, the number of deaths, the number of urban and rural residents, and the GDP from 2012 to 2017 are shown in Table 1.

The mortality rates of different causes were counted, respectively, when counting the main causes of fatalities of Chinese population. Then, the causes of death were sorted according to the value of mortality. The source data are derived from the Chinese government and international organizations, and the statistical results were compared to ensure the authenticity of the data. Statistics from the Chinese government (2012–2017) are shown in Table 2. Statistics from international organizations (2000, 2010, 2015, and 2016) are shown in Table 3.

The causes of fatalities of Chinese population were counted based on the source data from Chinese government and international organizations as shown above. According to the comparison of the above data, the difference between the data obtained through the two channels is small, which proves that the statistics are true and reliable. The main causes of fatalities of Chinese population include malignant neoplasms, cerebrovascular diseases, heart diseases, respiratory diseases, and external causes of damage and poisoning.

### 3.2. Main Causes of Fatalities in Other Countries.
It is necessary to investigate other countries' societal risks and compare the results with Chinese societal risks. On the one hand, the authenticity and reliability of the data can be proved through comparative analysis. On the other hand, investigating more countries' societal risks can help us to provide further suggestions for nuclear safety goals based on societal risks. China, the United States, Japan, the United Kingdom, France, India, Egypt, and Sudan were selected as the research object countries according to the development status and the level of nuclear power in each country. The

causes of death and mortality in these countries in 2016 were counted, and the results are shown in Table 4.

According to the statistical data from international organizations, the causes of death and mortality of China, the United States, Japan, the United Kingdom, France, India, Egypt, and Sudan in 2016 were counted. According to the comparisons of the causes of death and mortality of China and the US, the societal fatalities' risks in China and in the US are similar. For example, the mortality rates caused by cardiovascular diseases, malignant neoplasms, respiratory diseases, and injuries are 317.10, 167.88, 66.47, and 51.15 in China and 259.87, 194.83, 76.65, and 56.98 in the US. For probabilistic safety goals, we focus on the mortality rate of malignant neoplasms and external causes, which are similar between China and the US as well.

Furthermore, the nuclear safety goals of the US were formulated and revised from 1979 to 1986. According to data from international organizations, the mortality rate of malignant neoplasms and external causes in the United States from 1978 to 1985 were counted, and the results are shown in Table 5.

According to the statistical data in the table, the mortality rate of malignant neoplasms and external causes in the United States has not changed much from 1978 to 1985, and they are similar to the current risks of malignant neoplasms and external causes in China.

### 3.3. Probabilistic Safety Goals of Multimodule HTGR.
High-temperature gas-cooled reactors are extremely unlikely to cause serious core damage and large early release due to inherent safety and unique design concepts. CDF and LERF proposed for water-cooled reactor are not suitable for high-temperature gas-cooled reactor. Therefore, the probabilistic safety goal of HTR-PM has been reestablished by China National Nuclear Safety Administration (NASA); that is, "the cumulative frequency of all beyond design basis accident sequences that lead to off-site (including plant boundary) personal effective dose exceeding 50 mSv shall be less than $10^{-6}/(r \cdot y)$," and this risk metric is defined as the "frequency of LARGE release category" in HTR-PM probabilistic safety analysis (PSA) model. In this section, we verified the rationality of Chinese existing probabilistic safety goals for water reactors and then studied the probabilistic safety goals for Chinese high-temperature gas-cooled reactors.

### 3.4. Chinese Existing Probabilistic Safety Goals.
The mortality rate of malignant neoplasms and external causes are important basis when verifying the rationality of Chinese existing CDF and LERF based on the current societal risks in China. According to the above statistics on Chinese societal risks, the statistical results of the mortality rate of malignant neoplasms and external causes are as follows. Statistics based on data from the Chinese government are shown in Table 6, and statistics based on data from international organizations are shown in Table 7.

According to the data from the Chinese government and international organizations shown in Tables 6 and 7, the

TABLE 1: General overview of Chinese Society.

| Year | Total population ('0000) | Dead population ('0000) | Urban population ('0000) | Rural population ('0000) | GDP (100 million) |
|---|---|---|---|---|---|
| 2012 | 135404 | 966 | 71182 | 64222 | 519322 |
| 2013 | 136072 | 972 | 73111 | 62961 | 568845 |
| 2014 | 136782 | 977 | 74916 | 61866 | 636463 |
| 2015 | 137462 | 975 | 77116 | 60346 | 676708 |
| 2016 | 138271 | 977 | 79298 | 58973 | 744127 |
| 2017 | 139008 | 986 | 81347 | 57661 | 827122 |

Source: National Economic and Societal Development Statistical Bulletin [22].

TABLE 2: Demographic mortality statistics in China based on Chinese data.

| Mortality rate (1/100,000) | 2012 | 2013 | 2014 | 2015 | 2016 | 2017 |
|---|---|---|---|---|---|---|
| Malignant neoplasms | 158.3 | 152.6 | 157.4 | 159.8 | 158.3 | 159.1 |
| Cerebrovascular diseases | 127.7 | 137.0 | 137.6 | 139.4 | 140.0 | 139.4 |
| Heart diseases | 125.9 | 138.3 | 139.6 | 140.2 | 144.0 | 146.9 |
| Respiratory diseases | 89.0 | 76.0 | 76.8 | 76.3 | 74.4 | 71.9 |
| External causes of damage and poisoning | 46.2 | 47.4 | 45.7 | 44.6 | 44.7 | 43.2 |
| Other diseases | 26.4 | 8.2 | 6.8 | 6.2 | 6.1 | 6.0 |
| Digestive diseases | 16.0 | 15.5 | 14.5 | 14.2 | 14.2 | 14.5 |
| Endocrine, nutritional, and metabolic diseases | 14.2 | 14.6 | 15.6 | 17.1 | 18.4 | 18.8 |
| Infectious | 6.9 | 7.4 | 7.2 | 7.2 | 7.0 | 6.7 |
| Neurological conditions | 6.6 | 6.8 | 6.8 | 6.7 | 7.5 | 7.7 |
| Genitourinary diseases | 6.5 | 6.7 | 6.9 | 6.8 | 6.9 | 7.1 |
| Mental disorders | 2.5 | 2.8 | 2.7 | 2.8 | 2.8 | 2.7 |
| Acatalepsia | 2.3 | 2.5 | 2.5 | 2.3 | 2.2 | 2.1 |
| Neonatal conditions | 2.3 | 2.2 | 2.3 | 1.9 | 2.0 | 1.7 |
| Congenital anomalies and chromosomal abnormalities | 2.0 | 2.1 | 2.0 | 1.8 | 1.6 | 1.6 |
| Musculoskeletal diseases | 1.4 | 1.7 | 1.7 | 1.7 | 2.0 | 2.1 |
| Blood, hematopoietic organ, and immune disorders | 1.2 | 1.2 | 1.2 | 1.2 | 1.3 | 1.3 |
| Complications of pregnancy, childbirth, and puerperium | 0.1 | 0.1 | 0.1 | 0.1 | 0.1 | 0.1 |
| Parasitic diseases | 0.1 | 0.1 | 0.0 | 0.1 | 0.1 | 0.1 |

Source: China's Health Statistical Yearbook [21]. *Note.* External causes of injury and poisoning include traffic accidents, poisoning, falls, fires, natural disasters, mechanical asphyxiation, suicide, homicide, and mechanical injuries.

individual latent cancer fatality risk (ILCFR) is about $1.6 \times 10^{-3}/y$, and the individual early prompt fatality risk (IEPFR) is about $5 \times 10^{-4}/y$.

According to the Chinese societal risks, the reasonability of existing probabilistic safety goals in China is shown in Figure 3. Based on the Chinese societal risks and quantitative safety goals ("two 0.1% rule"), the individual latent cancer fatality risk caused by nuclear power plant operation ($\text{ILCFR}_{\text{NPP}}$) should be less than $1.6 \times 10^{-6}/y$, and the individual early prompt fatality risk caused by nuclear power plant accidents ($\text{IEPFR}_{\text{NPP}}$) should be less than $5 \times 10^{-7}/y$. Based on the subsidiary safety goals and the assessment of nuclear power plant, the $\text{ILCFR}_{\text{NPP}}$ is less than $4 \times 10^{-8}/y$, and the $\text{IEPFR}_{\text{NPP}}$ is less than $3 \times 10^{-8}/y$. As shown above, Chinese current probabilistic safety goals can meet the needs of Chinese societal risks control.

*3.5. Probabilistic Safety Goals of Multimodule HTGR.* The design characteristics and defense-in-depth measures of multimodule HTGR nuclear power plants are different from those of water reactor nuclear power plants. Due to the safety design concept, inherent safety, and passive safety measures, there is extremely low large release frequency and longer time before radioactive material is released into the environment. So, there is longer time for postaccident mitigation and emergency response, allowing more measures to actually eliminate core damage and large early release. Therefore, it uses the "frequency of LARGE release category" defined in HTGR PSA as the risk index rather than the CDF or LERF. According to the risk metric of HTR-PM, it should be less than $10^{-6}/(r \cdot y)$. However, it should be noted that this safety goal is dedicated to HTR-PM project, and it is focused on single reactor rather than unit (two reactors and one turbine). Therefore, this paper tries to study whether this risk metric can be extended to be applied to the multimodule HTGR; that is, can we use the "frequency of LARGE release category less than $10^{-6}/(\text{unit} \cdot y)$ or $10^{-6}/(\text{site} \cdot y)$ as the risk metric of multimodule HTGR directly.

In the following, we will use the risk metric of HTR-PM to demonstrate the margin of probabilistic safety goal.

The "LARGE" release category of HTR-PM is similar to the LERF of water reactors, and it focuses on early prompt fatalities risks and EQHO. Individual early risk (IER) is

TABLE 3: Demographic mortality statistics in China based on the WHO data.

| Mortality rate (1/100,000) | 2000 | 2010 | 2015 | 2016 |
|---|---|---|---|---|
| Cardiovascular diseases | 212.8 | 269.6 | 309.5 | 317.1 |
| Malignant neoplasms | 144.4 | 159.9 | 166.3 | 167.9 |
| Respiratory diseases | 97.5 | 71.2 | 65.9 | 66.5 |
| External causes of damage and poisoning | 60.7 | 54.0 | 50.9 | 51.2 |
| Neurological condition | 20.6 | 32.3 | 42.0 | 44.9 |
| Digestive diseases | 18.3 | 17.4 | 19.2 | 19.7 |
| Genitourinary diseases | 9.8 | 12.3 | 14.9 | 15.2 |
| Respiratory infectious | 19.2 | 12.6 | 12.4 | 12.6 |
| Diabetes mellitus | 7.7 | 9.7 | 11.6 | 11.9 |
| Infectious and parasitic diseases | 18.6 | 12.0 | 9.6 | 9.2 |
| Neonatal conditions | 18.0 | 8.0 | 5.4 | 4.9 |
| Mental and substance use disorders | 2.1 | 2.6 | 3.1 | 3.2 |
| Congenital anomalies | 6.7 | 4.6 | 3.3 | 3.1 |
| Other neoplasms | 1.5 | 2.4 | 2.9 | 2.9 |
| Endocrine, blood, and immune disorders | 1.5 | 1.4 | 1.7 | 1.7 |
| Musculoskeletal diseases | 1.1 | 1.3 | 1.5 | 1.5 |
| Nutritional deficiencies | 1.4 | 0.9 | 1.1 | 1.1 |
| Skin diseases | 0.3 | 0.4 | 0.5 | 0.5 |
| Sudden infant death syndrome | 0.1 | 0.1 | 0.1 | 0.1 |

Source: World Health Organization statistics [23]. *Note.* External causes of injury and poisoning include road injury, poisonings, falls, fire, heat and hot substances, drowning, exposure to mechanical forces, natural disasters, other unintentional injuries, self-harm, interpersonal violence, collective violence, and legal intervention.

$$IER = \sum_1^H \frac{(EF_h * LARGE_h)}{TP(1)}, \quad (11)$$

where $EF_h$ is the number of early prompt fatalities within 1 mile caused by accident sequence $h$. $LARGE_h$ is the frequency of fatal LARGE categories caused by accident sequence $h$. $TP(1)$ is the total population within 1 mile of the nuclear power plant.

Then, in the population $TP(1)$, the number of early prompt fatalities caused by accident sequence $h$ is

$$EF_h = CPEF_h * TP(1), \quad (12)$$

where $CPEF_h$ is the conditional probability of early prompt fatalities caused by accident sequence $h$, meaning the conditional probability of one person's early fatality caused by a radioactive release nuclear accident.

According to formulae (9) and (10), the individual early prompt fatality risk is

$$IER = \sum_1^H CPEF_h * LARGE_h. \quad (13)$$

According to the data survey for Chinese societal risks, the individual risk of prompt fatality caused by all other accidents is $5 \times 10^{-4}/y$ in China. According to the 0.1% in the early quantitative health objective (EQHO), the individual early risk ($IER_{EQHO}$) caused by nuclear power plant accidents needs to be less than $5 \times 10^{-7}/(r \cdot y)$. Suppose a worst accident sequence $h$, which has the greatest impact on early prompt fatalities risk. An unscrubbed release occurred before the surrounding population were effectively evacuated.

Suppose

$$IER_h = CPEF_h * LARGE_h = IER_{EQHO} = \frac{5 \times 10^{-7}}{(r \cdot y)}. \quad (14)$$

According to the probabilistic safety goals for multi-HTGR, $LARGE_h = 1 \times 10^{-6}/(r \cdot y)$.

Thus, $CPEF_h = 0.5$.

That is, the conditional probability of early prompt fatalities caused by the worst accident sequence $h$ is 0.5; it just meets the EQHO for individual early prompt fatalities risks.

In the International Commission on Radiological Protection (ICPR) Publication 60, according to the dose threshold of the deterministic effects, the 60-day median lethal dose ($LD_{50}[60]$) is 3~5 Gy/time. The probability of stochastic effects increases with increasing dose. Stochastic effects include cancer and hereditary diseases. For cancer, the probability coefficients of fatal cancer are $5 \times 10^{-2}$/Sv for the public and $4 \times 10^{-2}$/Sv for occupational workers engaged in radiation. For hereditary diseases, the probability coefficients of hereditary diseases are $1 \times 10^{-2}$/Sv for the public and $0.6 \times 10^{-2}$/Sv for workers. ICPR 103 followed the conclusion of the ICRP 60; the combined detriment due to fatal cancer and hereditary diseases remains unchanged at around $5 \times 10^{-2}$/Sv. For HTR-PM, there is extremely low large release frequency, and the personal effective dose control threshold is 50 mSv. According to the results of above analysis, when $LARGE_h = 1 \times 10^{-6}/(r \cdot y)$ and $CPEF_h = 0.5$, the risk metric of HTR-PM can meet the requirements of Chinese societal risks. In fact, the personal effective dose control threshold is 50 mSv, and actual $CPEF_h$ is extremely low as well, so the risk metric of HTR-PM has large margin compared with Chinese societal risk. Therefore, it give us the confidence to expand the risk metric of HTR-PM (i.e., $1 \times 10^{-6}$/reactor $\cdot y$) to multimodule HTGR (i.e., $1 \times 10^{-6}/(unit \cdot y)$ or $1 \times 10^{-6}/(site \cdot \leq y)$), and then the risk metric of multimodule HTGR can meet the requirements of Chinese societal risks.

## 4. Discussions

Existing nuclear safety goals is mainly for a single reactor. But in fact, most of the plant sites are multireactor sites. Multireactor site means a nuclear power plant site with two or more reactors on one site. From the Fukushima nuclear accident, we realized the possibility and severity of nuclear accidents occurring at multiple reactors at the same time. Nuclear safety goals are set to protect the lives, health, and environment of populations. For the populations, not only the impact of a single reactor on the human body must be considered, but also the impact of the entire plant site on the human body.

For example, expand the risk metric of HTR-PM from a single reactor to a plant site and explore the adaptability of probabilistic safety goals. The current probabilistic safety goals of HTR-PM are that the cumulative frequency of all accident sequences that cause the personal effective dose

TABLE 4: Demographic mortality statistics in different countries.

| Mortality rate (1/100,000) | China | The US | Japan | The UK | France | India | Egypt | Sudan |
|---|---|---|---|---|---|---|---|---|
| All causes | 734.9 | 869.8 | 1026.0 | 912.4 | 861.6 | 722.6 | 635.9 | 712.3 |
| Cardiovascular diseases | 317.1 | 259.9 | 280.8 | 228.7 | 221.6 | 195.6 | 257.0 | 202.9 |
| Malignant neoplasms | 167.9 | 194.8 | 312.9 | 255.7 | 267.9 | 61.6 | 81.2 | 44.6 |
| Respiratory diseases | 66.5 | 76.7 | 90.1 | 76.0 | 48.0 | 76.8 | 27.1 | 22.1 |
| Injuries | 51.2 | 57.0 | 49.7 | 31.8 | 54.8 | 81.8 | 36.7 | 89.6 |
| Neurological conditions | 44.9 | 102.1 | 41.8 | 149.9 | 99.5 | 15.8 | 22.1 | 16.3 |
| Digestive diseases | 19.7 | 36.7 | 45.3 | 43.5 | 38.4 | 38.5 | 83.4 | 20.9 |
| Genitourinary diseases | 15.2 | 26.7 | 34.7 | 16.1 | 16.4 | 23.0 | 19.7 | 19.8 |
| Respiratory infectious diseases | 12.6 | 20.6 | 110.7 | 57.1 | 27.7 | 46.6 | 23.1 | 48.2 |
| Diabetes mellitus | 11.9 | 26.2 | 11.3 | 10.0 | 19.1 | 23.3 | 18.7 | 14.6 |
| Infectious and parasitic diseases | 9.2 | 17.5 | 17.0 | 10.1 | 15.4 | 90.6 | 12.4 | 101.1 |
| Neonatal conditions | 4.6 | 3.6 | 0.5 | 2.5 | 2.4 | 41.5 | 26.8 | 89.4 |
| Mental and substance use disorders | 3.2 | 14.9 | 1.8 | 5.7 | 9.2 | 2.4 | 0.6 | 1.6 |
| Congenital anomalies | 3.1 | 4.0 | 2.2 | 3.5 | 3.0 | 7.9 | 15.1 | 18.0 |
| Other neoplasms | 2.9 | 5.1 | 9.9 | 6.0 | 11.8 | 1.1 | 3.8 | 3.2 |
| Endocrine, blood, and immune disorders | 1.7 | 14.1 | 8.2 | 4.8 | 10.8 | 1.6 | 5.2 | 5.4 |
| Musculoskeletal diseases | 1.5 | 4.5 | 5.2 | 7.0 | 6.7 | 3.7 | 0.2 | 0.7 |
| Nutritional deficiencies | 1.1 | 3.0 | 2.5 | 0.6 | 6.5 | 6.3 | 1.4 | 3.4 |
| Skin diseases | 0.5 | 1.6 | 1.5 | 3.1 | 2.1 | 1.0 | 0.1 | 0.8 |
| Maternal conditions | 0.3 | 0.2 | 0.0 | 0.1 | 0.1 | 3.1 | 0.9 | 9.0 |
| Sudden infant death syndrome | 0.1 | 0.5 | 0.1 | 0.2 | 0.2 | 0.4 | 0.6 | 0.9 |
| Sense organ diseases | . | 0.0 | 0.0 | 0.1 | 0.1 | . | . | . |
| Oral conditions | . | 0.1 | 0.1 | 0.1 | 0.2 | 0.0 | . | . |

Source: World Health Organization statistics [23].

TABLE 5: The mortality rate of malignant neoplasms and external causes in the US.

| Mortality rate (1/100,000) | 1978 | 1979 | 1980 | 1981 | 1982 | 1983 | 1984 | 1985 |
|---|---|---|---|---|---|---|---|---|
| Malignant neoplasms | 161.7 | 175.4 | 179.5 | 180.2 | 183.6 | 185.9 | 188.7 | 190.5 |
| External causes | 70.7 | 70.6 | 70.7 | 67.8 | 63.8 | 61.6 | 61.5 | 61.2 |

Source: World Health Organization statistics [23].

TABLE 6: The mortality rate of malignant neoplasms and external causes in China (1).

| Mortality rate (1/100,000) | 2012 | 2013 | 2014 | 2015 | 2016 | 2017 | Average |
|---|---|---|---|---|---|---|---|
| Malignant neoplasms | 158.3 | 152.6 | 157.4 | 159.8 | 158.3 | 159.1 | 157.6 |
| External causes | 46.2 | 47.4 | 45.7 | 44.6 | 44.7 | 43.2 | 45.3 |

TABLE 7: The mortality rate of malignant neoplasms and external causes in China (2).

| Mortality rate (1/100,000) | 2016 | 2015 | 2010 | 2000 | Average |
|---|---|---|---|---|---|
| Malignant neoplasms | 167.9 | 166.3 | 159.9 | 144.4 | 159.6 |
| External causes | 51.2 | 50.9 | 54.0 | 60.7 | 54.2 |

outside the plant (including the site boundary) to exceed 50 mSv is less than $10^{-6}/(r \cdot y)$. Expanding from a single reactor to a plant site means LARGE = $10^{-6}/(\text{reactor} \cdot \text{year})$ changed to LARGE = $10^{-6}/(\text{site} \cdot \text{year})$ (site·year, $s \cdot y$).

Through the derivation in Section 4, LARGE = $10^{-6}/(s \cdot y)$; then, $\text{CPEF}_h = 0.5$. That is, the conditional probability of early prompt fatalities caused by the worst accident sequence $h$ in the entire plant site is 0.5; it

just meets the EQHO for individual early prompt fatalities' risks.

Suppose there are two reactors in a plant site, and suppose that the two reactors suffer the worst accident sequence at the same time. In order to ensure the probabilistic safety goals of the multimodule HTGR site and ensure a sufficient safety margin, it is necessary to ensure the cumulative frequency of beyond design basis accidents with a
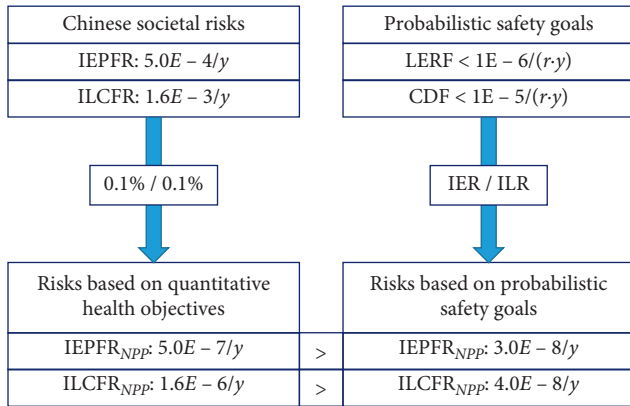
| Chinese societal risks |
| --- |
| IEPFR: $5.0E - 4/y$ |
| ILCFR: $1.6E - 3/y$ |

| Probabilistic safety goals |
| --- |
| LERF < 1E − 6/$(r \cdot y)$ |
| CDF < 1E − 5/$(r \cdot y)$ |

| 0.1% / 0.1% |
| --- |

| IER / ILR |
| --- |

| Risks based on quantitative health objectives | | |
| --- | --- | --- |
| IEPFR$_{NPP}$: $5.0E - 7/y$ | > | IEPFR$_{NPP}$: $3.0E - 8/y$ |
| ILCFR$_{NPP}$: $1.6E - 6/y$ | > | ILCFR$_{NPP}$: $4.0E - 8/y$ |

| Risks based on probabilistic safety goals |
| --- |

Figure 3: The rationality of existing probabilistic safety goals in China.

personal effective dose exceeding 50/2 = 25 mSv for each reactor is less than $10^{-6}/2 = 5 \times 10^{-7}/(r \cdot y)$.

In fact, the individual effective dose and cumulative frequency caused by the entire plant site are not necessarily the simple addition of the individual effective dose and cumulative frequency caused by each single reactor. However, in order to ensure the probabilistic safety goals, the value of the probabilistic safety goals of each single reactor is smaller than the entire plant site. We need to consider the following points:

(a) The safety and reliability of a single reactor is constant. The number of reactors on the site needs to be controlled and cannot be increased indefinitely.

(b) The design of the reactors can still be based on the single reactor for the convenience of design. But for the entire plant site, we can consider different types of reactors with different risk levels at the same site.

## 5. Conclusions

According to the statistics on societal risks in China, the individual latent cancer fatality risk (ILCFR) is $1.6 \times 10^{-3}/y$, and the individual early prompt fatality risk (IEPFR) is $5 \times 10^{-4}/y$. The mortality rates are similar in China and the United States, and the changes in recent years are small. The Chinese current probabilistic safety goals can meet the requirement of little contribution to social risks.

The probabilistic safety goals of HTR-PM recommended by China's National Nuclear Safety Administration (NNSA) are as follows: the cumulative frequency of all beyond-design-basis accident sequences that lead to off-site (including plant boundary) personal effective dose exceeding 50 mSv shall be less than $10^{-6}/(r \cdot y)$. According to the inference, the probabilistic safety goals are rational. And the risk metric of HTR-PM has large margin according to the societal risk of China; maybe, it can be extended to be applied to the multimodule HTGR as "frequency of LARGE release category less than $10^{-6}/(\text{unit} \cdot y)$ or $10^{-6}/(\text{site} \cdot y)$."

In the end, we think it is better that the probabilistic safety goals based on entire plant site rather than a single reactor. We need to control the number of reactors on one site, and we can consider different types of reactors with different risk levels at the same site. And the above analysis process is applicable to other types of reactors.

## Data Availability

The data used in this paper are obtained from China National Bureau of Statistics (http://www.stats.gov.cn/) and World Health Organization (https://www.who.int/data/collections).

## Conflicts of Interest

The authors declare that they have no conflicts of interest regarding the publication of this paper.

## Acknowledgments

## References

[1] C. Meyer, "China and nuclear energy: solving an energy crisis–part 4," *Energize*, vol. 7, no. 42, pp. 18-19, 2011.

[2] J. Wood, "Nuclear safety and three major accidents," *Nuclear Power. IET Digital Library*, vol. 18, no. 6, 2007.

[3] OECD/NEA, *Probabilistic Risk Criteria and Safety Goals, NEA/CSNI/R*, Organization for Economic Cooperation and Development/Nuclear Energy Agency (OECD/NEA), Paris, France, 2009.

[4] Z. Zhang, Z. Wu, and Y. Sun, "Design aspects of the Chinese modular high-temperature gas-cooled reactor HTR-PM," *Nuclear Engineering & Design*, vol. 236, no. 5-6, pp. 485–490, 2006.

[5] IAEA, "Policy for setting and assessing regulatory safety goals," 1995.

[6] EPRI, "Advanced light water reactor utility requirements document," *ALWR Policy and Summary of Top-Tier Requirements*, vol. 1, 1990.

[7] K. R. KEMA, "European utility requirements for LWR nuclear power plants," *Main Policies and Top Tier Requirements, Revision B*, vol. 1, 1995.

[8] GPR-RSK, "IPSN-GRS proposals for the development of technical guideline for future pWRs," 1997.

[9] IAEA, *Safety Series 75-INSAG-3, Basic Safety Principles for Nuclear Power Plants*, IAEA, 1988, https://www.google.com/search?rlz=1C1GCEJ_enIN954IN954&q=Vienna&stick=H4sIAAAAAAAAAOPgE-LQz9U3MC43slACs9IyCiy1tLKTrfTzi9IT8zKrEksy8_NQOFYZqYkphaWJRSWpRcWLWNnCMlPz8hJ3sDICANR77yBOAAAA&sa=X&ved=2ahUKEwipg5u38-zwAhULIbcAHc0pBCcQmxMoATA4egQINRAD.

[10] IAEA, *Safety Series 75-INSAG-12, Basic Safety Principles for Nuclear Power Plants*, IAEA, 1999, https://www.google.com/search?rlz=1C1GCEJ_enIN954IN954&q=Vienna&stick=H4sIAAAAAAAAAOPgE-LQz9U3MC43slACs9IyCiy1tLKTrfTzi9IT8zKrEksy8_NQOFYZqYkphaWJRSWpRcWLWNnCMlPz8hJ3sDICANR77yBOAAAA&sa=X&ved=2ahUKEwipg5u38-zwAhULIbcAHc0pBCcQmxMoATA4egQINRAD.

[11] IAEA, *Safety Standards Series No.NS-R-1, Safety of Nuclear Power Plants: Design*, IAEA, 2000, https://www.google.com/search?rlz=1C1GCEJ_enIN954IN954&q=Vienna&stick=H4s IAAAAAAAAAOPgE-LQz9U3MC43slACs9IyCiy1tLKTrfTz i9IT8zKrEksy8_NQOFYZqYkphaWJRSWpRcWLWNnCMl Pz8hJ3sDICANR77yBOAAAA&sa=X&ved=2ahUKEwipg5u 38-zwAhULIbcAHc0pBCcQmxMoATA4egQINRAD.

[12] IAEA, *Safety Standards Series No.NS-G-1.2, Safety Assessment and Verification for Nuclear Power Plants*, IAEA, 2001, https://www.google.com/search?rlz=1C1GCEJ_enIN954IN954&q=Vi enna&stick=H4sIAAAAAAAAAOPgE-LQz9U3MC43slACs9I yCiy1tLKTrfTzi9IT8zKrEksy8_NQOFYZqYkphaWJRSWpRc WLWNnCMlPz8hJ3sDICANR77yBOAAAA&sa=X&ved=2ah UKEwipg5u38-zwAhULIbcAHc0pBCcQmxMoATA4egQINR AD.

[13] USNRC, *51 Federal Register 7023, Safety Goals for the Operation of Nuclear Power Plants; Policy Statement*, USNRC, Rockville, MD, USA, 1982.

[14] USNRC, *51 Federal Register 10772, Safety Goals for the Operation of Nuclear Power Plants; Policy Statement*, USNRC, Rockville, MD, USA, 1983.

[15] USNRC, *51 Federal Register 30028, Safety Goals for the Operation of Nuclear Power Plants; Policy Statement; Republication. Federal Register*, USNRC, Rockville, MD, USA, 1986.

[16] China National Nuclear Safety Administration, *Provisions on Design Safety of Nuclear Power Plant, HAF102*, National Nuclear Safety Administration, 1991, Beijing, China, 2016.

[17] China National Nuclear Safety Administration, *Safety Evaluation and Validation of Nuclear Power Plant*, National Nuclear Safety Administration, Beijing, China, 2006.

[18] China National Nuclear Safety Administration, *Twelfth Five-Year Plan and Vision 2020 for Nuclear Safety and Radioactive Pollution Prevention*, Beijing, China Environmental News, Beijing, China, 2012.

[19] China National Nuclear Safety Administration, *Thirteenth Five-Year Plan and Vision 2025 for Nuclear Safety and Radioactive Pollution Prevention*, Beijing, China Environmental News, Beijing, China, 2017.

[20] USNRC. NUREG-1860, *Feasibility Study for a Risk-Informed and Performance-Based Regulatory Structure for Future Plant Licensing*, Washing DC: United States Nuclear Regulatory Commission, Washington, DC, USA, 2007.

[21] China National Health Commission, *China Health Statistical Yearbook*, China Union Medical College Press, Beijing, China, 2017.

[22] China National Bureau of Statistics, *National Economic and Societal Development Statistical Bulletin*, National Bureau of Statistics, Beijing, China, 2017.

[23] World Health Organization, *Global Health Estimates Summary Tables*, WHO, Geneva, Switzerland, 2021, http://www.who.int/healthinfo/global_burden_disease/en/.

[24] The World Bank, *Free and Open Access to Global Development Data*, The World Bank, Washington, DC, USA, 2021, https://data.worldbank.org/.

*Research Article*

# Development of Fuel Product Barrier Monitoring System Based on State Functions in State-Oriented Emergency Operating Procedure

**Wang Zhenying** ⓘ**, Shi Yanming, Xu Huibo, Zhang Lijun, Zhou Shiqing, Gao Chunyan, and Huang Yu**

*State Key Laboratory of Nuclear Power Safety Monitoring Technology and Equipment, Shenzhen 518100, China*

Correspondence should be addressed to Wang Zhenying; wangzhenying@cgnpc.com.cn

For pressurized water reactor nuclear power plants, in order to prevent the release of radioactive substances into environment, fission product barriers (FPBs) are constructed based on the concept of defense-in-depth, including fuel clad, reactor coolant system (RCS), and containment; the status of these FPBs is then acting as an important dimension to decision-making of emergency action levels (EALs). For CPR1000 nuclear power plants, state functions defined in state-oriented emergency operating procedure (SOP) are used to characterize postaccident physical conditions; their degradation substantially represents the challenges on fundamental safety functions and then on the integrity of FPBs in like manner, so degradation of these state functions is referred to as determining initial conditions of each FPB, by which the link between SOP and EALs is established. Then, an intelligent FPB monitoring system (FPBMS) aiming to automatically monitor states of FPBs is developed, verified, and validated. The pioneering work, by building bridges between state functions and initial conditions of FPBs and then computerizing them innovatively, proves that dynamical monitoring of states of FPBs during accident evolvement and real-time indication of loss or potential loss of FPBs can be achieved, which is most helpful in decision-making of EALs.

## 1. Introduction

Nuclear accidents are different from other accidents in that they may lead to unacceptable release of radioactive substances into environment. In order to quickly and effectively control and mitigate consequences of nuclear accidents, nuclear power plant should establish a thorough emergency plan for nuclear accidents and maintain adequate emergency preparedness (IAEA [1, 2]), among which determination of emergency classification levels (ECLs) and emergency action levels (EALs) is very important issue. As for nuclear power plants in China, EALs are progressively divided into four action levels: emergency standby, facility emergency, on-site emergency, and off-site emergency (NNSA [3, 4]).

In order to prevent the release of radioactive substances into the environment, nuclear power plants have set up multiple fission product barriers (FPBs); these FPBs are

fundamentally constructed based on the concept of defense-in-depth; as long as any of the physical barriers remains intact, it can effectively prevent the large-scale release of radioactive fission products into environment. For pressurized water reactors, three primary FPBs are generally constructed, including fuel clad, reactor coolant system (RCS), and containment. The status of these FPBs has also been acting as an important dimension while developing site-specific EALs, in which it is usually classified as recognition category F, that is, evaluating threats to each FPB after accidents and identifying typical symptoms indicating that its integrity is potentially or substantially challenged, and then initial conditions relative to the FPB are determined based on these symptoms (NEIs [5, 6]).

How to evaluate threats to each FPB and screen out the representative symptoms indicates that its states have become the key problem. As for the methodologies for

development of EALs, Shi [7] suggested a general methodology to determine EALs based on postaccident plant conditions, Liu et al. [8] investigated the popular technical systems for development of EAL, and recognition category "A" was specially studied (Liu [9]), He et al. [10] advanced a system of generic intervention levels and generic action levels for HPR1000, and Zang et al. [11] suggested a risk-informed optimization method of EALs for advanced passive light reactor. Meanwhile, emergency operating procedures (EOPs), aiming to monitor and control the reactor after accidents, have been suggested to be coupled with EALs. Faletti et al. [12] attempted to integrate EALs with Combustion Engineering EOPs, Yang [13] jointed the critical safety functions status tree (CSFST) in EOP with EALs for Qinshan Nuclear power plant, Yu [14] tried to connect the event-oriented EOPs with EALs for Fuqing nuclear power plant, and Zhang and Xu [15] discussed the initial conditions of EALs relative to anticipated transients without scream (ATWS). NEI [5, 6] suggested that some red paths of CSFST, indicating severe degradation of critical safety functions, can be directly taken as the symptoms of loss or potential loss of a FPB, and thereupon can be referred to as the initial conditions of recognition category F. As for computerization of EALs, Chen et al. [16] realized a primary EALs semiautomatic judgment and warning system which still mostly depended on personal judgments. It also should be noted that CSFST is characteristic of symptom-oriented EOPs developed by Westinghouse; when these initial conditions are applied to CPR1000 nuclear power plants, adopting state-oriented EOP (SOP), a series of problems are emerging, such as the inappropriate parameters and thresholds, hard to execute, and so on.

This study aims to establish the link between SOP and EALs, after capturing the functional requirements; for each FPB, we determine initial conditions representing its loss or potential loss based on the degradation states of state functions as well as several other important parameters; then an intelligent FPB monitoring system, aiming to dynamically monitor and indicate states of FPBs during accident evolvement, is developed, verified, and validated.

## 2. Functional Requirement

Appropriate parameters and reasonable thresholds are the basic basis of judging the integrity of FPBs after accidents. These parameters and thresholds should represent the typical symptoms of credible threats which may lead to loss of integrity of an FPB, excluding all other conditions where the integrity of the FPB is not challenged.

SOP in CPR1000 nuclear power plants is developed based on six state functions of nuclear steam supply system (NSSS); these six state functions can characterize postaccident states of reactor representatively, as shown in Table 1. Rather than finding out the reason for accident, SOP aims to control the six state functions, to prevent them from degradation, or to restore them after their degradation. As long as these state functions are well managed, the safety of the reactor will be ensured; once degradation of state functions is detected, operators will be oriented to corresponding accident strategies and operating sequences to

restore them orderly (J. Mišák [17]). SOP has a loop structure to keep periodically surveillance on these state functions, so as to detect possible concurrent accidents and change accident strategy in time. Although the initial conditions of FPBs focus on the threats on integrity of FPBs, they are consistent with the physical conditions characterized by degradation of state functions in SOP from the impact on fundamental safety functions (reactivity, core cooling, and containment) point of view; for example, degradation of secondary water inventory in SOP indicates that the residual heat cannot be effectively removed by steam generators (SG) and core cooling cannot be ensured anymore, which also certainly presents a potential challenge to the integrity of RCS. Therefore, the parameters and thresholds relative to state functions that have been well defined in SOP can be taken as the typical symptoms of loss or potential loss of FPBs as long as they essentially represent the same physical significance; for this reason, the degradation of state functions can be depended on to determine the initial conditions of FPBs, which will build a bridge between SOP and EALs and is conducive to timely and reasonable decision-making of EALs after accidents.

Additionally, considering that the state functions are periodically monitored only at the end of each operating sequence with a period of about 20 min, during which time SOP will complete a loop, the interval may delay the annunciation of EALs for some time, so we consider building an intelligent FPB monitoring system (FPBMS); taking the advantages of digital control system (DCS), the system should be able to automatically perform surveillance on integrity of FPBs and indicate the status of FBPs under accident conditions in a timely manner.

## 3. FPB Initial Conditions

For each FPB, as suggested in NEI 99–01 [6], two states are defined: loss and potential loss. Then, for each state of each FPB, the initial conditions are determined based on degradation of state functions as well as several other important parameters; these initial conditions are constructed into judgment logics which will be configured in FPBMS.

*3.1. Fuel Clad Barrier.* The fuel clad barrier consists of all the clad of fuels in reactor core. For CPR1000 nuclear power plants, the logical criteria related to the state of fuel clad barrier based on state functions are shown in Figure 1.

We regard the beginning of uncovering of fuel assemblies in core as a criterion for potential loss of fuel clad barrier. CPR1000 nuclear power plants have installed core cooling and monitoring system (CCMS) which supplies both $\Delta T_{sat}$ and RPVL measurements to monitor state functions WR (P, T) and $IE_P$, respectively (He et al. [18]); these two state functions are dedicated to identifying the core cooling state in postaccident conditions and thus can be used to detect whether fuel assemblies are beginning to uncover or not:

(1) Degradation of $IE_P$: in SOP, it is characterized by RPVL lower than the top of the core; the scenario could only appear following continual draining of

TABLE 1: State functions in SOP.

| State functions | Safety functions | Parameters |
|---|---|---|
| Subcriticality (S/K) | Reactivity | Intermediate range detector (IRD) |
| Residual heat removal [WR (P, T)] | Core cooling | RCS pressure (P RCS), subcooling margin ($\Delta$Tsat), and temperature at core outlet (T RIC) |
| Primary water inventory (IE$_P$) | | Reactor pressure vessel water level (RPVL) |
| Secondary water inventory (IE$_S$) | | SG water level wide range (L SG WR) |
| Secondary integrity (INT$_S$) | Containment | Steam line pressure and SG activity channels |
| Containment integrity (INT$_E$) | | Containment pressure (Pcont) and containment dose rate (DRcont) |
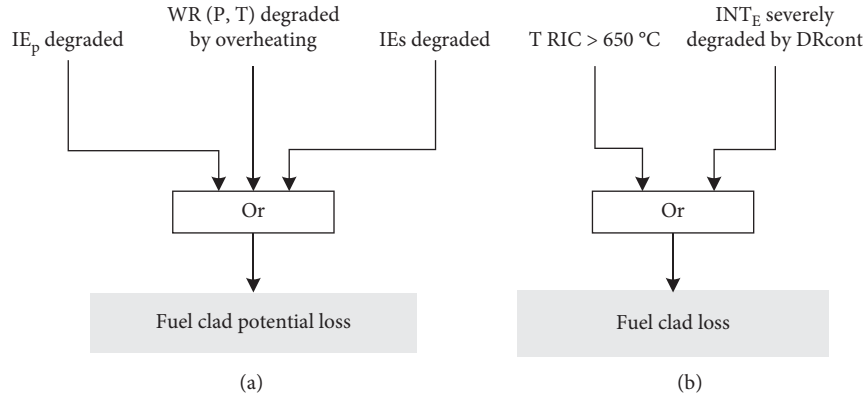
FIGURE 1: Fuel clad barrier initial conditions.

primary coolant, degradation of IE$_P$ means that the water level in reactor pressure vessel has begun to be lower than the physical level of the core, and fuel assemblies are beginning to uncover.

(2) Degradation of WR (P, T) due to overheating: in SOP, it is characterized by $\Delta$Tsat < -$\varepsilon$, where "$\varepsilon$" is the uncertainty surrounding the measurement of $\Delta$Tsat (Wang et al. [19]). Negative $\Delta$Tsat means that the subcooling margin of coolant at the core outlet has been actually lost, superheated steam is beginning to appear at the core outlet, and the phenomena can only occur when the fuel assemblies are beginning to uncover.

(3) In terms of the secondary side, degradation of IE$_S$, which is characterized by L SG WR < −3 m in SOP, means that SGs have lost their capacity of heat removal due to the nearly dry-up of secondary side water inventory, as the residual heat cannot be effectively removed, overheating in the core and failure of fuel assemblies is anticipated, and this also indicates a potential loss of fuel clad barrier.

We regard the beginning of the failure of fuel clad as a criterion for loss of fuel clad barrier. T RIC > 650°C, as the temperature criterion for entering into severe accident management guideline (SAMG), indicates that the upper half of the core has already uncovered and failure of fuel clad is anticipated in several minutes; then it is taken as an initial condition for loss of fuel clad barrier. As for state function INT$_E$, if its severe degradation is caused by high dose rate in

containment as shown in Figure 2, it means that a certain proportion (about 2%~5%) of the fuel clad has been failed, radioactive substances (such as noble gases) filled in the pellet-clad gap have released into primary coolant and then into the containment, and this condition also indicates loss of fuel clad barrier.

3.2. RCS Barrier. The RCS barrier consists of RCS primary side, pressurizer safety valves, and all connecting pipelines and valves up to the isolation valves to RCS. For CPR1000 nuclear power plants, the logical criteria related to state of RCS barrier based on state functions are shown in Figure 3.

For potential loss of RCS barrier, the following initial conditions are identified:

(1) Degradation of WR (P, T) due to overcooling: It is characterized by $\Delta T$sat >140°C and represents a severe overcooling condition which may occur after steam line break with safety injection in service. In this condition, high risk of pressurized thermal shock on reactor pressure vessel may lead to its brittle fracture and threaten the integrity of the RCS barrier.

(2) P RCS > 4.5 MPa (RHRS connected): $\Delta T$sat > 140°C can only cover the operation modes that residual heat removal system (RHRS) is not connected; for the lower operation modes with RHRS connected, the setpoint pressure of safety valves on RHRS
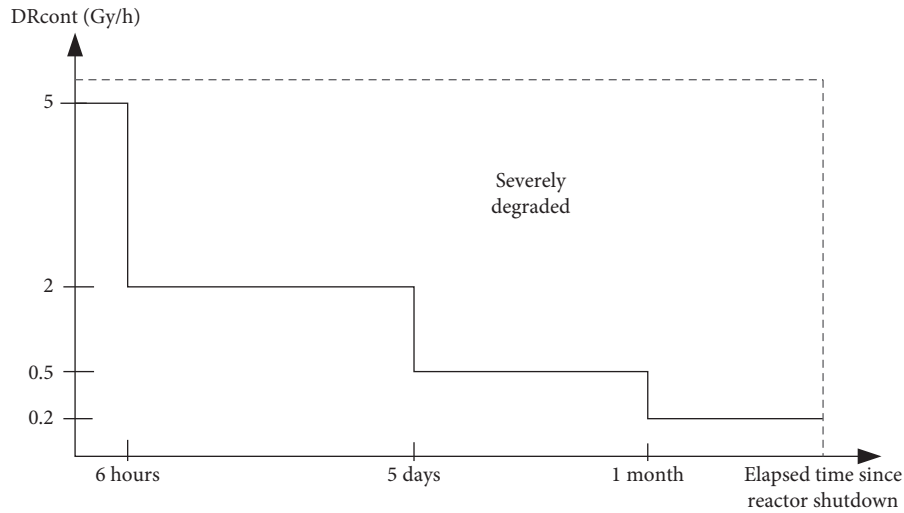
FIGURE 2: Threshold of high DRcont in SOP.



(a)

(b)
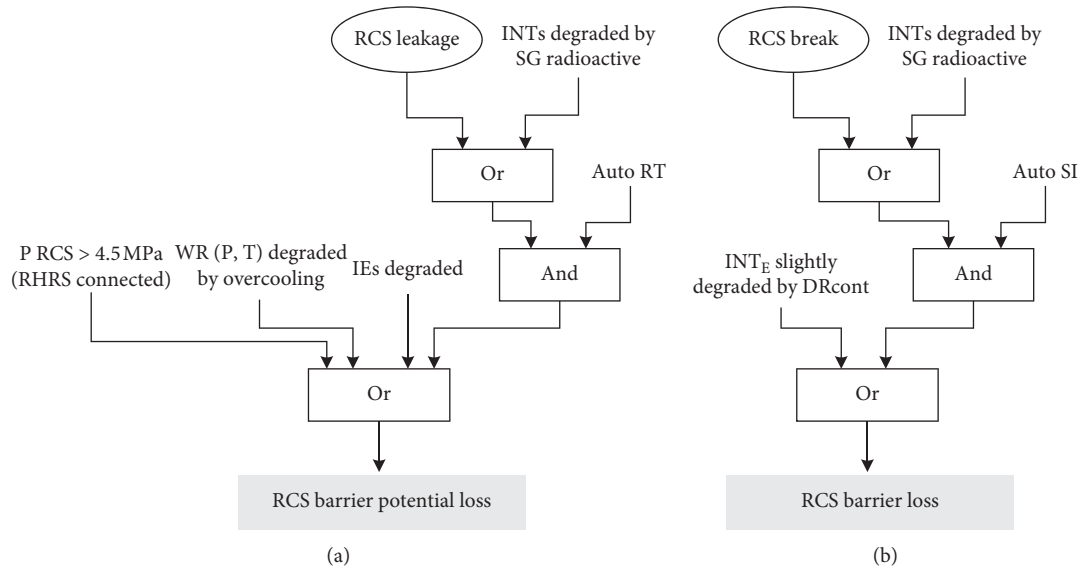
FIGURE 3: RCS barrier initial conditions.

pipelines, 4.5 MPa, is chosen as the criterion of RCS cold overpressure.

(3) Degradation of $IE_S$: It means that the residual heat cannot be effectively removed by SGs; continual heating of primary coolant will raise up the temperature and pressure of RCS and eventually lead to automatic actuation of pressurizer safety valves. In this condition, the "feed and bleed" strategy is anticipated in SOP; the volunteered open of pressurizer safety valves in this strategy indicates a potential loss of the RCS barrier.

(4) Leakage on RCS: It can be detected by leak balance test performed by operators if the leakage is high enough to actuate automatic reactor trip; it means that the leakage is so severe that actuation of reactor protection system is asked for; then this scale of leakage on RCS is considered as an initial condition of potential loss of RCS barrier. Similarly, if an SG is radioactive due to leakage on the U-tube, resulting in degradation of $INT_S$, and consequently automatic reactor trip is actuated, the condition is also regarded as potential loss of RCS barrier.

For loss of RCS barrier, the following initial conditions are identified:

(1) Slight degradation of $INT_E$ due to high dose rate in containment: If slight degradation of containment is caused by slightly high dose rate in containment, it means that a certain scale mass and energy release into containment is ongoing, which indicates the integrity of RCS has been lost. 0.02 Gy/h is chosen as the threshold of the slightly high dose rate, which corresponds to an instantaneous release of all reactor coolant mass into the containment assuming that reactor coolant activity equals 37GBq/t dose equivalent I-131.

(2) Break on RCS: Thanks to all the available parameters such as RPVL, $\Delta T$sat, and pressurizer water level, break on RCS can be detected by operators; if the break is large enough to actuate engineered safety features such as safety injection, then this scale of the break on RCS is considered as an initial condition of loss of RCS barrier. Similarly, if an SG is radioactive due to rupture of the U-tube, resulting in degradation of $INT_S$, and consequently safety injection is actuated, the condition is also regarded as loss of RCS barrier.

### 3.3. Containment Barrier.

The containment barrier consists of containment structure, containment isolation valves, and their upstream components, as well as the isolation valves on main steam lines and feedwater lines and their upstream components. For CPR1000 nuclear plants, the logical criteria related to state of containment barrier based on state functions are shown in Figure 4.

For potential loss of containment barrier, the following initial conditions are identified:

(1) Degradation of $INT_E$ due to high Pcont concurrent with failure of the containment spray system: If degradation of containment is caused by high containment pressure, it means that there is a large-scale mass and energy release in containment and containment spray is requested. 0.24 MPa, which corresponds to the setpoint pressure of containment spray automatic action, is chosen as the threshold of high Pcont. Due to the failure of containment spray, the heat continually cumulated in containment cannot be effectively removed and it may threaten the integrity of the containment.

(2) Pcont > limit pressure: If containment pressure is higher than 0.52 MPa, which is the designed limit pressure of containment, the integrity of containment will be aggressively challenged.

(3) SAMG criteria: It is synthesis information, which includes (A) the temperature criterion T RIC > 650°C, which means that the upper half of the fuel assemblies has been uncovered and nearly all the primary coolant has been released into containment; (B) hydrogen concentration exceeding 4%, which means that hydrogen accumulated in containment has exceeded the minimum explosion concentration and there is a risk of hydrogen deflagration threatening the integrity of containment; (C) DRcont higher than SA dose rate curve as shown in Figure 5, which means that a considerable proportion of fuel clad has been failed (about 10%~20%). In this condition, the fuel clad barrier and the RCS barrier must have been lost, and a major release of radioactive substances requiring off-site protective actions is anticipated (IAEA [20]); it is therefore prudent to take this condition as potential loss of containment barrier.

For loss of containment barrier, the following initial conditions are identified:

(1) Degradation of $INT_S$ due to SG radioactive and failure of the radioactive SG isolation: Leak or rupture of U-tube in an SG will lead to the SG radioactive; after identifying the radioactive SG, the operator will try to totally isolate it on both water side and steam side following the guidance of SOP, failure of the radioactive SG isolation means that there is a path for radioactive substances from RCS discharging into environment, and this condition is regarded as a typical example of loss of containment barrier.

(2) Failure of containment isolation: Actuation of containment isolation means that a considerable mass and energy release into the containment is expected following a break on the primary side or secondary side, and isolation of containment is requested as soon as possible. In this condition, however, if the operator estimates that containment isolation has been failed, then the containment is really bypassed and the integrity of containment is actually lost.

## 4. Construction of FPBMS

FPBMS, as an independent support system, will directly communicate with level 3 of DCS which is isolated from the terminal bus with a firewall, as shown in Figure 6, it is a one-way communication, data are only transmitted to FPBMS from level 3 of DCS, and FPBMS will never send any data to DCS, so as to avoid any unpredictable and adverse impact on the operation of DCS.

### 4.1. Signal Acquisition and Processing.

The input data obtained from DCS include the status of state functions themselves, parameters relative to state functions, and important signals (such as reactor trip signal and safety injection signal) as well as several critical instrument parameters; all these data are necessary for FPBMS to diagnose the status of FPBs.

As for instrument parameters, redundant signals are obtained from DCS and are processed in FPBMS to improve the robustness of the system. Taking P RCS as an example,

(a)                                                                                    (b)
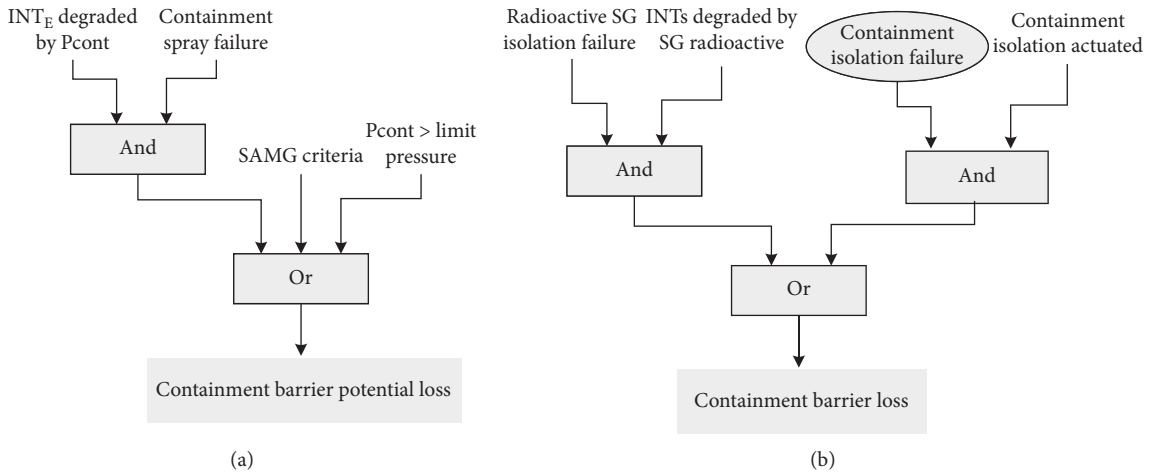
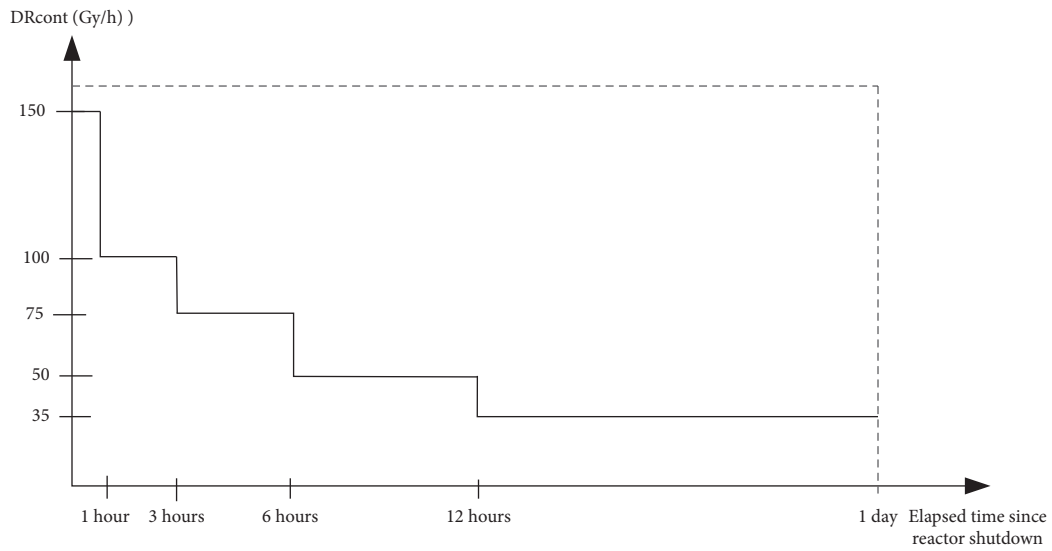FIGURE 4: Containment barrier initial conditions.
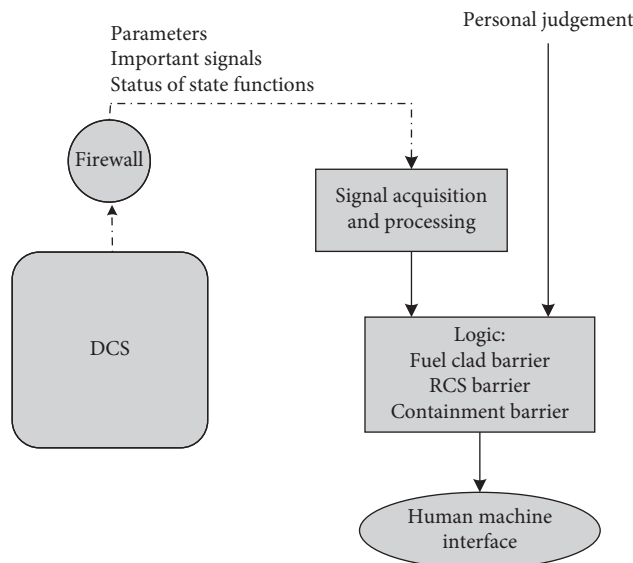


FIGURE 5: SA dose rate curve.
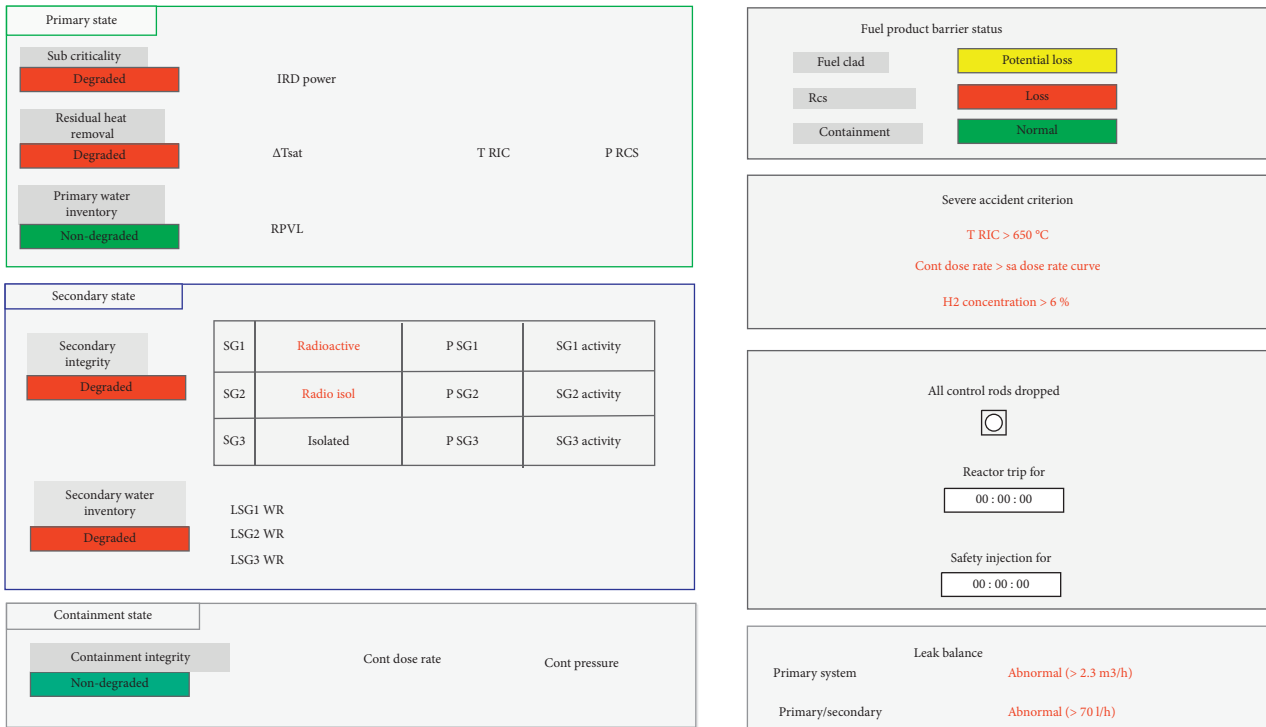


FIGURE 6: Interface with DCS.

FIGURE 7: Monitoring display.

four P RCS signals, individually assigned in four independent protection groups of the reactor protection system, along with their availability status are acquired by FPBMS, and then the maximum value of these signals is chosen as the representative P RCS value after eliminating invalid signals.

*4.2. Human-Machine Interface.* In FPBMS, three kinds of displays are provided for human-machine interface (HMI). (1) Monitoring display: it integrates states of state functions, parameters relative to state functions, and FPBs status on one monitoring display, as shown in Figure 7. (2) Breakdown displays: these displays are dedicated to visualizing the logics shown in Figures 1, 3, and 4, so that emergency personnel can track the source and find out the original initial conditions. (3) Control displays: considering that, under some complicated conditions, it is the duty of plant emergency director (PED) to judge the status of FPBs using all other available pieces of information, control displays provide an interface for PED to intervene in the logic process. It should be noted that the judgments made by operators (such as leakage or break on RCS), which have been confirmed on SOP control displays while implementing SOP to control the reactor state, are also acquired from DCS by FPBMS.

## 5. Verification and Validation

The verification and validation (V&V) of FPBMS is carried out thanks to the full scope simulator (FSS) of CPR1000 nuclear power plants. The operators, human factor engineers, technical engineers, and emergency response experts are all included in the V&V team. The technical engineers dedicate to integrating FPBMS into FSS, the operators control the reactor state following the guidance of SOP under accident scenarios simulated on FSS, all the accident scenarios are specially chosen if only they may threaten the integrity of one or more FPBs, the emergency response experts focus on FPBMS and identify the technical issues during the time, and the human factor engineers concentrate on the HMI issues.

Expected results are obtained via the V&V programs on FSS. Table 2 shows the sequence and results of a Fukushima-like accident (station blackout concurrent with turbine auxiliary feedwater pump failure); FPBMS indicates the first and second barrier potential loss at the time exhaustion of water inventory in SGs, which lead to degradation of $IE_S$. Potential loss of the third barrier is indicated when Pcont is over 0.24 MPa as containment spray is failed to actuate due to power loss, FPBMS indicates RCS barrier loss when T RIC is over 650°C because pressurizer relief valves are forced to open by operator just before transferring to SAMG.

We conclude that FPBMS, though several deficiencies remain, can be looked at as a real-time system that can reliably monitor the status of FPBs during accident evolvement. Loss or potential loss of the three FPBs can be dynamically indicated to help emergency response experts quickly and correctly determine the EALs. Since FSS is a little more different from the actual reactor characteristic, further V&V is expected to be carried out on the multiplant integrated real-time monitoring platform where the real-time operating data of all CPR1000 nuclear power plants are monitored.

TABLE 2: Sequence and result of station blackout.

| Time (h) | Sequence of transient | FPB status displayed on FPBMS | |
|---|---|---|---|
| 0 | Reactor trip | Fuel clad | Normal |
| | | Rcs | Normal |
| | | Containment | Normal |
| 1.6 | Exhaustion of water inventory in SGs | Fuel clad | Potential loss |
| | | Rcs | Potential loss |
| | | Containment | Normal |
| 2.0 | Core is beginning to uncover | Fuel clad | Potential loss |
| | | Rcs | Potential loss |
| | | Containment | Normal |
| 2.1 | Pcont is over 0.24 MPa | Fuel clad | Potential loss |
| | | Rcs | Potential loss |
| | | Containment | Potential loss |
| 2.5 | T RIC is over 650°C | Fuel clad | Loss |
| | | Rcs | Loss |
| | | Containment | Potential loss |

## 6. Conclusions and Prospects

As degradation of state functions defined in SOP substantially represents the challenges on fundamental safety functions and then on integrity of FPBs in like manner, for each FPB, we determine the initial conditions representing its loss or potential loss based on degradation of state functions as well as several other important parameters, by which the link between SOP and EALs is established; then, an intelligent FPBMS, aiming to dynamically monitor and indicate the status of FPBs during accident evolvement, is developed, verified, and validated. The pioneering work, by building bridges between state functions and initial conditions of FPBs and then computerizing them innovatively, proves that dynamical monitoring of the status of FPBs during accident evolvement and real-time indication of loss or potential loss of FPBs can be achieved, which may effectively alleviate the pressure on persons under accident conditions and effectively support decision-making of EALs after accidents.

As far as the FPBs themselves are concerned, EALs can be easily determined according to their status. In general, loss or potential loss of fuel clad barrier or RCS barrier will trigger "facility emergency," loss or potential loss of both will trigger "on-site emergency," confirming loss of two barriers, and potential loss of the third barrier will trigger "off-site emergency." However, it should be noted that recognition categories of EALs, besides FPBs, also include abnormal radiation levels (recognition category A), system malfunction (recognition category S), and hazards (recognition category H); FPBMS, as a pilot system, has proved that it is feasible to automate the decision-making process of EALs; we are looking forward to extending the function of FPBMS in further work, aiming to build an integrated intelligent EALs expert system by entirely integrating the initial conditions of all recognition categories of EALs into it.

## Abbreviations

S/K:          Subcriticality
WR (P, T):    Residual heat remove

P RCS:         RCS pressure
ΔTsat:         Subcooling margin
T RIC:         Temperature at core outlet
IE$_P$:        Primary water inventory
RPVL:          Reactor pressure vessel water level
IE$_S$:        Secondary water inventory
INT$_S$:       Secondary integrity
INT$_E$:       Containment integrity
Pcont:         Containment pressure
DRcont:        Containment dose rate.

## Data Availability

The data used in this paper are part of the plant design data, which are proprietary and cannot be disclosed.

## Conflicts of Interest

The authors declare that they have no conflicts of interest.

## References

[1] IAEA, *Arrangements for Preparedness for a Nuclear or Radiological Emergency (GS-G-2.1)*, IAEA, Vienna, Austria, 2007.

[2] IAEA, *Criteria for Use in Preparedness and Response for a Nuclear or Radiological Emergency (GSG-2)*, IAEA, Vienna, Austria, 2011.

[3] NNSA, *Nuclear Power Plant Emergency Management Regulations for Nuclear Accidents (HAF002)*, NNSA, Beijing, China, 1993.

[4] NNSA, *One of the Implementation Details of Regulations for Emergency Management for Nuclear Accidents, Emergency Preparedness and Response of Nuclear Power Plant (HAF 002/01)*, NNSA, Beijing, China, 1998.

[5] NEI, *Methodology for Development of Emergency Action Levels Advanced Passive Light Water Reactors*, NEI, Washington DC, USA, NEI 07-01, 2009.

[6] NEI, *Development of Emergency Action Levels for Non-Passive Reactors*, NEI, Washington DC, USA, NEI 99-01 Rev.6, 2012.

[7] Z. Q. Shi and J. F. Li, "Determining protective actions based on nuclear power plant conditions during a reactor accident," *Chinese Journal of Nuclear Science and Engineering*, vol. 21, no. 4, pp. 386–393, 2001.

[8] T. Liu, L. G. Zhang, and J. Y. Qu, "Methodologies for development of nuclear power plant emergency action level and their application," *Atomic Energy Science and Technology*, vol. 44, no. 4, pp. 456–459, 2010.

[9] T. Liu, "Study on nuclear power plant A recognition category emergency action level," in *Proceedings of the 18th International Conference on Nuclear Engineering(ICONE18)*, Xi'an, China, May 2010.

[10] F. He, H. Yu, and K. L. Mu, "System of generic criteria and operational criteria for nuclear and radiological emergency of HPR1000," *Nuclear Power Engineering*, vol. 39, no. 2, pp. 166–170, 2018.

[11] X. C. Zang, T. Liu, and J. J. Tong, "Suggestions on optimization method of emergency action level of advanced passive light reactor," *Nuclear Power Engineering*, vol. 39, no. S1, pp. 133–137, 2018.

[12] D. W. Faletti and J. D. Jamison, *Integration of Emergency Action Levels with Combustion Engineering Emergency Operating Procedures*, Pacific Northwest Labs., Richland, WA, USA, 1985.

[13] H. R. Yang, "Study on emergency action levels for Qinshan nuclear power plant," *China Nuclear Science and Technology Report*, vol. 20, no. 1, pp. 182–191, 2005.

[14] H. Yu, "Application of emergency operation procedure in establishing NPP emergency action level," *Nuclear Power Engineering*, vol. 36, no. 3, pp. 54–56, 2015.

[15] C. M. Zhang and C. Xu, "Application of initiating condition and emergency action level in NPP at ATWS," *Nuclear Power Engineering*, vol. 27, no. 6, pp. 66–69, 2006.

[16] Q. Chen, Q. M. Zhang, and L. Zhai, "Emergency classification level automatic judgment and warning system based on emergency action level of nuclear power plant," in *Proceeding of the 2018 International Conference on Power System Technology*, Guangzhou, China, November 2018.

[17] J. Mišák, *Development and Review of Plant Specific Emergency Operating Procedures*, IAEA, Vienna, Austria, 2006.

[18] Z. X. He, J. H. Yu, X. F. Li et al., "Design of cooling monitoring system based on SOP," *Nuclear Power Engineering*, vol. 33, no. 5, pp. 107–110, 2012.

[19] Z. Y. Wang, R. S. Li, K. B. Sun et al., "Dimension of the forced vessel water level based on subcooling margin of core outlet coolant in CPR1000 nuclear power plants," *Energy Procedia*, vol. 127, pp. 103–109, 2017.

[20] IAEA, *Generic Assessment Procedures for Determining Protective Actions during a Reactor accident (TECDOC-955)*, IAEA, Vienna, Austria, 1997.

*Research Article*

# Assessment of Cesium Compound Behavior during Simultaneous Failure of Reactor Pressure Vessels and Spent Fuel Pools Using Modified ART Mod 2: Fukushima Daiichi Accident Simulation

**Wasin Vechgama** [1] **and Kampanart Silva** [2]

[1]*Environment Technology Section, Nuclear Technology Research and Development Center,*
 *Thailand Institute of Nuclear Technology (Public Organization), 16 Vibhavadi-Rangsit Road, Lat Yao, Chatuchak,*
 *Bangkok 10900, Thailand*
[2]*Renewable Energy and Energy Efficiency Research Team, National Energy Technology Center,*
 *114 Thailand Science Park, Phahonyothin Road, Khlong Nueng, Khlong Luang, Pathum, Thani 12120, Thailand*

Correspondence should be addressed to Wasin Vechgama; wasinvechgama@gmail.com

To support the regional strategy development of ASEAN NPSR using scientific research, Modified ART Mod 2 has been used to assess the fission product release from RPVs and SFPs independently. However, the Fukushima Accident suggested the possibility of simultaneous release from RPV and SFP which indicated the necessity of re-evaluation of the maximum source term. The objective was to assess the fission product behavior during a simultaneous failure in RPVs and SFPs of BWR type with Mark I containment design in multiple units using Modified ART Mod 2 in order to evaluate the maximum source term. The releases of cesium compounds in gas and aerosol forms from RPVs and SFPs of Units 1–3 of the Fukushima Daiichi NPP were selected as the case studies. It was found that the behavior of cesium compounds was mainly governed by the aerosols and atmospheric temperatures, which resulted in different characteristics in adsorption and thermophoresis. It also turned out that the simulation of a simultaneous release led to a smaller release than the summation of independent simulations of releases from RPV and SFP by 25%. This study helped estimate the maximum consequences in order to be able to effectively design the EPR for NPP accidents inside or outside the ASEAN region.

## 1. Introduction

It is well known that a severe accident in Nuclear Power Plants (NPPs) is one of the technological disasters affecting people and the environment worldwide [1]. This essentially means whether or not the country uses nuclear energy; it has the potential to be influenced by NPP incidents. The Association of Southeast Asian Nations (ASEAN) is one of the regional entities that concern about the radioactive effects from possible severe accidents in NPPs [2]. Although NPPs have never been operated in ASEAN countries, knowledge of nuclear safety analysis and assessments of nuclear severe accident consequences are still needed to design a regional plan for preventing, mitigating, and managing potential

severe accidents in NPPs located around the region. These concerns of nuclear accident consequences lead to the establishment of the ASEAN Network on Nuclear Power Safety Research (ASEAN NPSR) whereby researchers and engineers in the field of nuclear power safety can jointly conduct research and derive findings from a regional standpoint. The goal of ASEAN NPSR is to strengthen Research and Development (R&D), Human Resource Development (HRD), and regional cooperation in the field of nuclear power safety in ASEAN in order to support the formulation of the regional strategy for accident management [2]. Therefore, ASEAN NPSR continuously promotes collaborative studies that contribute to the planning of Emergency Preparedness and Response (EPR) against NPP

accidents, starting from probable accidents in NPPs located around the region, in order to effectively protect people and the environment from nuclear severe accident consequences.

The first project of the ASEAN NPSR on transboundary atmospheric dispersion assessment of fission product release has continued with active participation from the ASEAN Member States over past years to together support the formulation of ASEAN EPR using scientific research data. In this project, the information on the amount and timeline of the radioactive release from NPPs, the so-called source term, is the main input data for the transboundary atmospheric dispersion assessment. Source term data has been obtained from a publicly available domain such as State-of-the-Art Reactor Consequence Analyses (SOARCA) [3]. SOARCA studied the radioactive effects of severe accidents in a representative Boiling Water Reactor (BWR) and Pressurized Water Reactor (PWR). Adopting source term data from SOARCA has two important drawbacks. The first one is that the core inventory is not that of the NPPs of interest, and the other is that only accidents caused by Reactor Pressure Vessel (RPV) failure in a single unit are taken into account. However, after the accident at the Fukushima Daiichi Nuclear Power Plant (1FNPP) in Japan happened, a concern on a multiunit accident of NPPs has become larger than that of a single-unit accident [4]. Consideration of the multiunit accident leads to a more comprehensive accident management strategy that covers the management of severer cases [5]. Looking back to ASEAN, NPPs around the region were built in the form of multiple units such as the Fangchenggang Nuclear Power Plant in China [6]. Thus, the use of source term data from SOARCA as the input data for the atmospheric dispersion calculation may be irrelevant. It is important that ASEAN has a regional capability to assess the source term data by itself in order to evaluate fission product release from a multiple-unit accident in an external location, which will be an important input for the transboundary atmospheric dispersion assessment.

After the accident in the 1FNPP, Tokyo Electric Power Company (TEPCO) put a large effort into the study of the behavior of the reactor core and the RPV and other essential components and examine unsolved issues from accident progression of Units 1–3 of 1FNPP [7]. Units 1–3 of 1FNPP are BWR technology with Mark I containment design in which Unit 1 is an earlier BWR/3 design while Units 2 and 3 are BWR/4 designs [8]. TEPCO aimed to disclose the complete picture of this severe accident and contribute to the improvement of the safety systems of the 1FNPP. Modular Accident Analysis Program 5 (MAAP5) [9] was the main accident analysis code that TEPCO used to analyze accident progression. An accident in Spent Fuel Pools (SFPs) was another major concern for 1FNPP because there were a lot of spent fuels in it which could damage and resulted in fission product release to the environment. Although severe damage of fuel assemblies in the SFP of all units of 1FNPP was not the main concern, the possibility of such accidents was recognized and thus studies on potential radioactive release from SFPs of 1FNPP were widely conducted. Oak Ridge National Laboratory (ORNL) performed the

simulation of the SFP of Unit 4 which is the largest source of the spent fuels in the 1FNPP using the Oak Ridge Isotope GENeration (ORIGEN) code [10] whereby the deviation of thermal-hydraulic conditions was studied [11]. In 2018, the simulation of the inherent response of the SFPs of 1FNPP was conducted to analyze the influence of loss of cooling accident in the SFPs using MAAP 5.02 [12] in order to enhance the safety systems of the SFPs [13]. In the aspect of Probabilistic Risk Assessment (PRA) research, level 1 and level 2 PRAs of Mark I BWR which is the reactor type of 1FNPP were redone to calculate core damage frequency (CDF) and large release frequency (LRF) during the decommissioning state using accidents occurring in both RPVs and SFPs [14]. As for level 3 PRA, multiunit level 3 PRA was conducted based on conservative assumptions to estimate multiunit risk and to understand the risk characteristics in a multiunit context [4]. Therefore, in order to be able to consider consequences from the maximum radiological release from an NPP accident, it is necessary to consider the risks associated with both RPVs and SFPs in a multiunit accident [15]. It is obvious from these previous studies that there is a chance of a multiunit accident with simultaneous failure of RPVs and SFPs in NPP accidents. However, currently, studies on such accidents are limited. This implies the necessity of a study of a simultaneous failure in a multiunit accident in order to reinforce the awareness of stakeholders and strengthen the EPR planning.

Thailand has been using the code of Analysis of Radioactive nuclide Transport and deposition/Modification 2 (ART Mod 2) [16] of the Japan Atomic Energy Agency (JAEA) to conduct the source term analysis since 2015. ART Mod 2 code was modified and validated for the evaluation of fission product behavior of cesium compounds from RPVs into Primary Containment Vessels (PCVs) [17]. Four models of aerosol deposition phenomena were validated in order to increase the accuracy of the calculation, namely, gravitational settling, Brownian diffusion, diffusiophoresis, and thermophoresis. Next, Modified ART Mod 2 was applied to a study of cesium compound behavior in the SFP of the Robert Emmett Ginna Nuclear Power Plant in the USA, in the case of complete loss of cooling water [18]. Then, Modified ART Mod 2 was verified for the evaluation of fission product release of cesium compounds from SFP into PCV of Unit 3 of 1FNPP [19]. However, Modified ART Mod 2 has never been used to assess the fission product behavior in a complete accident system which includes the failures of RPVs and SFPs in multiple units.

The objective of this paper is to evaluate the fission product behavior of the cesium compounds in gas and aerosol forms during a simultaneous failure of RPVs and SFPs of BWR type with Mark I containment design in multiple units using Modified ART Mod 2 code. Also, this study is used to confirm the ability of Modified ART Mod 2 to provide the source term data of a release from the PCV to the environment for the transboundary atmospheric dispersion assessment under ASEAN NPSR. Cesium compounds are selected as representative radioactive materials for this study because they are the major radioactive compounds that have long-term effects on people and the environment due to the thirty-year half-life of

cesium [20]. In this paper, cesium iodide (CsI) in gas form and cesium hydroxide (CsOH) in aerosol form are selected as the representative compounds because they are the majority of the cesium release after NPP accidents [13, 21]. This study considers gaseous CsI because iodine ($I_2$) gas has a chance to take a chemical form of CsI gas during severe accidents [22]. CsOH is in aerosol form because a large amount of CsOH aerosols from the reactor core deposit on surface structures of NPP in the experiment [23]. Accident of Units 1–3 of 1FNPP, that is, BWR type with Mark I containment design, is selected to be the representative accident because it was suspected to experience molten core in the RPVs and fuel damage in the SFPs during the initial phase of the examination of the 1FNPP after the accident [24]. This paper is divided into five parts. This part is the introduction and background. The second part is the information on the gas and aerosol deposition models of Modified ART Mod 2. The third part is the methodology and simulation conditions. The fourth part is the results and discussions. The last part is the conclusions.

## 2. Gas and Aerosol Deposition Models in Modified ART Mod 2

Modified ART Mod 2 is a tool for calculating the transportation and deposition of the fission product release. In Modified ART Mod 2, fission product types are characterized into two forms including gas and aerosol forms. Figure 1 shows the characteristic of deposition phenomena of gas and aerosol in Modified ART Mod 2.

As for the gaseous fission products, models for condensation and adsorption are considered to evaluate fission product behavior only at the wall surface [16], while the aerosol fission products consider deposition on both the wall and the floor [17]. Phenomena of Brownian diffusion, diffusiophoresis, and thermophoresis are used to illustrate the aerosol deposition on the wall. Only gravitational settling is considered for the aerosol deposition on the floor in Modified ART Mod 2.

### 2.1. Gas Deposition Models

2.1.1. Condensation. Condensation of the fission product in gas form occurs from differences between partial pressure and saturated vapor pressure in the system. Model of condensation velocity ($v_{cond}$) (cm/s) is used to represent the gas deposition on the wall as follows:

$$v_{cond} = \frac{D_g^k}{(1 - \gamma_g)\delta_D} \left(1 - \frac{\gamma_g^{k(s)}}{\gamma_g^k}\right), \quad (1)$$

where $D_g^k$ is the diffusion coefficient of the radionuclides ($cm^2/s$), $\delta_D$ is the thickness of the boundary layer (cm), $\gamma_g$ is the ratio of partial pressure without the radionuclides (-), $\gamma_g^k$ is the ratio of partial pressure without the radionuclides of the total pressure (-), and $\gamma_g^{k(s)}$ is the ratio of saturated pressure without the radionuclides of the total pressure (-).

2.1.2. Adsorption. Adsorption depends on a physical reaction between radionuclides and the material surface under high-temperature conditions. In the code, the only physical adsorption without chemical interactions will be considered in the deposition on the wall. Gas deposition on the wall due to adsorption velocity ($v_{ads}$) (cm/s) is calculated using the model as follows:

$$v_{ads} = A_0 \exp\left(-\frac{\varepsilon_a^k}{k_B T_{surf}}\right), \quad (2)$$

where $A_0$ is the velocity constant of the radionuclides (cm/s), $\varepsilon_a^k$ is the activation energy of reaction of the radionuclide (erg), $k_B$ is the Boltzmann constant (erg/(K.g)), and $T_{surf}$ is the temperature of the surface ($T$).

### 2.2. Aerosol Deposition Models

2.2.1. Gravitational Settling. Aerosol deposition velocity due to gravitational settling ($v_{gra}(r_p)$) (cm/s) is derived from the drag force of the aerosol surface. In the code, the only aerosol form of fission product release will be considered as the deposition on the ground or liquid surface in the water environment. The deposition velocity of gravitational settling is a function that depends on the Reynolds number (Re). In the case of Re smaller than one, the aerosol deposition velocity is determined by the Stokes approximation. As for the case of Re larger than one, the aerosol deposition velocity is determined by Newton's approximation as follows:

$$v_{gra}(r_p) = \begin{cases} \dfrac{2r_p^2 g(\rho_p - \rho_g)}{9\mu_g} Cu(r_p), & Re < 1, \\[2mm] \dfrac{\mu_g Re}{2r_p \rho_p}, & Re > 1, \end{cases} \quad (3)$$

where $r_p$ is the radius of aerosol (cm), $g$ is the gravitational acceleration ($cm/s^2$), $\rho_p$ is the density of aerosol ($g/cm^3$), $\rho_g$ is the density of the gas ($g/cm^3$), $Cu(r_p)$ is the Cunningham factor (-), and $\mu_g$ is the viscosity of gas ($dyn.s/cm^2$).

2.2.2. Brownian Diffusion. Aerosol deposition velocity due to Brownian diffusion ($v_{diff}(r_p)$) (cm/s) can be modeled from an empirical model considering the turbulent damping process under the condition of upward flow direction in a vertical duct as follows:

$$v_{diff}(r_p) = \begin{cases} 0.0899\, Sc^{-0.704} u_\tau; & \tau^+ < 0.2, \\[1mm] 3.25 \times 10^{-4} \tau^{+2} u_\tau; & 0.2 < \tau^+ < 22.9, \\[1mm] 0.17 u_\tau; & \tau^+ > 22.9, \end{cases} \quad (4)$$

where $\tau^+$ is the dimensionless particle relaxation time (−), Sc is the Schmidt number (−), and $u_\tau$ is the friction velocity (cm/s).
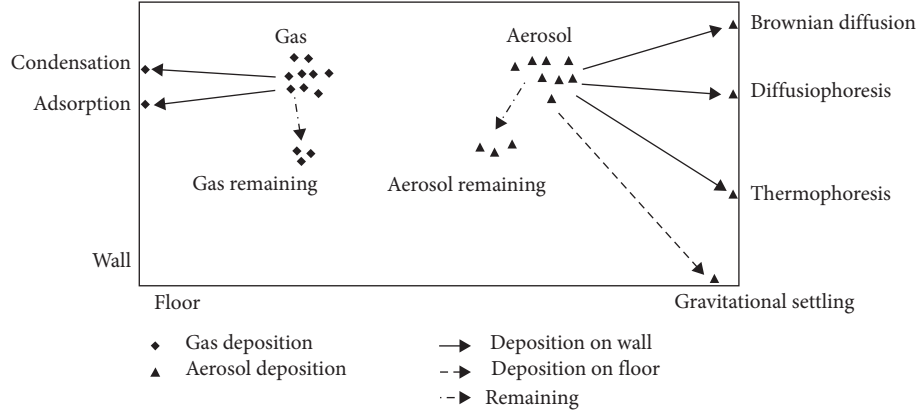
FIGURE 1: Characteristic of deposition phenomena of gas and aerosol forms in Modified ART Mod 2.

*2.2.3. Diffusiophoresis.* Diffusiophoresis is affected by the flow of the condensing steam and partial pressures of noncondensable gas near the structure surface. Thus, the aerosol deposition velocity of diffusiophoresis ($v_{\text{diffph}}(r_p)$) (cm/s) consists of both velocity of Stephan flow and gas momentum transfer as follows:

$$v_{\text{diffph}}\left(r_p\right) = U_c + \frac{\text{Cu}\left(r_p\right)}{\chi} \frac{\sqrt{m_s}}{\gamma_s \sqrt{m_s} + \gamma_a \sqrt{m_a}} \gamma_a U_c, \quad (5)$$

where $m_s$ is the molecule weight of steam (g), $m_a$ is the molecule weight of noncondensible gas (g), $\gamma_s$ is the mole fraction of steam (-), $\gamma_a$ is the mole fraction of non-condensible gas (-), $U_c$ is the velocity of condensing steam (cm/s), and $\chi$ is the shape factor (-).

*2.2.4. Thermophoresis.* Aerosol deposition velocity due to thermophoresis ($v_{\text{ther}}(r_p)$) (cm/s) is controlled by the difference of temperature gradients. The model of thermophoresis is generated by Monte-Carlo type numerical modeling as follows:

$$v_{\text{ther}}\left(r_p\right) = \frac{2v_g \text{Cu}\left(r_p\right)\left(\lambda_g + C_t \text{Kn} \lambda_p\right)\left(1 + \left(9\,\text{Kn}/\left(4 + (\pi/2)\right)\right)\right)}{T_g \left(1 + 3C_m \text{Kn}\right)\left(2\lambda_g + \lambda_p + 2C_t \text{Kn} \lambda_p\right)} \nabla T_g,$$

$$(6)$$

where $v_g$ is the dynamic viscosity of gas (cm²/s), $\lambda_g$ is the conductivity of mixed gas (erg/(K.cm.s)), $\lambda_p$ is the conductivity of aerosol (erg/(K.cm.s)), $C_t$ is the coefficient of the energy exchanges between the aerosol and gas (-), $C_m$ is the coefficient of the momentum exchanges between the aerosol and gas (-), Kn is the Knudsen number (-), and $\nabla T_g$ is the gradient of the temperature of the gas (K).

## 3. Methodology

In this paper, the release of CsI in gas form and CsOH in aerosol form from both the RPVs and the SFPs into the environment was assessed using hypothetical failure events of RPVs and SFPs of Units 1–3 of 1FNPP. Modified ART Mod 2 was used to simulate the accidents to study the fission product behavior in three cases including (1) a failure of RPVs (reference case), (2) independent failures of RPVs and SFPs, and (3) a simultaneous failure of RPVs and SFPs.

*3.1. Case 1: Failure of RPVs (Reference Case).* The first case was the simulation of the release of CsI gases and CsOH aerosols from RPVs of Units 1–3 of 1FNPP to PCVs, the fifth floor of Reactor Buildings (RBs), and the environment, respectively. This case was set to be a reference case for the comparisons in the following cases. Figure 2 shows the nodalization and flow directions of the first case. 13 volumes were used to represent the RPVs, the PCVs, the SFPs, and the RBs of Units 1–3 as well as the environment around the units. In this case, the fission product release of cesium compounds in each unit was transferred from the RPV into the PCV, the RB, and the environment, respectively. There is no consideration of the release from the SFPs. The geometry of each volume in Modified ART Mod 2 was determined based on the design of Units 1–3 [25–27], though all volumes were assumed to be in a cylindrical shape. Table 1 shows the geometry parameters for Modified ART Mod 2.

Regarding the source term from the RPVs, the amounts of CsI gas and CsOH aerosols were defined by multiplying the amount of cesium-137 (Cs-137) inventory in the core of Units 1–3 of 1FNPP [28] to the release fraction of CsI gas and CsOH aerosols calculated by TEPCO [29]. The radioactive cesium compounds release from the center of the RPVs of Units 1–3 which are represented by Volume 1, Volume 5, and Volume 9, respectively. Table 2 shows the cesium source term in the RPVs used as the inputs for Modified ART Mod 2. In this study, the aerosol size for all simulations was designed to match the aerosol distribution at the beginning of the aerosol phase, where aerodynamic mass median diameter (AMMD) and geometric standard deviation (GSD) are set to 3.35 and 1.5, respectively [30]. Aerosol mass distribution is assumed to follow log-normal approximation. As Modified ART Mod 2 requires ten representative values for aerosol diameters [16], ten different percentile values were selected to represent the CsOH aerosol sizes as shown in Table 3.

Thermal-hydraulic conditions during the accident in Units 1–3 of 1FNPP which affect the transportation and deposition of cesium compounds, including temperatures,
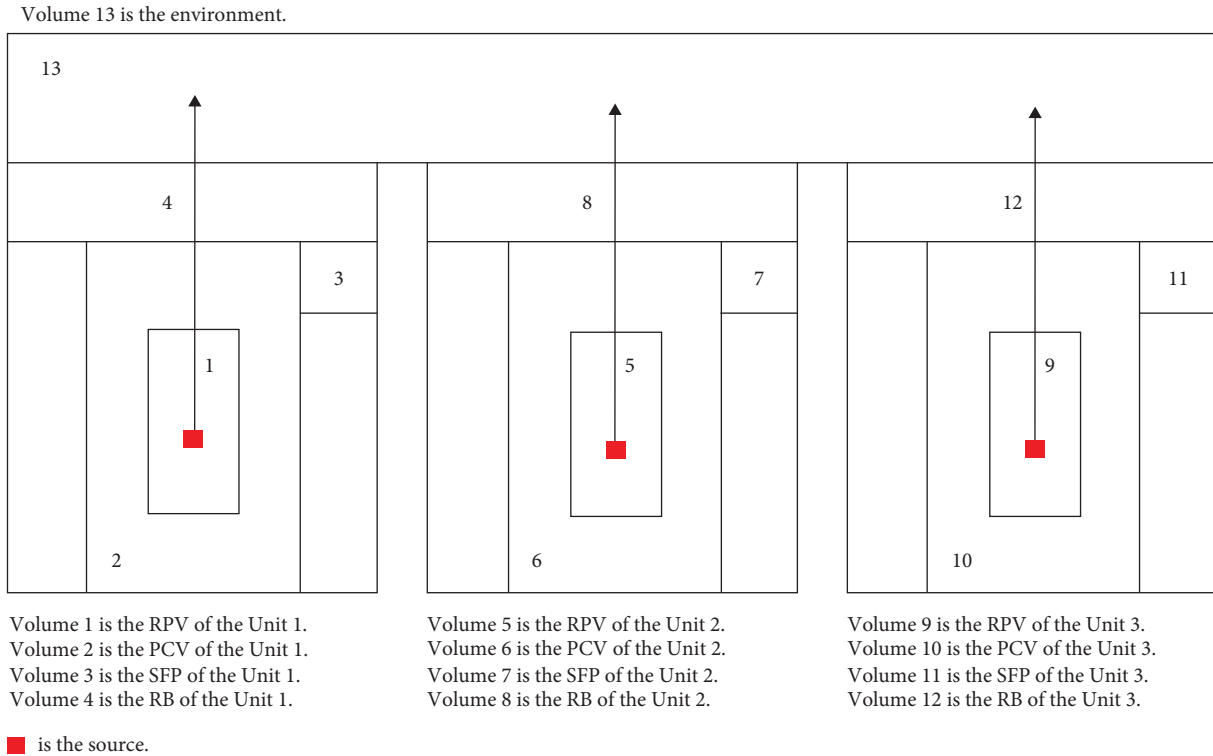
Volume 13 is the environment.



Volume 1 is the RPV of the Unit 1.
Volume 2 is the PCV of the Unit 1.
Volume 3 is the SFP of the Unit 1.
Volume 4 is the RB of the Unit 1.

Volume 5 is the RPV of the Unit 2.
Volume 6 is the PCV of the Unit 2.
Volume 7 is the SFP of the Unit 2.
Volume 8 is the RB of the Unit 2.

Volume 9 is the RPV of the Unit 3.
Volume 10 is the PCV of the Unit 3.
Volume 11 is the SFP of the Unit 3.
Volume 12 is the RB of the Unit 3.

■ is the source.

Figure 2: Nodalization and flow directions of case 1 (reference case).

Table 1: Inputs for geometry determination in Modified ART Mod 2.

| Volume no. | Diameter (cm) | Height (cm) | Cross-section area (cm$^2$) | Volume (cm$^3$) |
|---|---|---|---|---|
| 1 | $4.82E+02$ | $1.90E+03$ | $1.81E+05$ | $3.44E+08$ |
| 2 | $1.40E+03$ | $3.20E+03$ | $1.54E+06$ | $4.92E+09$ |
| 3 | $1.11E+03$ | $1.18E+03$ | $9.59E+05$ | $1.13E+09$ |
| 4 | $4.00E+03$ | $5.00E+02$ | $1.16E+07$ | $6.28E+07$ |
| 5 | $5.50E+02$ | $2.10E+03$ | $2.37E+05$ | $4.99E+08$ |
| 6 | $1.55E+03$ | $3.40E+03$ | $1.89E+06$ | $6.41E+09$ |
| 7 | $1.11E+03$ | $1.18E+03$ | $9.59E+05$ | $1.13E+09$ |
| 8 | $4.64E+03$ | $5.00E+02$ | $1.57E+07$ | $8.31E+09$ |
| 9 | $5.50E+02$ | $2.10E+03$ | $2.37E+05$ | $4.99E+08$ |
| 10 | $1.55E+03$ | $3.40E+03$ | $1.89E+06$ | $6.41E+09$ |
| 11 | $1.11E+03$ | $1.18E+03$ | $9.59E+05$ | $1.13E+09$ |
| 12 | $4.64E+03$ | $5.00E+02$ | $1.57E+07$ | $8.31E+09$ |
| 13 | $4.00E+06$ | $5.00E+05$ | $1.26E+13$ | $6.28E+18$ |

Table 2: Cesium source term in the RPVs for the calculation in Modified ART Mod 2.

| Initial source | Unit | Volume no. | CsI gas (Bq) | CsOH aerosols (Bq) |
|---|---|---|---|---|
| RPV | 1 | 1 | $2.03E+15$ | $3.55E+14$ |
| RPV | 2 | 5 | $4.10E+14$ | $4.10E+14$ |
| RPV | 3 | 9 | $3.62E+14$ | $3.01E+14$ |

pressures, and hydrogen (H$_2$) gas flows, refer to the TEPCO reactor core condition report of Units 1–3 of 1FNPP [29]. Only the wall temperature of the RPV within Unit 3 came from the study of Paul Scherrer Institute (PSI) [31]. Figures 3(a)–3(c) show the temperatures of gas and aerosols of cesium compounds, the RPV walls, and the PCV walls of

Units 1–3 used in the calculation. Figures 4(a) and 4(b) show the pressures in the RPVs and the PCVs of Units 1–3. Figure 5 shows the volumetric flow rates of H$_2$ gas from the RPVs of Units 1–3. Temperatures and pressures of the RBs and the environment were set at 298 K and 0.1 MPa to represent surrounding conditions.

Regarding the simulation timeline, the total time of simulation is 87 hours from 12.00 a.m. of March 11, 2011, to 03.00 p.m. of March 15, 2011, to cover the early phase of the release from Units 1–3. Unit 1 started to leak from a Safety Relieve Valve (SRV) 15 hours after the initiation of the accident. Then, the fission products started to leak from the PCV into the RB and the environment until the H$_2$ explosion happened at the 25th hour. Unit 2 started to leak from the SRV at the 77$^{th}$ hour. Unit 3 started to leak from the SRV at

TABLE 3: Representative CsOH aerosol sizes for the calculation in Modified ART Mod 2.

| Percentile | Representative aerosol diameters ($\mu$m) |
|---|---|
| 5 | 1.72 |
| 15 | 2.20 |
| 25 | 2.55 |
| 35 | 2.87 |
| 45 | 3.18 |
| 55 | 3.53 |
| 65 | 3.92 |
| 75 | 4.40 |
| 85 | 5.10 |
| 95 | 6.53 |

the 42nd hour into the RB and the environment until the $H_2$ explosion happened at the 68th hour.

*3.2. Case 2: Independent Failures of RPVs and SFPs.* In the second case, independent releases of cesium compounds from the SFPs were considered in addition to the first case. Figure 6 shows the timeline and release pathways of the second case. The release of radioactive materials from the SFPs was assumed to occur independently from the release from RPVs. The release of cesium compounds from the SFPs of Unit 1 and Unit 3 was assumed to start after the $H_2$ explosion which was the cause of the collapse of the fifth floor of RBs [32] and the rapid loss of coolant in the SFPs [11]. Only the SFPs of Unit 1 and Unit 3 where $H_2$ explosions occurred during the accident were assumed as the sources of release. Nodalization of this case was set using 13 volumes like the first case. But in this case, there were two release pathways. From Figure 6, the first pathway was from the RPV as in the first case. The second release was from the SFP into the RB and the environment, respectively. Figure 7 shows the nodalization and flow directions of the second case. The amounts of CsI gas and CsOH aerosols being released from the SFPs of Unit 1 and Unit 3 were defined by multiplying the cesium-137 inventory in SFPs of 1FNPP [32] to the same fractions of the release from the RPVs. Table 4 shows the cesium source term in the SFPs used for calculation in Modified ART Mod 2.

Thermal-hydraulic conditions for Modified ART Mod 2 code were set based on the simulation data during the complete loss of water from the study of inherent nuclear-spent fuel pool response to a loss of pool cooling accident [13] since it was modeled based on the behavior of spent fuels within the SFPs of 1FNPP. Figures 8(a) and 8(b) show the temperatures of the gas and aerosols of cesium compounds and the SFP walls used in the calculation. Figure 9 shows the volumetric flow rates of $H_2$ gas from the SFPs of Unit 1 and Unit 3 to the RBs. The pressures within the SFPs of the two units were set 0.1 MPa like the RBs and the environment because they were linked to each other.

*3.3. Case 3: Simultaneous Failure of RPVs and SFPs.* The third case aims to model the possible conditions of a simultaneous failure of RPVs and SFPs in multiple units to investigate the

consequences [32]. It resembled the second case, except that it considered the transportation of cesium compounds between the RPV and the SFP of each unit. The PCVs nearby the SFPs are an important part to link the transportation of cesium compounds between the RPVs and the SFPs. The volumetric flow rates and thermal-hydraulic conditions of this case were set to be the same as the second case, except that the interactions between Volumes 2 and 3, Volumes 6 and 7, and Volumes 10 and 11 were considered. Figure 10 shows the nodalization and flow directions of the third case.

## 4. Results and Discussion

*4.1. Case 1: Failure of RPVs (Reference Case).* Figure 11 shows the accumulative release of Cs-137 from the RPVs of Units 1–3 into the environment illustrated by Modified ART Mod 2 for the first case. It was found that the total of cesium-137 released at 87 hours after the initiation of the accident was $2.03E + 14$ Bq. This was compared to the simulated total Cs-137 release based on the Fukushima monitoring data in Figure 11 [33, 34]. It was found that the summation of the accumulative releases of cesium-137 of Units 1–3 simulated by Modified ART Mod 2 was slightly lower than the monitoring data.

The main reason for the underestimation could be the assumption of single point source release in Modified ART Mod 2 [16], which essentially means multiple release points from a single volume cannot be modeled. However, in the real situation, it is highly likely that the radioactive materials release from multiple points due to multiple locations of cracked and molten fuels [35]. The results of Modified ART Mod 2 were considered acceptable as the reference case because the major part of the results was in the same order of magnitude as Terada et al. [33] and was smaller than Katata et al. [34] by only one order of magnitude.

Next, Figure 12 shows the accumulative release of CsI gas and CsOH aerosols from Units 1–3 in the first case. It was found that the CsI gas was the major part of the release to the environment, while the released CsOH aerosols were only in the order of $10^{-8}$ of the total initial CsOH aerosols of Units 1–3. The majority of the CsOH aerosols tended to deposit in the units. The results are consistent with the studies of thermodynamic and kinetic studies of iodine and cesium transport in a nuclear severe accident at high temperatures [36]. This study showed that iodine and cesium had the potential to react with vapor and other iodine compounds to form CsI and CsOH in which more CsI tended to release into the ambiance than CsOH at high temperature due to different molecule structures. The results of Modified ART Mod 2 were also consistent with the studies by MAAP [29] and MELCOR 2.1 [31] where the majority of the CsOH aerosols deposited in the plants. However, the releases into the environment in MAAP and MELCOR 2.1 were around 1–2 percent which is much larger than the estimation of Modified ART Mod 2. This is again attributed to the assumption of single point source release in the code that affected the deposition rate and consequently the release of CsOH aerosols. On the other hand, in MAAP and MELCOR 2.1, fuels can be divided into multiple cells. This enables the
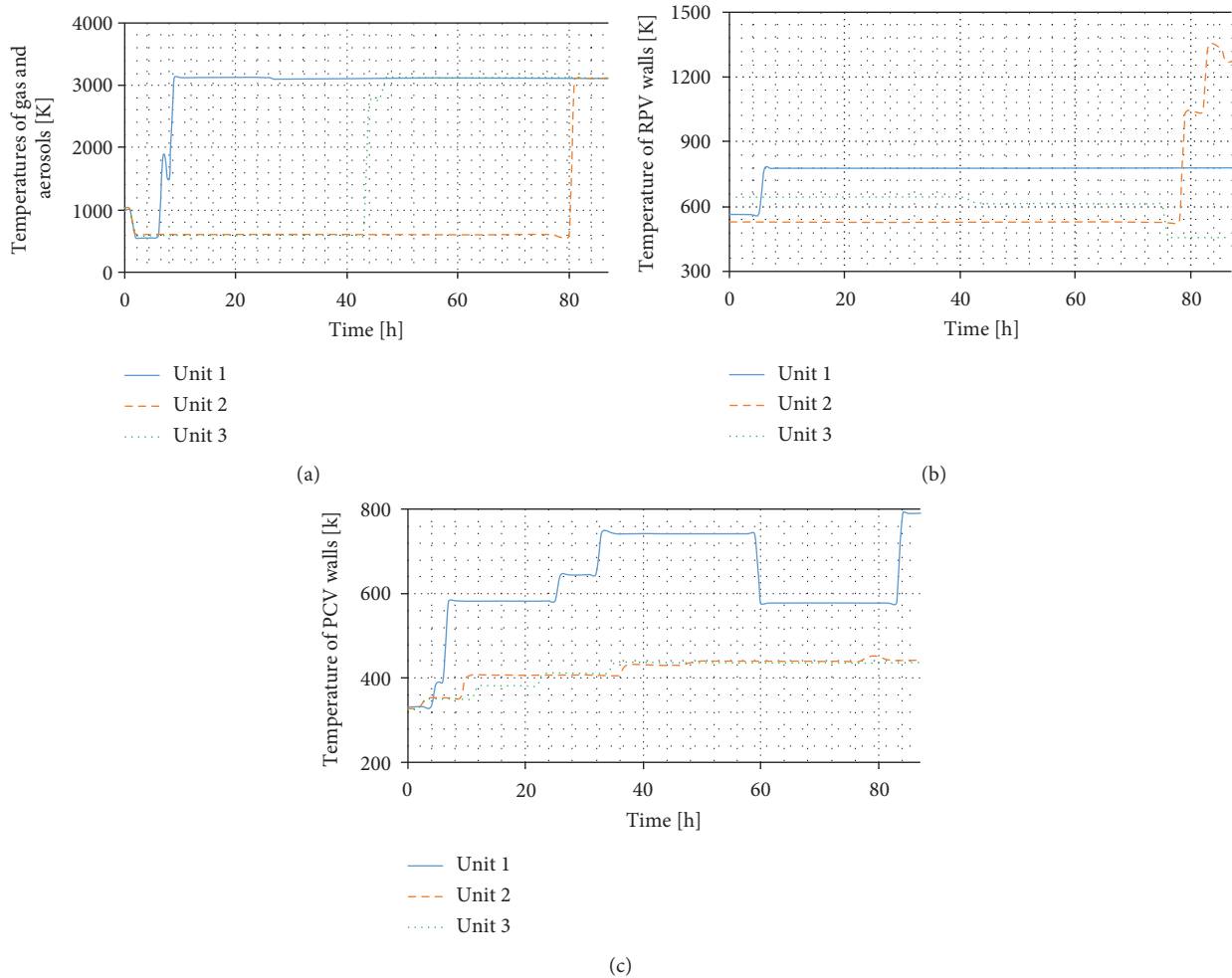
FIGURE 3: Conditions of the temperatures of Units 1–3 for Modified ART Mod 2 code: (a) gas and aerosols, (b) the RPV walls, and (c) the PCV walls.

simulation of multiple point source releases which is closer to the actual condition [13, 37]. It remained as a future task for Modified ART Mod 2 development to enable handling of multiple point source releases which would increase the accuracy of environmental source term prediction.

Since the deposition of cesium compounds directly affected the amount of release into the environment directly, contributions of different deposition phenomena to the deposition of CsI gas and CsOH aerosols in each volume were summarized in Tables 5 and 6, respectively. It was found that the CsOH aerosol deposition was attributed to only three phenomena, namely, gravitational settling on floors, Brownian diffusion on walls, and thermophoresis on walls. As for the CsI gas, only the adsorption phenomenon affected its deposition on walls. In this study, the releases of gas and aerosols from the molten core were assumed not to deposit on the floor of the RPVs especially volatile fission products [38] in order to maintain conservatism [39]. Thus, gravitational settling was considered only in volumes other than the RPVs. Diffusiophoresis of CsOH aerosols and condensation of CsI gas did not contribute to depositions on walls because the high temperature resulted in the decrease

in factors driving the two phenomena such as the diffusion coefficient and the fractions of steam and air [16]. For CsOH aerosols deposition on walls, thermophoresis was more dominant than Brownian diffusion since high temperature contributed to large temperature gradients which induced the particle deposition on the wall from thermophoresis [40, 41], especially in the RPVs. A small contribution of Brownian diffusion indicated that the influence of the turbulent damping process could be significantly decreased if a large temperature gradient existed in the system [42]. Likewise, the CsI gas deposition on walls from physical adsorption was also driven by the increase in adsorption velocity at high temperatures [16]. Moreover, the difference in fractions of CsI gas release into the environment among the three units in Table 5 showed that the amount of adsorption was dependent on the starting time of the leakage described in Section 3.1. Figure 13 shows the percentages of accumulative CsI gas deposition due to adsorption in Units 1–3 estimated by Modified ART Mod 2. It was found that adsorption could rapidly increase in the RPVs at high temperatures before the leakage into the environment started when the ambient temperature significantly
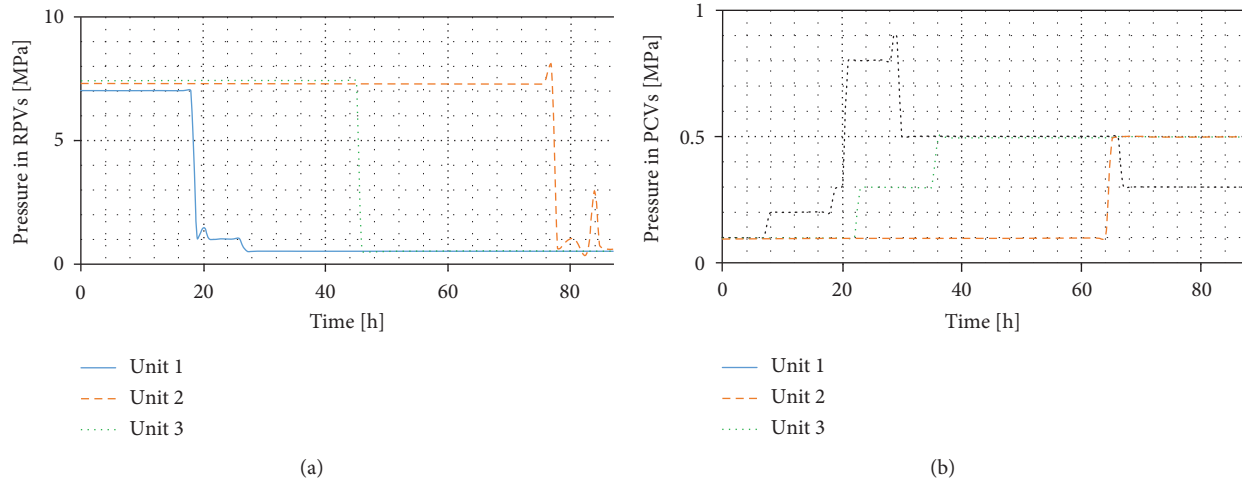
(a)



(b)

FIGURE 4: Conditions of the pressures in Units 1–3 for Modified ART Mod 2 code: (a) the RPVs and (b) the PCVs.
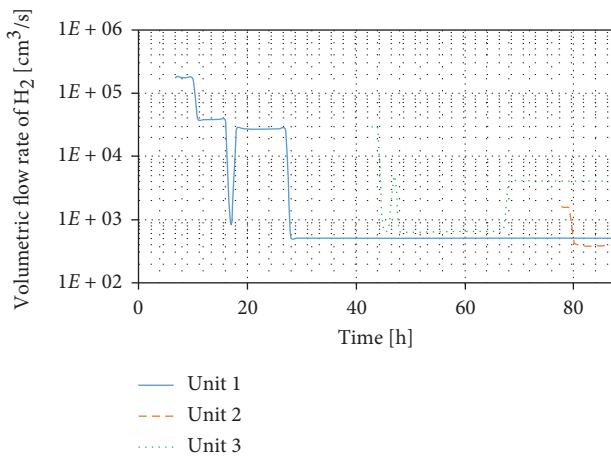


FIGURE 5: Conditions of the volumetric flow rates of $H_2$ gas from the RPVs of Units 1–3 for Modified ART Mod 2 code.

decreased. Thus, the amount of adsorption within the RPVs in Table 5 varied significantly.

## 4.2. Case 2: Independent Failures of RPVs and SFPs.

Figure 14 shows the comparison of the total accumulative release of cesium compounds into the environment from Units 1–3 estimated by Modified ART Mod 2 of the second case and the first case. It was found that the total cesium compound releases at 87 hours were $2.98E + 15$ Bq. When compared to the first case, it was found that the cesium compound releases of the second case were more than the first case by 14 times. This is because the total initial cesium-137 of Units 1–3 in the SFPs was larger than the RPVs and the release from SFPs could directly go to the RBs and the environment without the protection of the PCVs.

Next, contributions of different deposition phenomena to the deposition of CsI gas and CsOH aerosols in the SFP and the RB of Units 1 and 3 and the release into the environment were summarized in Tables 7 and 8. The values for the remaining volumes were identical to Tables 5 and 6. It

was found that although the fractions of release from the SFPs into the environment were smaller than those from the RPVs, the SFPs gave larger release into the environment simply due to larger initial sources. In addition, the SFPs were not protected by the PCVs. Same deposition phenomena as the reference case could be observed, but there were significant differences in contributions of adsorption, thermophoresis, and gravitational settling. Adsorption and thermophoresis within the SFPs were by far less than the RPVs. Although the temperatures in the SFPs were high, the surroundings were different from the RPVs. The SFPs were always open and closer to the environment which made the surrounding temperature much lower than that of the RPVs [43]. Lower temperature decreases adsorption [16] and thermophoresis [40, 41] in the SFPs. Gravitational settling also occurred on the floor of SFPs which was not assumed to exist in RPVs. It became the dominant phenomenon for aerosol deposition in the SFPs.

There is one additional finding from Case 2 which could contribute to the planning of decommissioning. The results showed that the majority of the deposition in RPVs was on walls, while most of the deposition was on the floor in SFPs. Therefore, in the decommissioning after the accident, these highly contaminated areas should be cleaned or eliminated before other parts to help reduce the spread of contamination and radiation effect to workers in the field [44].

## 4.3. Case 3: Simultaneous Failure of RPVs and SFPs.

Figure 15 shows the total accumulative release of cesium compounds into the environment from Units 1–3 using Modified ART Mod 2 code of the third case comparing to the second case. It was found that the total of cesium compound releases at 87 hours was $2.22E + 15$ Bq which was less than the second case by around 25 percent. From Figure 16 which shows the comparison of the ratios of deposition on the wall to deposition on the floor within Units 1–3 of the second case and the third case, it was found that the deposition characteristics of the two cases are similar. Hence, the reason for the difference in the
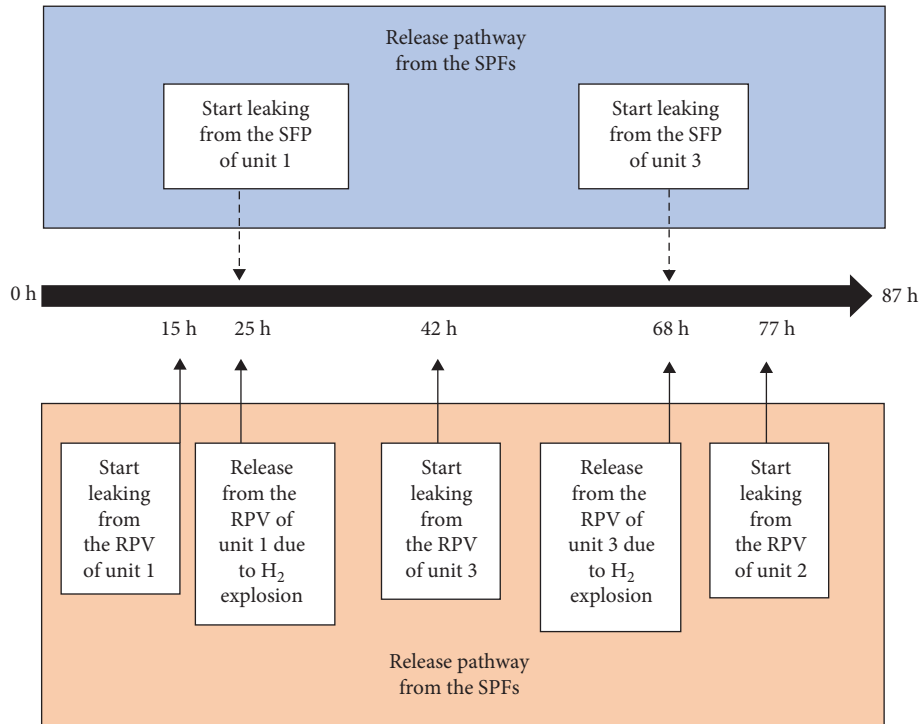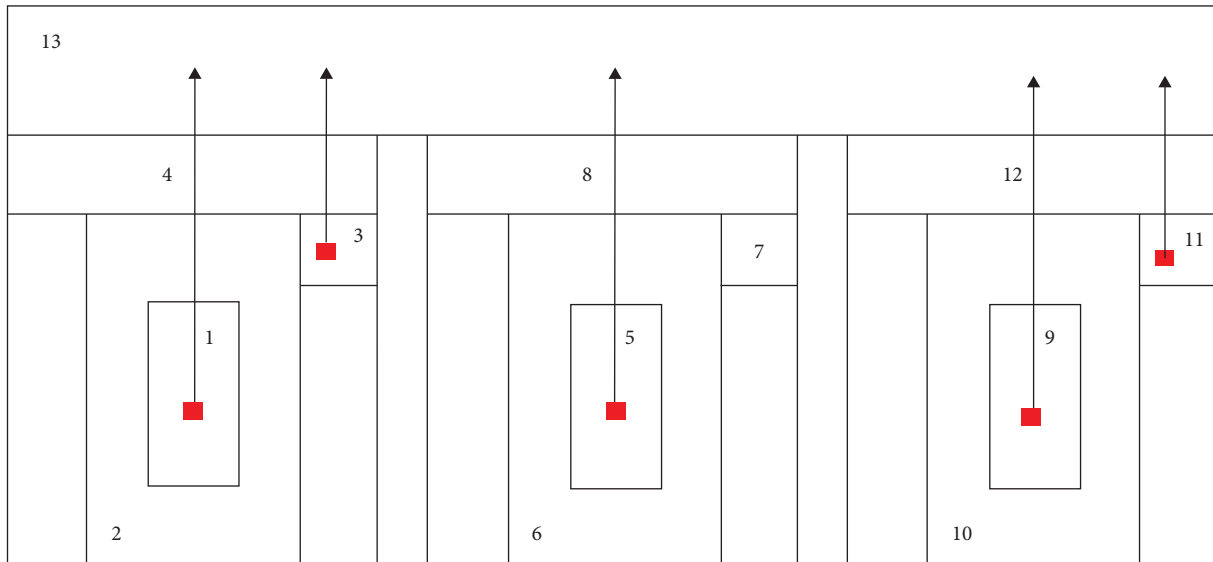
FIGURE 6: Timeline and release pathways of case 2.



Volume 13 is the environment.

Volume 1 is the RPV of the Unit 1.
Volume 2 is the PCV of the Unit 1.
Volume 3 is the SFP of the Unit 1.
Volume 4 is the RB of the Unit 1.

Volume 5 is the RPV of the Unit 2.
Volume 6 is the PCV of the Unit 2.
Volume 7 is the SFP of the Unit 2.
Volume 8 is the RB of the Unit 2.

Volume 9 is the RPV of the Unit 3.
Volume 10 is the PCV of the Unit 3.
Volume 11 is the SFP of the Unit 3.
Volume 12 is the RB of the Unit 3.

■ is the source.

FIGURE 7: Nodalization and flow directions of case 2.

release into the environment could not be described by the deposition characteristics. The simple explanation could be that the transportation of the cesium compounds between the RPVs and the SFPs increased the total flow of cesium compounds among the volumes in the system. Hence, the cesium compounds had more chance to deposit in on the PCV walls due to gas adsorption.

TABLE 4: Cesium source term in the SFPs used for calculation in Modified ART Mod 2.

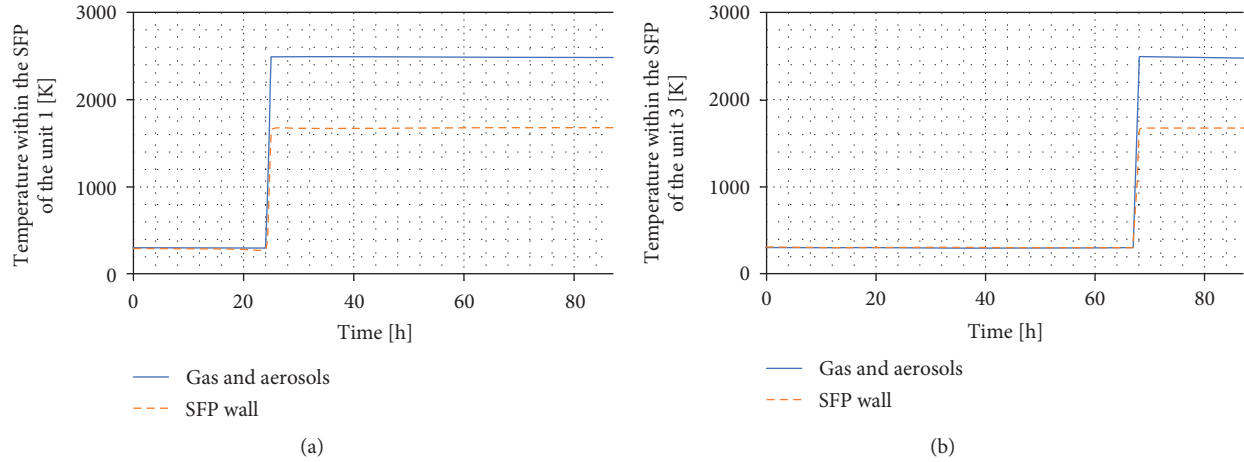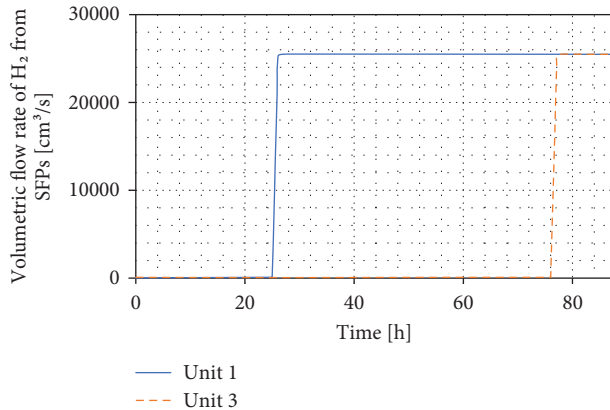| Initial source | Unit | Volume no. | CsI gas (Bq) | CsOH aerosols (Bq) |
| --- | --- | --- | --- | --- |
| SFP | 1 | 1 | $1.64E + 15$ | $2.87E + 14$ |
| SFP | 3 | 9 | $3.92E + 15$ | $6.86E + 14$ |



(a)



(b)

FIGURE 8: Temperatures of the gas and aerosols of cesium compounds and the SFP walls used for calculation in Modified ART Mod 2. (a) Unit 1. (b) Unit 3.



FIGURE 9: Volumetric flow rates of $H_2$ gas from the SFPs used for calculation in Modified ART Mod 2.

This study showcased the integrated release from RPVs and SFPs in a multiunit accident with the most probable conditions. The release of cesium compounds from the SFPs still was the major contribution and was larger than the release from the RPVs by approximately one order of magnitude. These results were not surprising considering the designs of the two components. The RPVs of 1FNPP were located at the center of units and equipped with safety systems such as suppression pools directly connected to the RPVs to retain the fission product, while these safety features are not designed for the SFPs [8]. Although the amount of radioactive materials being released into the environment indicated that SFP failure would lead to larger effects to people and the environment when compared to RPV failure, the occurrence probability of SFP failure is smaller than that of the RPVs by several orders due to lower normal temperature and pressure during reactor operation [8, 10]. However, considering the size of the consequences when the event occurs, the conclusion that the SFP failure during an NPP severe accident requires attention remains true.

Finally, this study showed that Modified ART Mod 2 could evaluate the behavior of cesium compounds in gas and aerosol forms and the amount and timing of their releases into the environment during a multiunit accident with different conditions. Modified ART Mod 2 could contribute to the prediction of consequences of a hypothetical simultaneous failure in the RPVs and the SFPs. Finding from the three cases of the study helped indicate the weakness of the entire system of an NPP with multiple units and the limitation of the coverage of current safety systems which do not normally include the assurance of the safety of SFPs. As mentioned in the introduction section, an NPP accident can affect regions with no active NPPs which implies that ASEAN NPSR has to also put more effort into studying the SFP failure, especially when it occurs at the same time as the RPV failure. Although the magnitude of the earthquake can now be detected in a real-time manner [45], it is still far from the exact prediction [46]. We could never be certain that accidents like or severer than the one that happened at 1FNPP in 2011 will not happen again. Therefore, a holistic study of an NPP severe accident considering the releases from the RPVs and the SFPs should be conducted by ASEAN NPSR in order to help develop the regional strategy on EPR toward future NPP accidents. The EPR should be planned to cover failures in different locations within the reactor unit and also simultaneous accidents in multiple units.

Volume 13 is the environment.
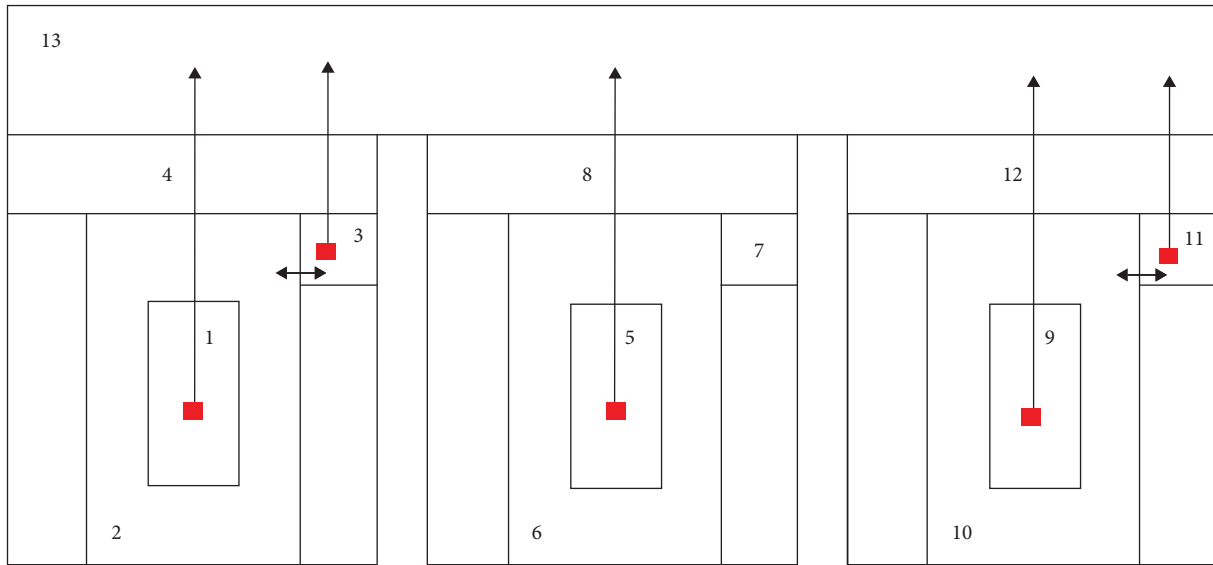


Volume 1 is the RPV of the Unit 1.
Volume 2 is the PCV of the Unit 1.
Volume 3 is the SFP of the Unit 1.
Volume 4 is the RB of the Unit 1.

Volume 5 is the RPV of the Unit 2.
Volume 6 is the PCV of the Unit 2.
Volume 7 is the SFP of the Unit 2.
Volume 8 is the RB of the Unit 2.

Volume 9 is the RPV of the Unit 3.
Volume 10 is the PCV of the Unit 3.
Volume 11 is the SFP of the Unit 3.
Volume 12 is the RB of the Unit 3.

■ is the source.
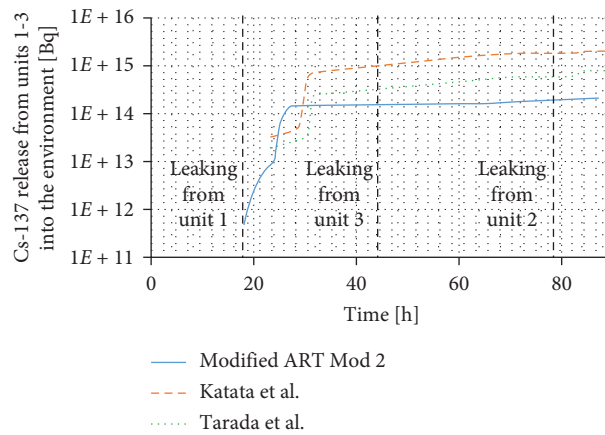
FIGURE 10: Nodalization and flow directions of case 3.



—— Modified ART Mod 2
- - - Katata et al.
······ Tarada et al.

FIGURE 11: Total accumulative release of Cs-137 into the environment from Units 1–3 of the first case.
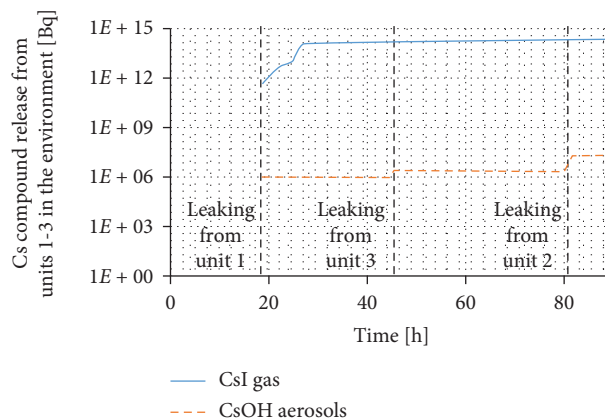


—— CsI gas
- - - CsOH aerosols

FIGURE 12: Total accumulative release of CsI gas and CsOH aerosols from Units 1–3 of the first case simulated by Modified ART Mod 2.

TABLE 5: Deposition phenomena of CsI gas in Units 1–3 of the first case simulated by Modified ART Mod 2.

| Unit | Type | Volume no. | CsI gas deposition (% of initial CsI gas from the RPVs of each unit) | | |
| | | | Adsorption | Remaining | Total release into the environment of each unit |
|---|---|---|---|---|---|
| 1 | RPV | 1 | $1.30E+01$ | $1.77E-01$ | |
| | PCV | 2 | $2.55E-03$ | $6.32E+01$ | $8.61E+00$ |
| | RB | 4 | $1.80E-04$ | $1.50E+01$ | |
| 2 | RPV | 5 | $8.47E+01$ | $1.35E+01$ | |
| | PCV | 6 | $3.45E-02$ | $1.81E+00$ | $5.44E-06$ |
| | RB | 8 | $1.02E-05$ | 5.08E-03 | |
| 3 | RPV | 9 | $6.30E+01$ | $5.97E+00$ | |
| | PCV | 10 | $6.88E-02$ | $2.18E+01$ | $7.97E+00$ |
| | RB | 12 | $3.39E-06$ | $1.19E+00$ | |

TABLE 6: Deposition phenomena of CsOH aerosols in Units 1–3 of the first case simulated by Modified ART Mod 2.

| Unit | Type | Volume no. | CsOH aerosols deposition ([% of initial CsOH aerosols from the RPVs of each unit) | | | |
| | | | GS[a] | BD[b] | TP[c] | Total release into the environment of each unit |
|---|---|---|---|---|---|---|
| 1 | RPV | 1 | $0.00E+00$ | $5.77E-01$ | $9.72E+01$ | |
| | PCV | 2 | $8.61E-04$ | $1.30E-02$ | $2.11E+00$ | $2.63E-07$ |
| | RB | 4 | $1.59E-04$ | $8.59E-04$ | 1.31E-01 | |
| 2 | RPV | 5 | $0.00E+00$ | $7.97E-01$ | $9.56E+01$ | |
| | PCV | 6 | $3.44E-01$ | $5.50E-03$ | $3.28E+00$ | $3.76E-06$ |
| | RB | 8 | $6.95E-04$ | $9.57E-06$ | $7.30E-04$ | |
| 3 | RPV | 9 | $0.00E+00$ | $4.92E-01$ | $8.97E+01$ | |
| | PCV | 10 | $2.17E-02$ | $1.46E-02$ | $9.71E+00$ | $4.22E-06$ |
| | RB | 12 | $1.95E-04$ | $5.92E-04$ | $8.50E-02$ | |

[a]Gravitational settling on floor. [b]Brownian diffusion on wall. [c]Thermophoresis on wall.
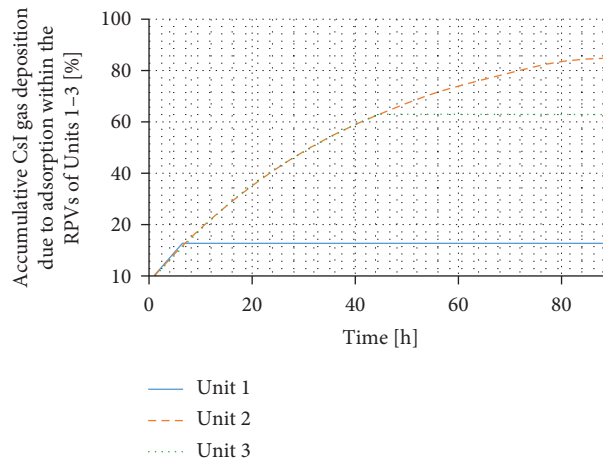


FIGURE 13: Percentages of accumulative CsI gas deposition due to adsorption within the RPVs of Units 1–3 using Modified ART Mod 2 code of the first case.

On the other hand, this work indicated the importance of possibly new NPP technologies especially Small Modular Reactors (SMRs) which are the potential to reduce risk of the SFP accidents [47]. SMRs' technologies were considered as the one of main points in ASEAN NPSR to contribute to new nuclear safety research which concerns about new consequences' forms of SMRs. This new nuclear safety research helped support the strength of the EPR in ASEAN through the collaborative work of ASEAN NPSR in the future.
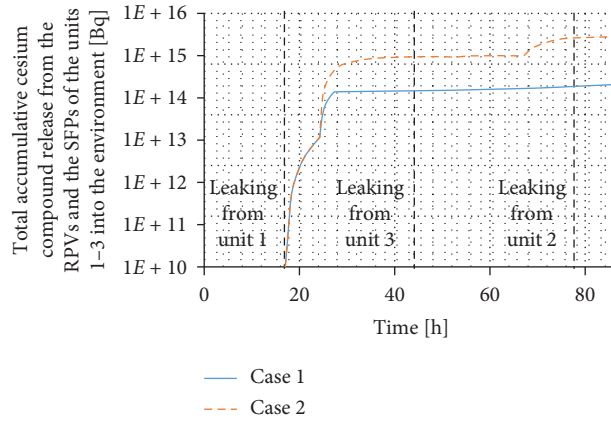
FIGURE 14: Total accumulative release of cesium compounds into the environment from Units 1–3 estimated by Modified ART Mod 2 of case 2 comparing to the reference case.

TABLE 7: Deposition phenomena of CsI gas in the SFP and the RB of Units 1 and 3 of the second case simulated by Modified ART Mod 2.

| Unit | Type | Volume no. | CsI gas deposition (% of initial CsI gas from the SFPs of each unit) | | |
| | | | Adsorption | Remaining | Total release into the environment of each unit |
| --- | --- | --- | --- | --- | --- |
| 1 | SFP | 3 | $1.24E-03$ | $1.82E-03$ | $5.12E+01$ |
| | RB | 4 | $5.37E-04$ | $4.88E+01$ | |
| 3 | SFP | 11 | $1.56E-03$ | $3.13E+00$ | $4.96E+01$ |
| | RB | 12 | $1.17E-04$ | $4.72E+01$ | |

TABLE 8: Deposition phenomena of CsOH aerosols in the SFP and the RB of Units 1 and 3 of the second case simulated by Modified ART Mod 2.

| Unit | Type | Volume no. | CsOH aerosols deposition (% of initial CsOH aerosols from the SFPs of each unit) | | | |
| | | | $GS^{(a)}$ | $BD^{(b)}$ | $TP^{(c)}$ | Total release into the environment of each unit |
| --- | --- | --- | --- | --- | --- | --- |
| 1 | SFP | 3 | $9.93EE+01$ | $6.73E-01$ | $1.09E-07$ | $2.86E-10$ |
| | RB | 4 | $6.07E-11$ | $3.28E-10$ | $5.00E-08$ | |
| 3 | SFP | 11 | $9.93E+01$ | $6.73E-01$ | $1.29E-26$ | $3.35E-29$ |
| | RB | 12 | $8.33E-30$ | $3.72E-29$ | $5.66E-27$ | |

$^{(a)}$Gravitational settling on the floor. $^{(b)}$Brownian diffusion on the wall. $^{(c)}$Thermophoresis on the wall.
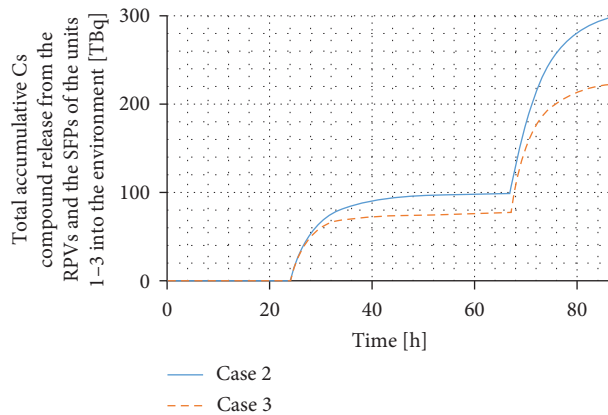


FIGURE 15: Total accumulative release of cesium compounds into the environment from Units 1–3 using Modified ART Mod 2 of case 3 comparing to case 2.
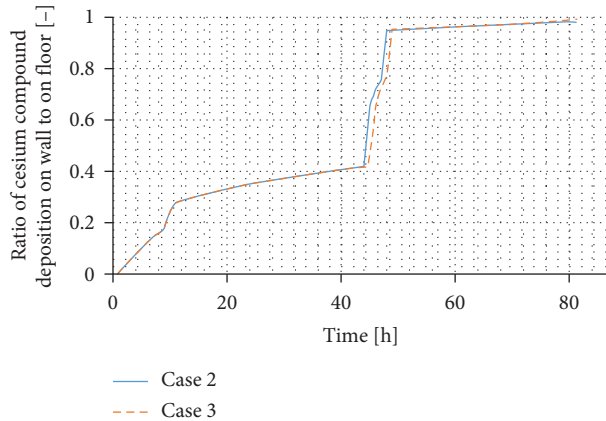
FIGURE 16: Comparison of the ratios of deposition on the wall to deposition on the floor within Units 1–3 of case 2 and case 3.

## 5. Conclusions

This paper assessed the fission product behavior of the cesium compounds in gas and aerosol forms during a simultaneous failure of RPVs and SFPs of BWR type with Mark I containment design in multiple units using Modified ART Mod 2 to demonstrate the ability of Modified ART Mod 2 to provide the source term data of a radioactive release from an NPP to the environment for the transboundary atmospheric dispersion assessment under ASEAN NPSR through the three case studies.

In the first case, Modified ART Mod 2 was used to simulate the cesium compound releases from the RPVs based on the past accident at 1FNPP. The behavior of the cesium compounds basically depended on the effect of high temperature which impacted adsorption and thermophoresis of the compounds. The second case considered independent releases from the SFPs and the RPVs to evaluate the maximum release in the environment. It was found that the release of cesium compounds of the second case was more than the first case by 14 times. This was simply due to larger initial sources and the inexistence of a multilayered protection system for SFPs. The third case considered the radioactive material flow between the SFPs and the RPVs. It was found that the release into the environment decreased by 25% since the increase in the total flow in PCVs heightens the chance for the cesium compounds to deposit on the PCV walls due to gas adsorption.

This study helped understand the physical characteristics of a simultaneous failure of RPVs and SFPs, which could support NPP safety assurance and safe decommissioning. From the viewpoint of ASEAN NPSR, the study enabled an evaluation of different types of radioactive releases from an NPP, including a combined release from different sources. This ability when combined with the ability to assess transboundary atmospheric dispersion [48] will support the development of the ASEAN EPR guidelines which will be useful for the planning of regional response during an accident in an external NPP. Moreover, this work indicated the importance of new NPP technologies to avoid the SFP accidents in ASEAN such as SMRs which were considered the

future nuclear safety research to help support the of the EPR in ASEAN in the future.

## Data Availability

All research papers and documents are cited at relevant places within the text as references.

## Conflicts of Interest

The authors declare that they have no conflicts of interest.

## References

[1] K.-M. Wai and P. K. N. Yu, "Trans-oceanic transport of 137 Cs from the Fukushima nuclear accident and impact of hypothetical Fukushima-like events of future nuclear plants in Southern China," *Science of The Total Environment*, vol. 508, pp. 128–135, 2015.

[2] ASEAN Network on Nuclear Power Safety Research, *Joint Communique on the Establishment of ASEAN Network on Nuclear Power Safety Research*, ASEAN Network on Nuclear Power Safety Research, Bangkok, Thailand, 2017.

[3] R. Chang, J. Schaperow, T. Ghosh et al., "State-of-the-art reactor consequence analyses (SOARCA) report," U.S. Nuclear Regulatory Commission, Washington, D.C., USA, NUREG-1935, 2012.

[4] K. Oh, S.-y. Kim, H. Jeon, and J. S. Park, "Study on multi-unit level 3 PSA to understand a characteristics of risk in a multi-unit context," *Nuclear Engineering and Technology*, vol. 52, no. 5, pp. 975–983, 2020.

[5] J.-E. Yang, "Fukushima dai-ichi accident: lessons learned and future actions from the risk perspectives," *Nuclear Engineering and Technology*, vol. 46, no. 1, pp. 27–38, 2014.

[6] Power Technology, *Fangchenggang Nuclear Power Plant*, Power Technology, Guangxi, China, 2020, https://www.power-technology.com/projects/fangchenggang-nuclear-power-plant-guangxi/.

[7] Tokyo Electric Power Company, "Evaluation of the situation of cores and containment vessels of Fukushima Daiichi Nuclear Power Station Units 1 to 3 and examination into unsolved issues in the accident progression," Progress report no. 5, Tokyo Electric Power Company, Tokyo, Japan, 2017.

[8] International Atomic Energy Agency, *The Fukushima Daiichi Accident Technical*, International Atomic Energy Agency, Vienna, Austria, 2015.

[9] Fauske & Associates, *User's Manual of MAAP 5, Modular Accident Analysis Program*, Fauske & Associates, Burr Ridge, IL, USA, 2008.

[10] A. G. Croff, *A User's Manual for the ORIGEN2 Computer Code*, Oak Ridge National Laboratory, Oak Ridge, TN, USA, 1980.

[11] D. Wang, I. C. Gauld, G. L. Yoder et al., "Study of Fukushima Daiichi nuclear power station unit 4 spent-fuel pool," *Nuclear Technology*, vol. 180, no. 2, pp. 205–215, 2012.

[12] Fauske & Associates, *Transmittal Document for MAAP 5 Code Revision MAAP 5.02*, Fauske & Associates, Burr Ridge, IL, USA, 2013.

[13] J. C. R. Blul, P. McMinn, and A. Grah, "Analysis of the inherent response of nuclear spent fuel pools," *Annals of Nuclear Energy*, vol. 124, pp. 295–326, 2019.

[14] D. Mercurio, V. M. Andersen, and K. C. Wagner, "Integrated level 1-level 2 decommissioning probabilistic risk assessment

for boiling water reactors," *Nuclear Engineering and Technology*, vol. 50, no. 5, pp. 627–638, 2018.

[15] I. S. Kim, M. Jang, and S. R. Kim, "Holistic approach to multi-unit site risk assessment: status and issues," *Nuclear Engineering and Technology*, vol. 49, no. 2, pp. 286–294, 2017.

[16] M. Kajimoto, A. Hidaka, K. Muramatsu, and J. Sugimoto, *A Computer Code for the Analysis of Radionuclide Transport and Deposition under Severe Accident Conditions*, Japan Atomic Energy Agency, Ibaraki, Japan, 1988.

[17] W. Vechgama, K. Silva, and S. Rassame, "Validation of Modified ART Mod 2 code through comparison with aerosol deposition of cesium compound in Phébus FPT3 containment vessel," *Science and Technology of Nuclear Installations*, vol. 2019, Article ID 4081943, , 2019.

[18] W. Vechgama, K. Silva, C. Kittasin, and S. Rassame, "Application of Modified ART Mod 2 code to fission product behavior analysis for spent fuel pool of nuclear power plant," in *Proceedings of the Technical Meeting on the Phenomenology, Simulation and Modelling of Accidents in Spent Fuel Pools*, Vienna, Austria, September 2019.

[19] W. Vechgama and K. Silva, "Integration of fission product release analysis from reactor pressure vessel and spent fuel pool in Modified ART Mod 2," in *Proceedings of the International Youth Nuclear Congress*, Sydney, Australia, November 2020.

[20] International Commission on Radiological Protection, "Occupational intakes of radionuclides: Part 3, ICRP Publication 137," International Commission on Radiological Protection, Ontario, Canada, Annals of the ICRP 46(3/4), 2007.

[21] L. E. Herranz, *"Fission Product Behavior and Transport," Joint ICTP-IAEA 1st Course on Scientific Novelties in Phenomenology of Severe Accidents in Water Cooled Reactors (WCRs)*, International Centre for Theoretical Physics, Trieste, Italy, 2018.

[22] K. Moriyama, Y. Maruyama, H. Nakamura, and H. Nakamura, "Kiche: a simulation tool for kinetics of iodine chemistry in the containment of light water reactors under severe accident conditions," Report number: JAEA-Data/Code 2010-034, Japan Atomic Energy Agency, Ibaraki, Japan, 2011.

[23] Q. Liu, J. Ishikawa, Y. Maruyama, and N. Watanabe, "A simple method for estimating the structure temperatures and the cesium revaporization inside the reactor pressure vessel - I: basic concepts and model descriptions for the Fukushima Daiichi Nuclear Power Plant," *Journal of Nuclear Science and Technology*, vol. 49, no. 5, pp. 479–485, 2012.

[24] Tokyo Electric Power Company, *Fukushima Nuclear Accident Analysis Report*, Tokyo Electric Power Company, Tokyo, Japan, 2012.

[25] Tokyo Electric Power Company, *Detailed Analysis of the Accident Progression of Units 1 to 3 by Using MAAP Code*, Tokyo Electric Power Company, Tokyo, Japan, 2012.

[26] International Research Institute for Nuclear Decommissioning, "Basic data of Fukushima Daiichi nuclear power plant," 2013, https://irid.or.jp/fd/page_id/237/.

[27] J. Rempe, M. Corradini, M. Farmer et al., "Safety insights from forensics evaluations at Daiichi," *Nuclear Materials and Energy*, vol. 10, pp. 8–34, 2017.

[28] P. Povinec, K. Hirose, and M. Aoyama, *Fukushima Accident: Radioactivity Impact on the Environment*, Elsevier, Amsterdam, Netherlands, 2013.

[29] Tokyo Electric Power Company, *Reactor Core Conditions of Units 1 to 3 of Fukushima Daiichi Nuclear Power Station*, Tokyo Electric Power Company, Tokyo, Japan, 2011.

[30] T. Haste, F. Payot, C. Manenc et al., "Phébus FPT3: overview of main results concerning the behaviour of fission products and structural materials in the containment," *Nuclear Engineering and Design*, vol. 261, pp. 333–345, 2013.

[31] L. Fernandez-Moguel, A. Rýdl, T. Lind, and B. Jäckel, *The OECD-NEA Benchmark Study of the Accident at the Fukushima Daiichi Nuclear Power Station (BSAF) Project-Phase 2*, Paul Scherrer Institute, Villigen, Switzerland, 2017.

[32] National Academies of Sciences, Engineering, and Medicine, *Lessons Learned from the Fukushima Nuclear Accident for Improving Safety and Security of U. S. Nuclear Plants: Phase 2*, National Academies Press, Washington, D.C., USA, 2016.

[33] H. Terada, G. Katata, M. Chino, and H. Nagai, "Atmospheric discharge and dispersion of radionuclides during the Fukushima Dai-ichi Nuclear power plant accident. part II: verification of the source term and analysis of regional-scale atmospheric dispersion," *Journal of Environmental Radioactivity*, vol. 112, pp. 141–154, 2012.

[34] G. Katata, M. Chino, T. Kobayashi et al., "Detailed source term estimation of the atmospheric release for the Fukushima Daiichi Nuclear power station accident by coupling simulations of an atmospheric dispersion model with an improved deposition scheme and oceanic dispersion mode," *Atmospheric Chemistry and Physics*, vol. 15, 2015.

[35] R. J. M. Konings, T. Wiss, and O. Beneš, "Predicting material release during a nuclear reactor accident," *Nature Materials*, vol. 14, no. 3, pp. 247–252, 2015.

[36] F. Z. Roki, M. N. Ohnet, and B. Simondi-Teisseire, "Thermodynamic and kinetic studies of iodine and caesium transport in nuclear severe accident by high temperature mass spectrometer," in *Proceedings of the Nuclear Energy for New Europe*, Portoroz, Slovenia, September 2008.

[37] Y. Chen, H. Zhang, W. Villanueva, W. Ma, and S. Bechta, "A sensitivity study of MELCOR nodalization for simulation of in-vessel severe accident progression in a boiling water reactor," *Nuclear Engineering and Design*, vol. 343, pp. 22–37, 2019.

[38] Tokyo Electric Power Company, *Fukushima Daiichi Genshiryoku Hatsudensho 1~3-goki No Roshin Jotai Ni Tsuite: On the Status of the Reactor Core in Fukushima Daiichi Nuclear Power Plant Units 1~3*, Tokyo Electric Power Company, Tokyo, Japan, 2011.

[39] H. Albrecht, V. Matschofl, and H. Wild, "Release of fission and activation products during LWR core meltdown," International Atomic Energy Agency, Vienna, Austria, INIS-MT-49658, 1978.

[40] L. Talbot, R. K. Cheng, R. W. Schefer, and D. R. Willis, "Thermophoresis of particles in a heated boundary layer," *Journal of Fluid Mechanics*, vol. 101, no. 4, pp. 737–758, 1980.

[41] S. Tseng, Y.-R. Hsu, and J.-P. Hsu, "Diffusiophoresis of polyelectrolytes: effects of temperature, pH, type of ionic species and bulk concentration," *Journal of Colloid and Interface Science*, vol. 459, pp. 167–174, 2015.

[42] F. Nieuwstadt, "The computation of the friction velocity u ∗ and the temperature scale T ∗ from temperature and wind velocity profiles by least-square methods," *Boundary-Layer Meteorology*, vol. 14, no. 2, pp. 235–246, 1978.

[43] A. Barto, Y. J. Chang, K. Compton et al., "Consequence study of a beyond-design-basis earthquake affecting the spent fuel pool for a U.S. Mark I boiling water reactor," U.S. Nuclear Regulatory Commission, Washington, D.C., USA, NUREG-2161, 2014.

[44] International Atomic Energy Agency, "Decommissioning of nuclear power plants, research reactors and other nuclear fuel

cycle facilities," International Atomic Energy Agency, Vienna, Austria, Specific safety guide No. SSG-47, 2018.

[45] K. Tamaribuchi, "Evaluation of automatic hypocenter determination in the JMA unified catalog," *Earth, Planets and Space*, vol. 70, no. 141, 2018.

[46] R. J. Geller, D. D. Jackson, Y. Y. Kagan, and F. Mulargia, "Earthquakes cannot be predicted," *Science*, vol. 275, no. 5306, p. 1616, 1997.

[47] R. J. Budnitz, H.-H. Rogner, and A. Shihab-Eldin, "Expansion of nuclear power technology to new countries - SMRs, safety culture issues, and the need for an improved international safety regime," *Energy Policy*, vol. 119, pp. 535–544, 2018.

[48] K. Silva, P. Krisanungkura, N. Khunsrimek, and S. Rassame, "Enhancing radiation monitoring system in preparation for transboundary atmospheric dispersion from a nuclear power plant accident," in *Proceedings of the Asian Symposium on Risk Assessment and Management*, Gyeongju, South Korea, October 2019.

*Research Article*

# Shielding Design and Dose Evaluation for HTR-PM Fuel Transport Pipelines by QAD-CGA Program

**Sheng Fang** ⬤,[1] **Jianzhu Cao**,[1] **Wenqian Li** ⬤,[1] **Chen Luo**,[2] **Feng Yao**,[1] **Xiaofan Li**,[3] **and Kai Li**[3]

[1]*Institute of Nuclear and New Energy Technology, Collaborative Innovation Centre of Advanced Nuclear Energy Technology, Key Laboratory of Advanced Reactor Engineering and Safety, Ministry of Education, Tsinghua University, Beijing, China*
[2]*Beijing Institute of Metrology, Beijing, China*
[3]*CNNC Everclean Environmental Engineering Co., Ltd, Beijing 100037, China*

Correspondence should be addressed to Wenqian Li; mili@mail.tsinghua.edu.cn

The spherical fuel elements are adopted in the high-temperature gas-cooled reactor pebble-module (HTR-PM). The fuel elements will be discharged continuously from the reactor core and transported into the fuel transport pipelines during the reactor operation, leading to spatially varying dose outside the pipeline. In this case, the dose evaluation faces two major challenges, including dynamic source terms and pipelines with varying lengths and shapes. This study tries to handle these challenges for HTR-PM through comprehensive calculations using the QAD-CGA program and to design the corresponding shielding of the pipeline. During the calculation, it is assumed that a spherical fuel element stays in different positions of the pipelines in turn, and the corresponding dose contributions were calculated. By integrating the dose contributions at different positions, the dose at the points of interest can be obtained. The total dose is further determined according to the assumed fuel elements transport speed of 5 m/s and total 6000 fuel elements transportation per day. Two types of fuel transport pipelines and two source terms were considered, i.e., the spent fuel element transport pipelines with corresponding spent fuel source term and the different burn-up fuel element transport pipelines with the average burn-up fuel source term. Doses at different points of interest were calculated with no shielding scenario and with lead shielding of different thicknesses scenario. To evaluate the shielding effect, the dose limit of the orange radiation zone of HTR-PM and the radiation damage thresholds from NCRP report No.51 were both adopted. The calculated results show that, for pipelines that transport the spent fuel, a 4 cm lead shielding will be enough. And for pipelines that transport fuel elements with different burn-up, a 5 cm lead shielding will be added. The method and results can provide valuable reference for other work of HTR-PM.

## 1. Introduction

The high-temperature gas-cooled reactor pebble-module (HTR-PM) is undergoing commissioning in Shandong Province of China. It has many characteristics different from the traditional pressurized water reactors [1–5]. The spherical graphite coated components are adopted in HTR-PM reactor as fuel elements. Each spherical fuel element is 60 mm in diameter and coating about 8000 $UO_2$ kernels in it. During the operation of the reactor, the spherical fuel elements will be removed and reloaded into the core periodically through the fuel transport pipelines [6]. Without enough shielding, the dose rate outside the pipelines will be

too high, since the irradiated spherical fuel elements are severely activated. For practical engineering design, two types of pipelines are worth attention. One is for the spent fuel elements transport, and the other is for the transport of fuel elements with different burn-up. The transport of both spherical fuel elements involves dynamic source terms. In addition, the length of the pipelines varies from place to place, leading to different dose in each case.

For the shielding calculation, the Monte Carlo simulation method and the empirical formula approximation calculation method are commonly employed. The Monte Carlo method can deal with complex geometric structures, material composition, and source terms, by simulating the real particle

transport process, such as scattering, transmission, and absorption. Widely used software based on the Monte Carlo method includes MCNP [7–9], FLUKA (http://www.fluka.org/fluka.php; [10], GEANT4 [11, 12], and so on. However, the Monte Carlo method usually requires a longer calculation time. The QAD-CGA program, which is based on the point-kernel integration technique, is especially suitable for dealing with shielding design problems under simple geometric structures. The scattering of particles is approximated by the buildup factor [13, 14]. After comparison and verification, under the simple geometric model, the QAD-GCA program has the advantages of fast calculation speed and accurate results [15–19]. The dose evaluation along the pipelines involves only a simple geometry, but requires repetitive calculation with varying source terms. These features make the QAD-CGA program a good candidate for the dose calculation.

For the above reason, the QAD-CGA is used to calculate the dose caused by a moving fuel element in this study. The dose rates by a fuel element at different positions are calculated at the points of interest. Based on the speed of the fuel element, the total dose at the point of interest is calculated by integrating the dose rates with the duration of the fuel element at each position. This method is applied to the calculation of the point-by-point dose rate for a single spent fuel element, the average hourly dose rate from 6000 elements per day, and the cumulative dose of 40 years from 6000 elements per day for different cases. The results are compared with the dose limit of the orange radiation zone of HTR-PM and the thresholds of radiation tolerance of different materials from NCRP report No. 51.

## 2. Method

*2.1. Source Terms.* The spherical fuel elements will pass through the fuel transport pipelines at an average speed of 5 m/s. Two types of source terms need to be considered: (1) the spent fuel and (2) the average burn-up fuel, which is for the fuel elements transport with different burn-up. Normally, there will be 6000 elements passing through the pipelines per day.

The source term for the average burn-up fuel is calculated under the assumption that the proportion of the fuel elements with different cycle numbers (1–4 \ 5–8 \ 9–12 \ 13–14 \ 15) is, respectively, 1.2/15, 1.1/15, 1.0/15, 0.9/15, and 0.

The KORIGEN code was adopted to calculate the gamma source terms. KORIGEN is a KARLSRUHE version of the ORIGEN code [20] developed by the Oak Ridge National Laboratory, which contains an updated nuclide cross section data library for high-temperature gas-cooled reactors. KORIGEN calculates the radionuclide inventory at the equilibrium of the reactor, by solving deterministic differential equations. It can calculate irradiation in both thermal and fast-neutron spectra [21–24].

From the KORIGEN calculation, there will be more than 60 radionuclides in a spent fuel element [25]. Figure 1 shows the gamma-ray intensity of the two source terms, which were derived from the radionuclide inventory. For the spent fuel
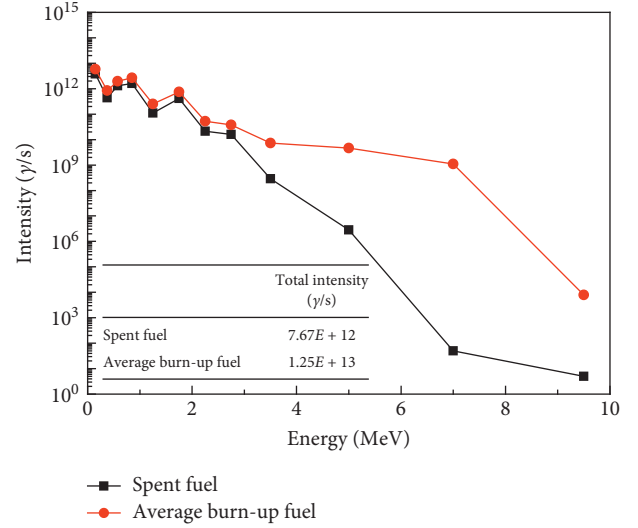


FIGURE 1: The source terms for the spent fuel and the average burn-up fuel.

source term, the total gamma intensity is $7.67 \times 10^{12}$ $\gamma$/s. For the average burn-up fuel source term, the total gamma intensity is $1.25 \times 10^{13}$ $\gamma$/s.

*2.2. Geometry Model.* The outer diameter of the fuel transport pipelines is 69 mm with a thickness of 2 mm as shown in Figure 2. The pipeline is made of stainless steel with density of 7.8 g/cm$^3$. Its main component is iron and also contains impurities, such as carbon, silicon, manganese, nickel, chromium, and titanium. In the calculation, the composition of the pipeline was simplified to iron. The points of interest were all chosen in the middle line of the pipeline. The distance between one point of interest and the outside of the pipeline is defined as Dpi.

For pipelines that transport the spent fuel, two scenarios were considered: with no shielding and with a 4 cm lead shielding. For pipelines that transport fuel elements with different burn-up, three scenarios were considered: with no shielding, with a 4.5 cm lead shielding, and with a 5 cm lead shielding.

When the spherical fuel element moves from the left side to the right side of the pipeline, its dose contribution to the points of interest at different positions of the pipeline may vary greatly. In this work, the following method was adopted to calculate the total dose at one point of interest produced by a spherical fuel element passing through the pipeline one time.

Taking the 5 m-length pipeline as an example, its left half can be divided into 13 segments, as shown in Figure 2, where AB, BC, CD to LM are all 20 cm length (12 segments in total), and the length of the MN is 10 cm.

Define the dose from a spherical fuel element to one point of interest during its movement in the AB segment as $D_{AB}$. $D_{AB}$ can be conservatively calculated by
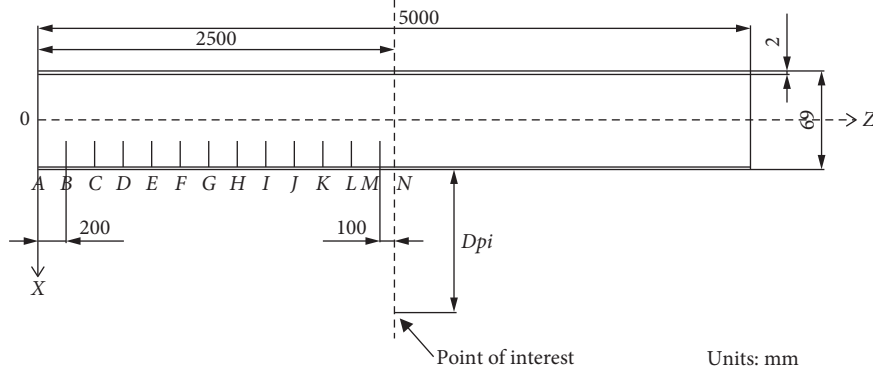
$$D_{AB} = d_B \times t_B, \tag{1}$$

Figure 2: The geometry structure in the QAD-CGA calculation.

where $d_B$ is the dose rate of the spherical fuel element at point B and $t_B$ is the time required for the fuel element to pass through the AB segment.

For the other segments, the calculation method is similar. Since the points of interest are located in the middle of the pipeline, due to the symmetrical relationship, the spherical fuel element gives the same dose to one point of interest when it moves in the left half and right half sections. Then, the dose from a spherical fuel element to the point of interest during its movement along the whole pipeline ($D$) can be calculated by

$$D = 2 \times \sum \left( D_{AB}, D_{BC}, \ldots, D_{LM} \right) + D_{MN}. \qquad (2)$$

*2.3. Dose Limit.* We focus on $\dot{D}$ and $D_{40y}$, which are defined as follows: $\dot{D}$ is the average hourly dose rate from 6000 elements per day, mGy/h, which can be calculated by equation (3); $D_{40y}$ is the cumulative dose of 40 years from 6000 elements per day, Gy, which can be calculated by equation (4).

$$\dot{D} = D \times \left( \frac{6000}{24} \right), \qquad (3)$$

$$D_{40y} = \dot{D} \times 40 \times 365.25 \times \frac{24}{1000}. \qquad (4)$$

For $D_{pi} = 30$ cm, the dose limit of $\dot{D}$ should be 3 mGy/h, which is the upper limit value of the orange radiation zone of HTR-PM.

For $D_{40y}$, it is mainly used to evaluate the material radiation damage. Two concerned radiation damage thresholds are listed in Table 1 (NCRP report No. 51) [25].

## 3. Results and Discussion

*3.1. For Pipelines That Transport the Spent Fuel.* For pipelines that transport the spent fuel, two scenarios were considered: pipelines with no shielding and with a 4 cm lead shielding.

Firstly, for each case, the point-by-point dose rate by one spent fuel element should be calculated. Figure 3 shows one of the point-by-point dose rates calculated results. It is relative to a point of interest of Dpi = 30 cm and for a 5 m pipeline with no shielding case.

Table 1: Two concerned radiation damage thresholds.

| Item | Threshold (Gy) |
|---|---|
| Plastics losing tensile strength | $1 \times 10^4$–$1 \times 10^7$ |
| Natural rubber losing elasticity | $5 \times 10^4$–$3 \times 10^5$ |

From Figure 3, it can be seen, at point B, the dose rate is 239 mGy/h, while at point N the dose rate increases to $2.09 \times 10^4$ mGy/h, which is 2 orders of magnitude higher than point B's dose rate. So, it can be drawn that the dose of points of interest is mainly affected by the segments near the middle of the pipeline.

Then, based on the point-by-point dose rate results, the $\dot{D}$ and $D_{40y}$ results of different Dpi and different pipeline lengths can be calculated by equations (3) and (4).

Figure 4 shows the average hourly dose rate $\dot{D}$ at different Dpi positions for a 5 m pipeline, from which it can be seen, for the pipeline with no shielding case, at $Dpi = 30$ cm's position, $\dot{D} = 318$ mGy/h; and at $Dpi = 500$ cm's position, $\dot{D} = 5.99$ mGy/h, which decreased by two orders of magnitude. For the pipeline with a 4 cm lead shielding case, the $\dot{D}$ at $Dpi = 30$ cm and 500 cm are 2.86 mGy/h and $9.74 \times 10^{-2}$ mGy/h, respectively. It can be drawn that a 4 cm lead shielding can reduce the dose rates at points of interest with the same Dpi by nearly two orders of magnitude.

Figure 5 shows the calculated $D_{40y}$ results at different Dpi positions for a 5 m pipeline, from which it can be seen, for the pipeline with no shielding case, at $Dpi = 30$ cm's position, $D_{40y} = 1.11 \times 10^5$ Gy; and at $Dpi = 500$ cm's position, $D_{40y} = 2.1 \times 10^3$ Gy, which also decreased by two orders of magnitude. For the pipeline with a 4 cm lead shielding, the $D_{40y}$ at $Dpi = 30$ cm and 500 cm are 1000 Gy and 34.2 Gy, respectively. Similarly, as $\dot{D}$, a 4 cm lead shielding can reduce $D_{40y}$ at points of interest with the same $Dpi$ by nearly two orders of magnitude.

Table 2 lists the $\dot{D}$ and $D_{40y}$ values at $Dpi = 30$ cm's position for pipelines of 1–5 m length. The calculation results show that when the pipeline lengths are changed from 1 m to 5 m, the $\dot{D}$ at $Dpi = 30$ cm increases from 227 mGy/h to 318 mGy/h, while with a 4 cm lead shielding, the $\dot{D}$ at $Dpi = 30$ cm increases from 2.72 mGy/h to 2.86 mGy/h when the length of the pipeline changes from 1 m to 3 m. But when the pipeline length increases from 3 m to 5 m, the $\dot{D}$ and $D_{40y}$ will not increase, since the two ends contribute very little
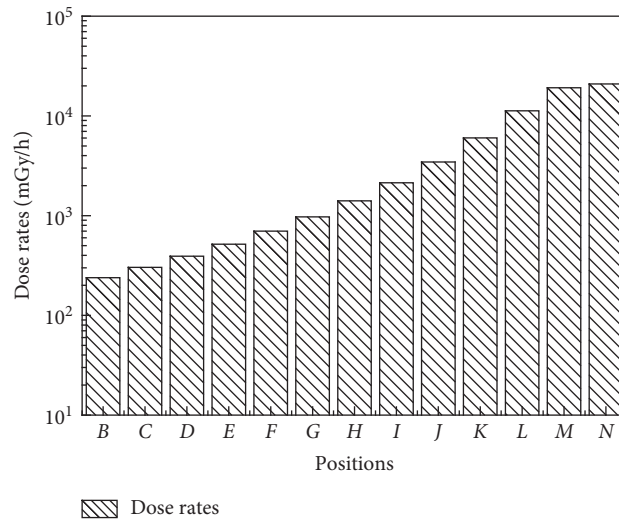
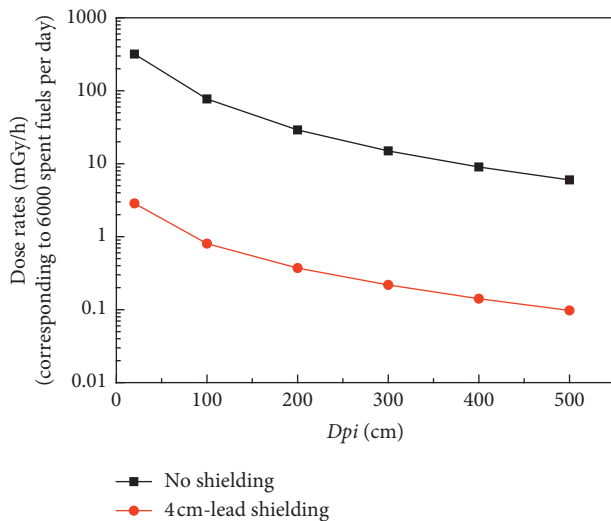FIGURE 3: The dose rates from one spent fuel element ($Dpi = 30$ cm, 5 m pipeline, no shielding).



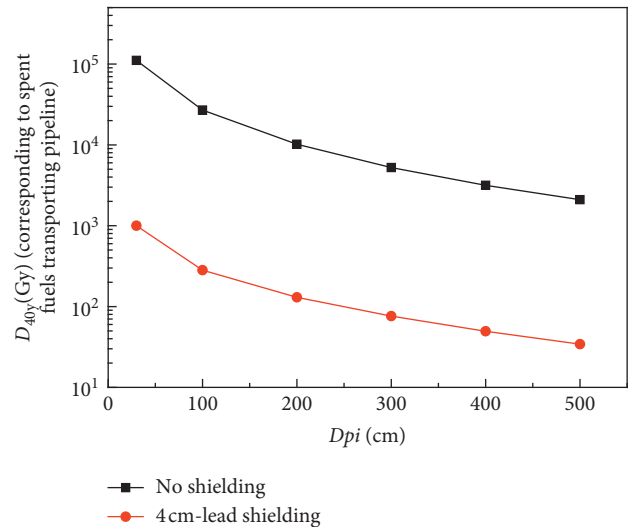FIGURE 4: $\dot{D}$ at different $Dpi$ positions for a 5 m pipeline.



FIGURE 5: $D_{40y}$ at different $Dpi$ positions for a 5 m pipeline.

dose to the point of interest for a long pipeline. Compared with the dose limit of 3 mGy/h, a 4 cm lead shielding should be suitable for pipelines of different lengths.

Also, compared with the radiation damage thresholds list in Table 1, with a 4 cm lead shielding, the highest $D_{40y}$ is 1000 Gy, lower than the plastics losing tensile strength and natural rubber losing elasticity thresholds.

*3.2. For Pipelines That Transport Fuel Elements with Different Burn-Up.* For pipelines that transport fuel elements with different burn-up, the average burn-up fuel source term was adopted. Table 3 lists the calculated results of $\dot{D}$ and $D_{40y}$ for pipelines of 1–5 m lengths at $Dpi = 30$ cm's position. Three scenarios were considered: with no shielding, with a 4.5 cm lead shielding, and with a 5 cm lead shielding.

From Table 3, it can be seen that, for with no shielding case, the $\dot{D}$ increases from 371 mGy/h to 518 mGy/h for 1–5 m pipelines. With a 4.5 cm lead shielding, the $\dot{D}$ can be reduced by 2 orders of magnitude, but still higher than the dose limit of 3 mGy/h. With a 5 cm lead shielding, the $\dot{D}$ can be reduced to lower than 3 mGy/h. Similar to the spent fuel transport case, the phenomenon happened that the $\dot{D}$ and $D_{40y}$ did not increase when the pipeline length increased from 2 m to 5 m for with lead shielding case. This is also because the oblique lead shields at both ends of the long pipeline greatly attenuate the dose.

Also, compared with the radiation damage thresholds list in Table 1, with a 5 cm lead shielding, the highest $D_{40y}$ is 908 Gy, lower than the plastics losing tensile strength and natural rubber losing elasticity thresholds.

TABLE 2: $\dot{D}$ and $D_{40y}$ at $Dpi = 30$ cm for 1–5 m pipelines for the spent fuel source term.

| Pipeline length (m) | $\dot{D}$ (mGy/h) | | $D_{40y}$ (Gy) | |
| --- | --- | --- | --- | --- |
| | With no shielding | 4 cm lead shielding | With no shielding | 4 cm lead shielding |
| 1 | 227 | 2.72 | $7.97 \times 10^4$ | 953 |
| 2 | 286 | 2.85 | $1.00 \times 10^5$ | 999 |
| 3 | 306 | 2.86 | $1.07 \times 10^5$ | 1000 |
| 4 | 314 | 2.86 | $1.10 \times 10^5$ | 1000 |
| 5 | 318 | 2.86 | $1.11 \times 10^5$ | 1000 |

TABLE 3: $\dot{D}$ and $D_{40y}$ at $Dpi = 30$ cm for 1–5 m pipelines for the average burn-up fuel source term.

| Pipeline lengths (m) | $\dot{D}$ (mGy/h) | | | $D_{40y}$ (Gy) | | |
| --- | --- | --- | --- | --- | --- | --- |
| | No shielding | 4.5 cm lead | 5 cm lead | No shielding | 4.5 cm lead | 5 cm lead |
| 1 | 371 | 3.49 | 2.49 | $1.30 \times 10^5$ | 1220 | 871 |
| 2 | 467 | 3.66 | 2.59 | $1.64 \times 10^5$ | 1280 | 907 |
| 3 | 498 | 3.66 | 2.59 | $1.75 \times 10^5$ | 1280 | 908 |
| 4 | 511 | 3.66 | 2.59 | $1.79 \times 10^5$ | 1280 | 908 |
| 5 | 518 | 3.66 | 2.59 | $1.82 \times 10^5$ | 1280 | 908 |

So, a 5 cm lead shielding should be added for pipelines that transport fuel elements with different burn-up.

## 4. Conclusions

In this work, the radiation protection design and dose evaluation were performed for the fuel transport pipelines for the HTR-PM reactor, using the shielding calculation software QAD-CGA program. Two types of fuel transport pipelines were considered, i.e., the spent fuel element transport pipelines and different burn-up fuel element transport pipelines. Correspondingly, two source terms were adopted: one is the spent fuel source term and the other is the average burn-up fuel source term. The moving process of a fuel element is discretized and dose calculations were performed to fuel elements at different positions. These doses were integrated with the moving time to obtain the total dose. For pipelines that transport the spent fuel, two scenarios were considered: with no shielding and with a 4 cm lead shielding. For pipelines that transport fuel elements with different burn-up, three scenarios were considered: with no shielding, with a 4.5 cm lead shielding, and with a 5 cm lead shielding. For each case, the point-by-point dose rate by one spent fuel element, the average hourly dose rate from 6000 elements per day, and the cumulative dose of 40 years from 6000 elements per day were calculated. Different Dpi and pipeline lengths were considered. To evaluate the shielding effect, the HTR-PM's orange radiation zone dose limit of 3 mGy/h and the radiation damage thresholds from NCRP report 51 were both adopted. The calculated results indicate that, for pipelines that transport the spent fuel and different burn-up fuel elements, a 4 cm and a 5 cm lead shielding should be added separately.

## Data Availability

The data used to support the findings of this study are available from the corresponding author upon request.

## Conflicts of Interest

The authors declare that they have no conflicts of interest.

## Acknowledgments

## References

[1] Z. Y. Zhang, Y. J. Dong, W. W. Qi et al., "Making dreams come true," Nuclear Engineering International, vol. 64, no. 755, pp. 16–18, 2019.

[2] Z. Y. Zhang, Y. J. Dong, F. Li et al., "The Shandong shidao bay 200 MWe high-temperature gas-cooled reactor pebble-bed module (HTR-PM) demonstration power plant: an engineering and technological innovation," Engineering, vol. 2, pp. 112–118, 2016.

[3] Z. Y. Zhang, Z. X. Wu, D. Z. Wang et al., "Current status and technical description of Chinese 2 x 250 MWth HTR-PM demonstration plant," Nuclear Engineering and Design, vol. 239, pp. 1212–1219, 2009.

[4] Z. Y. Zhang and Y. H. Sun, "Economic potential of modular reactor nuclear power plants based on the Chinese HTR-PM project," Nuclear Engineering and Design, vol. 237, pp. 2265–2274, 2007.

[5] Z. Y. Zhang and Y. L. Sun, "Current status of nuclear power and HTR development in China," Atw-International Journal for Nuclear Power, vol. 51, p. 784, 2006.

[6] S. Fang, H. Li, and W. Q. Li, "Radiation protection calculation and optimization for shielding design around the refueling pipelines of HTR-PM," in Proceedings of the 26th International Conference on Nuclear Engineering, London, UK, 2018.

[7] A. Leal and B. Gamboa, "Dose distribution calculation with MCNP code in a research irradiator," Radiation Physics and Chemistry, vol. 167, p. 5, 2020.

[8] D. B. Pelowitz, *MCNPX User's Manual. 2008. Version 2. 6. 0*, Los Alamos Scientific Lab, New Mexico, USA, 2010.

[9] S. Shalbi, N. Sazali, and W. N. W. Salleh, "A simulation on desired neutron flux for the boron neutron capture therapy (BNCT) purpose by using Monte Carlo N-Particle (MCNPX)," *IOP Conference Series: Materials Science and Engineering*, vol. 736, p. 062022, 2020.

[10] A. Ferrari, P. R. Sala, A. Fasso et al., *FLUKA: A Multi-Particle Transport Code*, CERN European Organization for Nuclear Research, Geneva, Switzerland, 2008.

[11] S. Agostinelli et al., "Geant4—a simulation toolkit," *Nuclear Instruments and Methods in Physics Research Section A*, vol. 506, pp. 250–303, 2003.

[12] Z. M. Hu, Y. H. Zheng, T. S. Fan et al., "Experimental evaluation of the Geant4-calculated response functions of a Bonner sphere spectrometer on monoenergetic neutron sources," *Nuclear Instruments & Methods in Physics Research Section A-Accelerators Spectrometers Detectors and Associated Equipment*, vol. 965, p. 6, 2020.

[13] Y. Harima, "An historical review and current status of buildup factor calculations and applications," *Radiation Physics and Chemistry*, vol. 41, pp. 631–672, 1993.

[14] J. K. Shultis and R. E. Faw, "Radiation shielding technology," *Health Physics*, vol. 88, no. 4, pp. 297–322, 2005.

[15] S. Fang, H. Li, J. Z. Cao et al., "Gamma dose rate estimation and operation management suggestions for decommissioning the reactor pressure vessel of HTR-PM," in *Proceedings of the ASME 2013 15th International Conference on Environmental Remediation and Radioactive Waste Management*, Brussels, Belgium, 2013.

[16] W. Li, X. Liu, L. Ming et al., "Multilayer shielding design for intermediate radioactive waste storage drums: a comparative study between FLUKA and QAD-CGA," *Science and Technology of Nuclear Installations*, vol. 2019, Article ID 8186798, 11 pages, 2019.

[17] W. Li, X. Liu, F. Sheng et al., "Monte Carlo simulation and experimental validation for radiation protection with multiple complex source terms and deep penetration for a radioactive liquid waste cementation facility," *Science and Technology of Nuclear Installations*, vol. 2020, Article ID 8819794, 13 pages, 2020.

[18] R. E. Malenfant, *A Series Of Point-Kernel General Purpose Shielding Programs*, Los Alamos Scientific Lab, New Mexico, USA, 1966.

[19] W. Y. Wang, L. G. Zhang, J. Z. Cao et al., "Optimization of the radiation shielding program QAD," *Nuclear Engineering*, vol. 4, p. 8, 2016.

[20] M. Bell, *ORIGEN-the ORNL Isotope Gened Depletion Code*, Oak Ridge National Lab., Oak Ridge, TN, USA, 1973.

[21] U. Fischer and H. W. Wiese, *Verbesserte Konsistente Berechnung des Nuklearen Inventars Abgebrannter DWR-Brennstoffe auf der Basis von Zell-Abbrand-Verfahren mit KORIGEN*, Institute for Neutron Physics and Reactor Technology Nuclear Research Center, Karlsruhe, Germany, 1983.

[22] W. Li, F. Sheng, and L. Hong, "Research on the induced radioactivity of HTR-PM's reactor pressure vessel: a comparative study between FLUKA, KORIGEN and QAD-CGA," *Annals of Nuclear Energy*, vol. 114, pp. 129–135, 2018.

[23] J. L. Muswema, "Source term derivation and radiological safety analysis for the TRICO II research reactor in kinshasa," *Nuclear Engineering and Design*, vol. 281, pp. 51–57, 2015.

[24] W. H. Yan, "Prototype studies on the nondestructive online burnup determination for the modular pebble bed reactors," *Nuclear Engineering and Design*, vol. 267, pp. 172–179, 2014.

[25] W. Li, F. Sheng, L. Hong et al., "Evaluation of the shielding effect of the spent fuel storage tank cover of HTR-PM: prediction calculation by QAD-CGA program," in *Proceedings of the 27th International Conference on Nuclear Engineering*, Glasgow, UK, 2019b.

*Research Article*

# Source Reconstruction of Atmospheric Releases by Bayesian Inference and the Backward Atmospheric Dispersion Model: An Application to ETEX-I Data

**Yungang Zhao** [iD],[1,2] **Yuanyuan Liu** [iD],[1] **Li Wang**,[3] **Jianping Cheng**,[1] **Shilian Wang**,[2] **and Qi Li**[2]

[1]*Key Laboratory of Beam Technology of Ministry of Education, College of Nuclear Science and Technology, Beijing Normal University, Beijing 100875, China*
[2]*CTBT Beijing National Data Centre and Beijing Radionuclide Laboratory, Beijing 100085, China*
[3]*Department of Physics, Beijing Normal University, Beijing 100875, China*

Correspondence should be addressed to Yuanyuan Liu; yyliu@bnu.edu.cn

Source term reconstruction methods attempt to calculate the most likely source parameters of an atmospheric release given measurements, including both location and release amount. However, source term reconstruction is vulnerable to uncertainties. In this paper, a method combining Bayesian inference with the backward atmospheric dispersion model is developed for robust source term reconstruction. The backward model is used to quantify the relationship between the source and measurements and to reduce the search range of the Bayesian inference. A Markov chain Monte Carlo method is used to sample from the multi-dimensional parameter space of the source term. The source location and release rate are estimated simultaneously, and the posterior probability distribution is produced by applying Bayes' theorem. The proposed method is applied to a set of real concentration data from the ETEX-I experiment. The results demonstrate that the source location is estimated to be $-2.86° \pm 1.01°$E, $48.25° \pm 0.33°$N, and the release rate is estimated to be $20.16 \pm 3.56$ kg/h. The true source location is correctly estimated to be within a one standard deviation interval, and the release rate is correctly determined to be within a three standard deviation interval.

## 1. Introduction

The accurate and timely evaluation of pollutant source (biological, chemical, and radioactive materials) parameters plays an important role in the emergency response. In nuclear accidents, such as the nuclear accident in Fukushima in 2011 and the Ruthenium-106 plume over Europe accident in 2017, the source locations or release rates are unknown. A major concern in these events is how to locate the pollution source and estimate the release rate. An effective way is to reconstruct the source by using environmental monitoring data and a dispersion model. Such methods have been applied to wind tunnel experiments [1, 2], tracer experiments [3, 4], and real accidents such as nuclear accidents

[5, 6] and radionuclide emissions under normal conditions [7].

Among these studies, two notable methods include Bayesian inference and the backward atmospheric model. Compared with deterministic optimization methods which provide a single optimal solution, Bayesian inference can provide a probability distribution of the source parameters based on the prior information of unknown parameters and monitoring data, but this method is time consuming for enormous sampling [8]. The backward atmospheric model can rapidly provide the possible source region for each measurement site, but it relies on further analysis to quantitatively determine the position and release rate of the source [9].

However, there are few reports on the combination of Bayesian inference and a backward atmospheric model.

For robust source term reconstruction, a new method combining Bayesian inference with the backward run model FLEXPART is proposed in this study. The source-receptor relationship and the possible source region are obtained through backward simulations. A Bayesian method combined with MCMC sampling is used to estimate the source term position and release rate simultaneously, together with their posteriori distributions. The proposed method is validated using the ETEX-I experiment by comparing both the source parameters and the concentration simulations.

## 2. Methodology

The source term reconstruction method based on Bayesian inference is a method that combines the prior information of unknown parameters with measurements to transform them into posterior information, and it has been applied to different scenarios [10–12]. The following sections briefly summarize Bayesian inference for source reconstruction and the derivation of the source-receptor relationship.

*2.1. Bayesian Inference for Source Reconstruction.* The aim of Bayesian inference for source reconstruction is to determine the a posteriori probability distribution of source parameters. The governing equation is Bayes' theorem, which can be expressed as follows:

$$P(S \mid M) = \frac{P(M \mid S)P(S)}{P(M)}, \tag{1}$$

where $S$ is the state vector formed by the source parameter and $M$ is a vector formed by the measurements.

The terms in equation (1) can be identified as follows. First, $P(S)$ is the prior probability for the source parameters prior to any knowledge. It mainly comes from previous data, historical experience, and subjective judgment. The prior probability distribution includes uniform and normal distribution. Second, $P(M \mid S)$ is the likelihood function and is the probability given the source parameter $S$, which indicates the fitness between the modeled and measured concentrations. Here, we define the likelihood function as the normal distribution function.

$$P(M \mid S) = \frac{1}{\prod_{i=1}^{N} \sqrt{2\pi}\sigma_i} \exp\left(-\frac{1}{2}\sum_{i=1}^{N}\left(\frac{M_i - C_i}{\sigma_i}\right)^2\right), \tag{2}$$

where $N$ is the number of monitoring data, $M_i$ is the $i$th monitoring data, $C_i$ is the $i$th data predicted by the atmospheric transport model for a known source $S$, which will be described in Section 2.2, and $\sigma_i$ is the error between $M_i$ and $C_i$. Third, $P(M)$ is the integration of $P(M \mid S)$ $P(S)$ at all source parameters and is referred to as the evidence. It can be simply a normalization constant. Finally, $P(S \mid M)$ is the posterior distribution and the answer for the source reconstruction.

*2.2. Source-Receptor Relationship (SRR).* The determination of the likelihood function requires the computation of $C_i$, i.e., the simulated concentrations. Because Bayesian inference requires a repeated computation of $C_i$, a direct simulation using an atmospheric dispersion model can be highly computationally demanding. An alternative method is to calculate a matrix representing the relationship between the release source and the concentration at the stations and to use matrix-vector multiplication instead. This matrix is called a source-receptor relationship. The advantage of calculating an SRR is that the calculation of the simulated concentration can avoid the numerical modeling process, which usually takes several minutes or hours. There are two ways to obtain the SRR: one is based on the source, using forward simulation. A forward simulation can establish the relationship between one source $(x_0, y_0, q_0)$ and a series of monitoring data $C$ $(C_1, C_2, \ldots, C_N)$; the other is based on the receptor, using backward simulation [13]. By reversing the sign of the advection, a large number of particles are released at the receptor and transported backward in time. The residence time in the grid is proportional to the contribution of a source in the grid cell. One backward simulation can establish the relationship between one monitoring dataset $C_i$ and a series of source data through the residence time $t_r$. When we fix the source parameters, the concentration $C_i$ at a station can be computed as follows:

$$C_i = \frac{qt_r}{V dt}. \tag{3}$$

$V$ is the grid volume, which is calculated based on the grid setting parameters, including the grid resolution and level heights, and $dt$ is the time resolution in the ATM. A more detailed description of the backward simulation can be found in [13].

In the case of unknown source term locations, the possible number of source term locations is generally much larger than the number of monitoring data. More simulations are needed in the forward mode than in the backward mode. Under this condition, the backward simulation is more efficient than the forward simulation in computational cost.

## 3. Sampling Method and Convergence

Markov chain Monte Carlo (MCMC) algorithms [14] are commonly used to generate random samples to obtain the posterior probability density function of source parameters. Many MCMC algorithms have been developed, including the Metropolis–Hastings (M-H) algorithm and Gibbs algorithm. Currently, the M-H algorithm is commonly used in source term reconstruction research; during one M-H sampling, parameters are disturbed simultaneously.

The process of the M-H algorithm is as follows:

(1) Initiation: generate the initial point $I = (x_0, y_0, q_0)$ depending on the prior probability.

(2) Perturbation: the new source $I' = (x_0 + dx, y_0 + dy, q_0 + dq)$ is obtained by unbiased perturbation.

(3) Accept or reject: the likelihood functions $P(M \mid I)$ and $P(M \mid I')$ are calculated and compared, and the ratio $\Delta p = P(M \mid I')/P(M \mid I)$ is obtained. At the same time, a random number $r$ between $[0, 1]$ is generated. When $R \leq \Delta P$, $I'$ is accepted; otherwise, $I'$ is rejected.

(4) Iteration: repeat Steps 2 and 3 until the convergence condition is reached.

In practice, the convergence condition is reached when the posterior distribution is stable. For MCMC sampling with multiple chains, the between-chain variance $B$ and within-chain variance $W$ are generally used to evaluate the convergence of sampling results [15]. For $m$ Markov chains of length $n$, the variance between chains $B$ is

$$B = \frac{n}{m-1} \sum_{j=1}^{m} \left( \overline{S_j} - \overline{S} \right), \tag{4}$$

where

$$\overline{S_j} = \frac{1}{n} \sum_{i=1}^{n} s_{ij},$$
$$\overline{S} = \frac{1}{m} \sum_{j=1}^{m} \overline{S_j}. \tag{5}$$

The within-chain variance $W$ is

$$W = \frac{1}{m} \sum_{j=1}^{m} w_j^2, \tag{6}$$

where

$$w_j^2 = \frac{1}{n-1} \sum_{i=1}^{n} \left( s_{ij} - \overline{S_j} \right)^2. \tag{7}$$

The convergence value is

$$\mathrm{Cov} = \frac{\mathrm{var}(S)}{W}, \tag{8}$$

where

$$\mathrm{var}(S) = \frac{n-1}{n} W + \frac{1}{n} B. \tag{9}$$

The posterior distribution of the source parameters can be obtained by statistical analysis of the stable results after the chains reach the convergence condition.

Therefore, the implementation process of source term reconstruction can be shown in Figure 1.

## 4. Application

*4.1. Benchmark.* In this section, the proposed methods are used to evaluate the source term location and release rate of ETEX-I.

ETEX-I is an atmospheric tracer experiment organized by many European countries [16]. It was carried out from October to November 1994. The tracer used was PMCH. The source location was Monterfil, Brittany, France ($-2.0083°$E, $48.058°$N). A total of 168 monitoring stations were set up in 17 countries, and 3104 available monitoring data points were obtained. The monitoring stations and the release point are shown in Figure 2.

To investigate the ability of source term reconstruction with less monitoring data, only 11 stations with 58 monitoring data points were selected, including detection and no-detection data points. The distribution of selected stations is also shown in Figure 2.

*4.2. Atmospheric Transport Model and Meteorological Data.* The atmospheric transport model used in this work is FLEXPART V8.2 [17]. The meteorological data are NCEP Climate Forecast System Reanalysis (CFSR) 6-hour products [18], a global gridded dataset with a spatial resolution of $0.5° \times 0.5$ and temporal resolution of 6 h.

The FLEXPART model is a Lagrangian particle diffusion model developed by Norwegian Atmospheric Research Institute. It can run in both forward and backward modes. This work mainly uses the backward mode. Based on the site locations and sampling information of the measurements, the backward simulation of each monitoring data point is carried out, and parts of the results are shown in Figure 3. The backward simulations show that the possible source region moves from the stations to the true source point.

*4.3. Prior Distribution of Source Term Parameters.* According to Section 4.2, the backward simulation results, the possible sources are mainly distributed in Central and Western Europe, Southern England, and the surrounding maritime areas. Based on these results, the sampling space of source term parameters is set as follows: longitude ($-10° \sim 10°$E), latitude ($45° \sim 55°$N), and release rate ($0 \sim 100$ kg/h). In this paper, assume the prior distribution of parameters is uniform. According to the prior distribution density function, 1000 source terms are generated as the initial points of the MCMC chain.

## 5. Results

*5.1. Convergence.* Source terms are iterated according to the sampling method in Section 3, and the iterative result of location parameters of one chain is shown in Figure 4. The initial point is located at ($7.5°$E, $53.25°$N). During the iterative calculation of Figure 1, the refined source term gradually approaches the true source location and finally stabilizes near the true source location.

The evolution of the mean value and standard deviation of the estimated source parameters is calculated and shown in Figure 5. After 3000 iterations, the mean values of all three parameters become stable. The standard deviations also show obvious reductions for all three estimated parameters. For latitude, the standard deviation is $0.33°$ at the steady state, which is the smallest among the three parameters. The standard deviation of the longitude is slightly larger, which is $1.01°$ at the steady state. This phenomenon demonstrates that
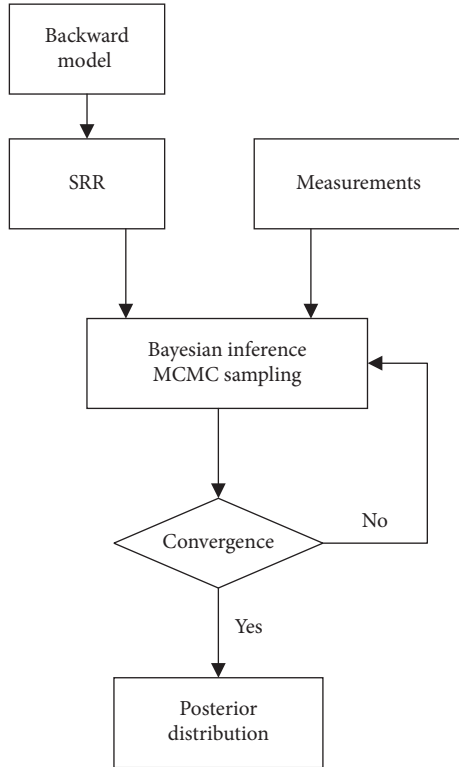
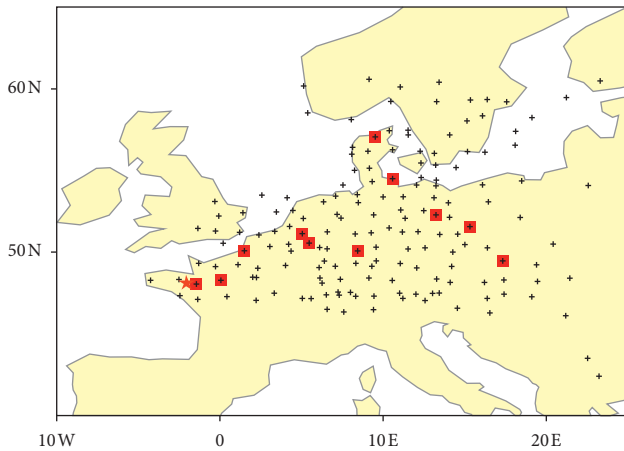FIGURE 1: Flowchart of source term reconstruction via Bayesian inference.



FIGURE 2: ETEX-I monitoring stations and the release point. The red star indicates the source release point, the black cross indicates 168 monitoring stations, and the red square indicates the station measurements selected in this work.

the uncertainties in the estimation of the two location parameters can be different. For the release rate, the standard deviation is 3.56 kg/h.

Based on the convergence method in Section 3, the convergence values of source term parameters are calculated. Figure 6 shows that, among the three parameters of longitude, latitude, and release rate, latitude converges fastest, and the release rate converges the slowest. The

relatively better convergences of the location parameters may be attributed to the better initial values provided by the backward simulations in Section 4.2.

*5.2. Estimated Results.* Figure 7 displays the posterior probability distributions of the parameters. The sampling results and true source parameters based on the prior distribution of source terms are also shown in Figure 7. The posterior probability distribution reveals that the mean value, the standard deviation, and the most likely value of the source parameters are $-2.86° \pm 1.01°$E ($-2.25°$E), $48.24° \pm 0.33°$N ($48.25°$N), and $20.16 \pm 3.56$ kg/h ($21.0$ kg/h). Figure 7(a) shows the longitude values' posterior distribution. The distribution has two peaks to the west of the true point, with deviations of $0.25°$ and $1.5°$. The two peaks are highly influenced by the wind field, which is mainly from west to east. Figure 7(b) shows the posterior distribution of latitude values. The majority of the values are within $0.5°$ of the true value. Figure 7(c) shows the release rate values of the accepted states. The release rate was correctly determined to be within a three standard deviation interval. The difference between the estimated release rate and the true value mainly comes from the model error. The statistics of the a posteriori distribution are listed in Table 1. Generally, the most likely values are closer to the true values than the mean values. These results indicate that the most likely estimate may be more reliable for source reconstruction in a real nuclear accident. Compared with the location, the release rate shows relatively larger errors and standard deviations.

*5.3. Comparison of Simulations and Measurements.* The observed concentrations and concentrations simulated by using different source terms were compared to validate the proposed source reconstruction methods.

(i) FWD_t: forward simulation with the true source term

(ii) FWD_m: forward simulation with the mean source term in Table 1

(iii) FWD_p: forward simulation with the most probability source term in Table 1

Figure 8 shows the plumes modeled by different source terms at different times. It is noticeable that the plume shapes are similar to each other for the same times, indicating that the meteorological input plays a dominant role in the simulation. Although the two estimates have relatively large differences in their longitude (Table 1), the concentration distributions are generally much the same, especially for the latter times (the middle and right columns of Figure 8). This phenomenon implies that the simulation is not that sensitive to the displacement of the source positions. However, the high-concentration area of the simulation using the true source term is quite different from that using the most likely and mean estimate, indicating that the release rate differences have a larger influence on the simulation. These differences in sensitivities to the source coordinate and
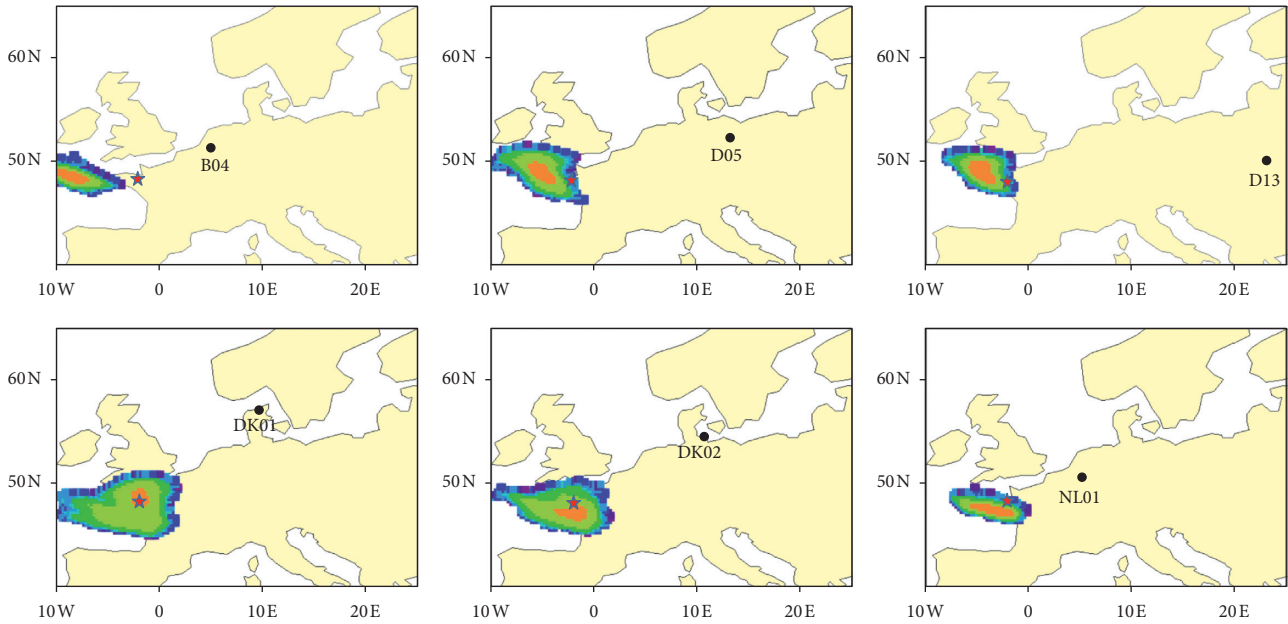
FIGURE 3: Backward simulation results. The red star indicates the source release point, and the black circle indicates the monitoring station.
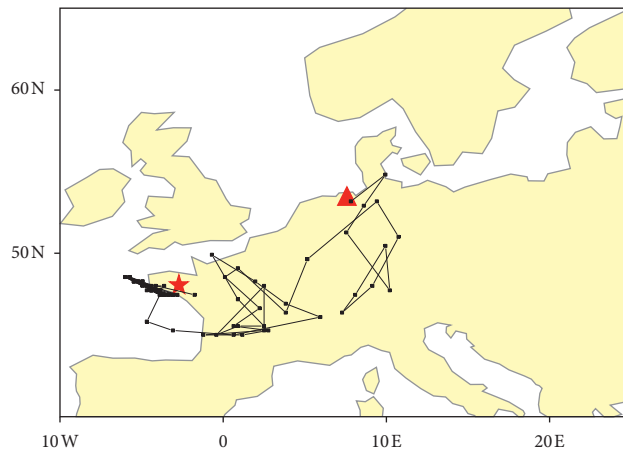


FIGURE 4: A Markov chain Monte Carlo sampling result for the source term location. The red triangle indicates the initial point, and the red star indicates the true source location.

the release rate may partially explain different deviations of the source reconstruction for these two variables (Table 1). At some measurements in the center of the plume, the simulation with the true release rate exhibits even larger deviations than the simulations using the other two source term estimates (the first column in Figure 8). This phenomenon indicates that the air dispersion model may have its own deviations, and such deviations are cancelled out by the deviations in the most likely estimate and the mean estimate to some degree. For those measurements outside the plume, the uncertainties in the meteorological input can be the major source of these deviations.

Figure 9 compares the temporal profiles of the observed and simulated concentrations at representative sites. For all 4 sites, the simulated timings of the peaks generally show deviations within a 3 h interval compared with the monitoring results, whereas the deviations of the simulated peak

values are within 50% at these four sites. For more than 70% of stations, the deviations in the estimation of the peak values are within a factor of 5. There is also a difference in the number of peaks between the simulations and measurements. Taking station D06 as an example, a small peak is shown behind the main peak in the measurement data, while it is not shown in the simulated data. Again, it is noticeable that the simulated profiles using the true release rate show the most obvious deviations at D05 and D13, which significantly overestimate the number and magnitude of the peaks. For the other two source terms, the simulated peak timing is basically the same, but the peak values are different. Thus, in addition to the release rate, it is also necessary to reduce the uncertainties in the input meteorological fields and the physical processes of the dispersion model to improve the simulation results. This improvement shall be our future work.
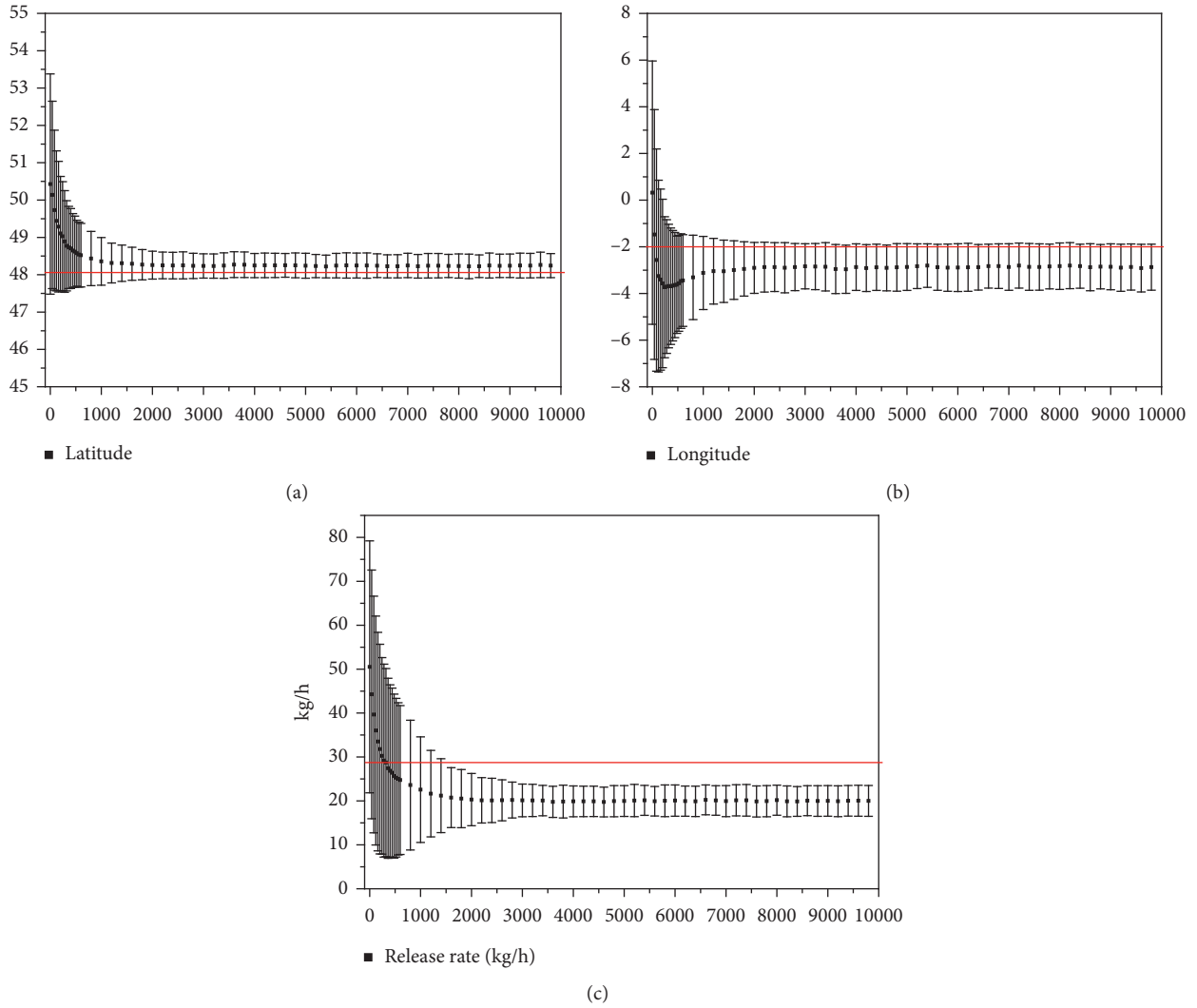
(a)



(b)



(c)

FIGURE 5: The mean values and standard deviations of source parameters after iterating: (a) latitude; (b) longitude; (c) release rate.
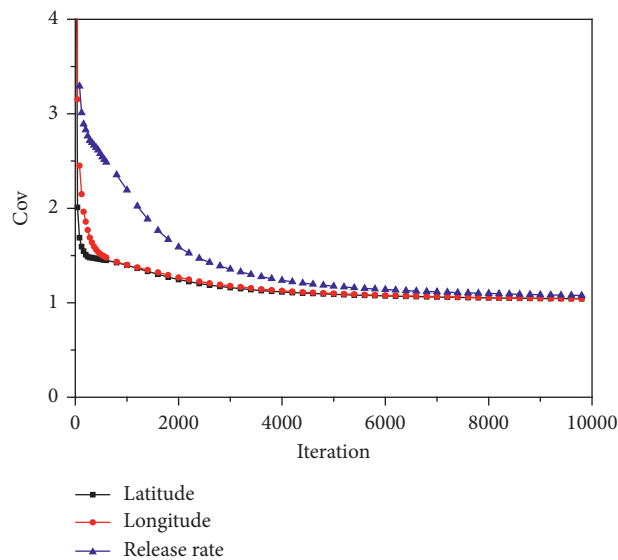


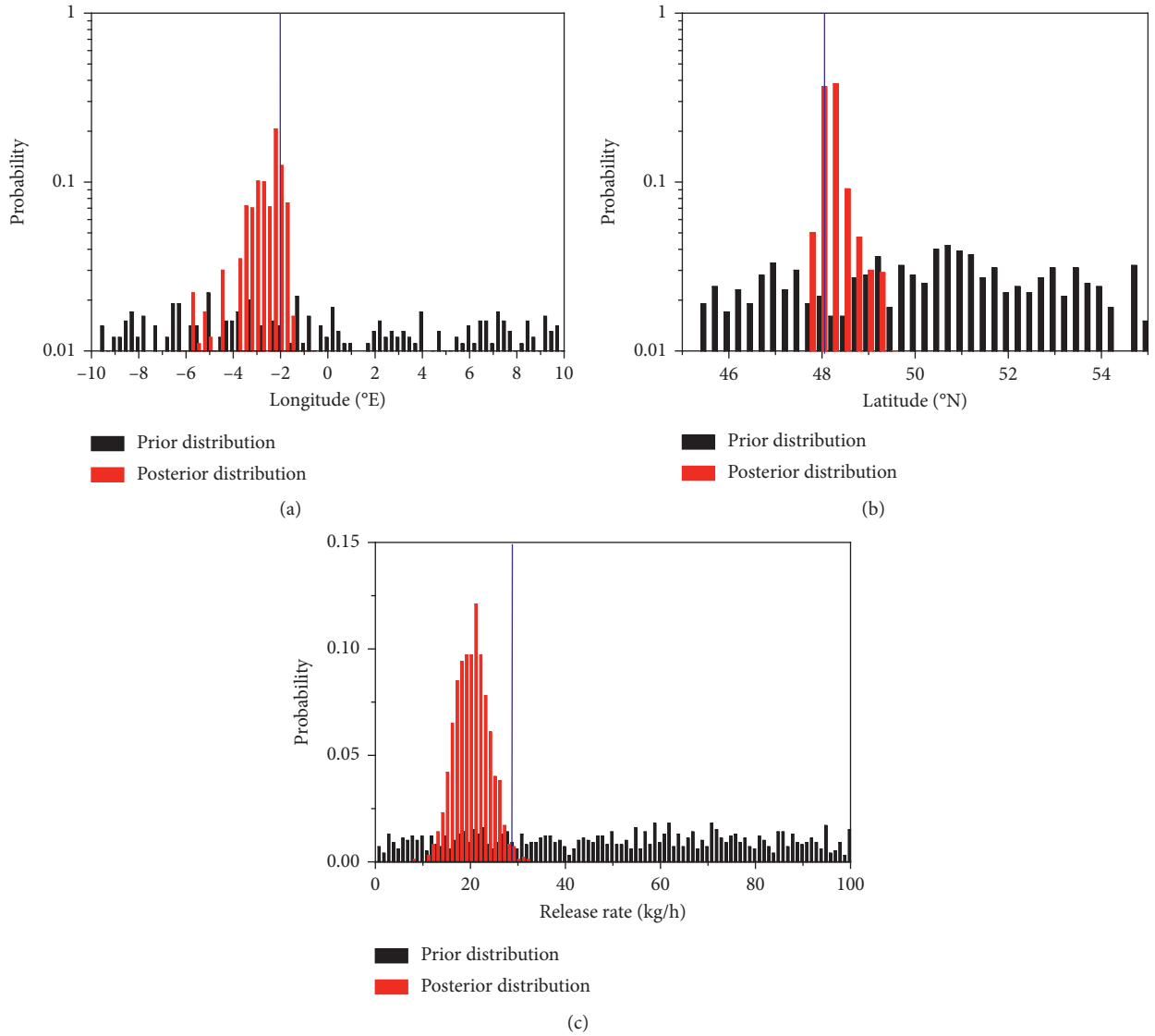FIGURE 6: Convergence values vs. the number of iterations.

(a)



(b)



(c)

FIGURE 7: Prior distribution (black bar), posterior distribution (red bar), and true value (blue bar) of source term parameters.

TABLE 1: Summary statistics of the MCMC samples.

| | Lon (°E) | Lat (°N) | Rate (kg/h) |
|---|---|---|---|
| Most prob | −2.25 | 48.25 | 21.0 |
| Mean | −2.86 | 48.24 | 20.16 |
| Standard deviation | 1.01 | 0.33 | 3.56 |
| True | −2.0083 | 48.058 | 28.73 |

Table 2 compares the quantitative metrics of the simulations using three different source terms. The simulations using the true release rate exhibit the worst metrics except

for the correlation $R$, implying that the model uncertainties may be further reduced. For the other two source terms, their performances are quite close to each other, except FB.
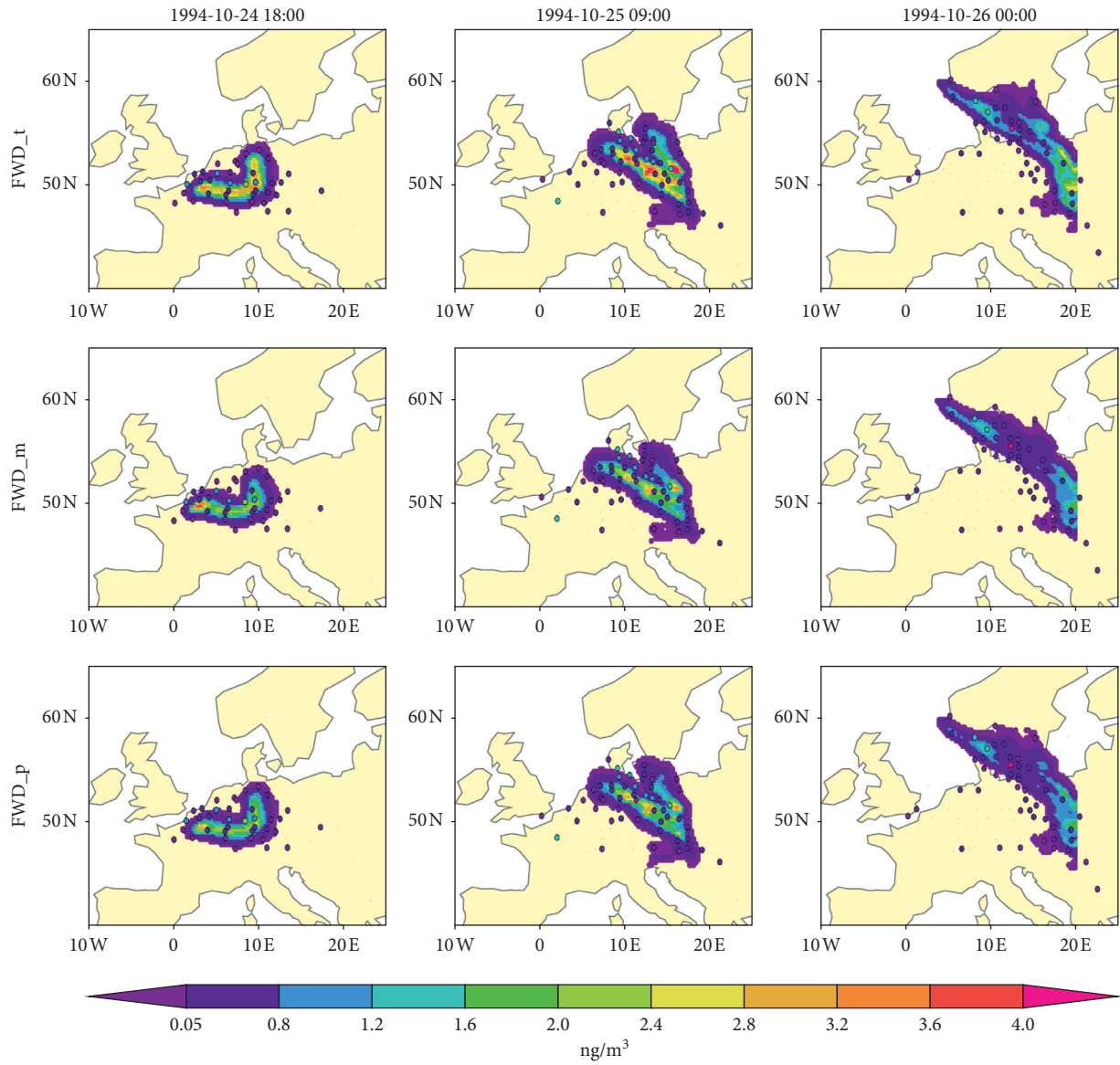
Figure 8: Comparison of simulated plumes by different methods for (top) FWD_t, (middle) FWD_m, and (bottom) FWD_p and measurements for different times: (left) 1994-10-24 18:00, (middle) 1994-10-25 09:00, and (right) 1994-10-26 00:00. The circles are the monitoring data.
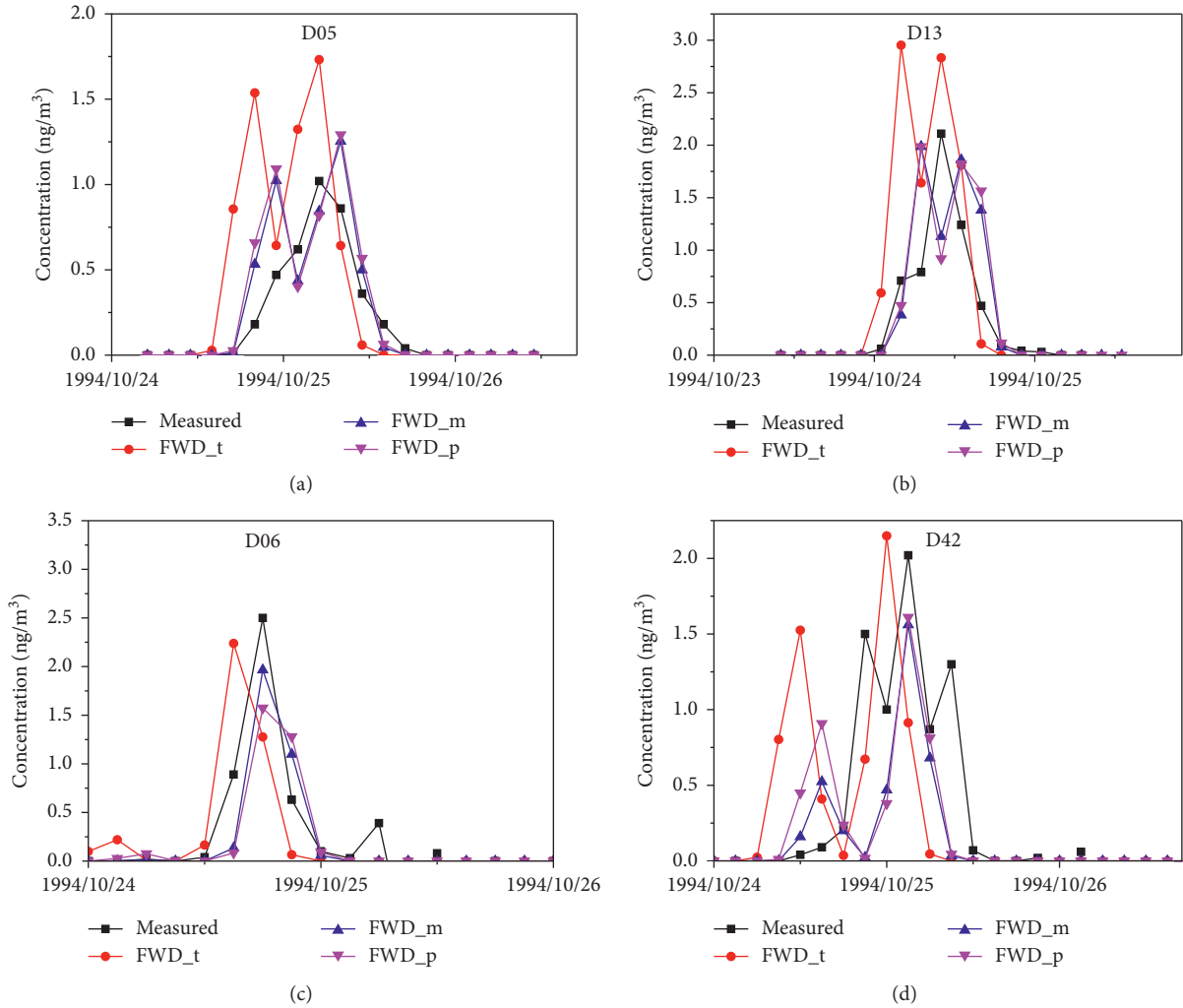
FIGURE 9: Comparison of simulations and measurements at different stations. (a) D04 and (b) D13 are stations used in the source reconstruction. (c) D06 and (d) D42 are stations not used in the source reconstruction.

TABLE 2: Statistical performance indicators for the comparison modeled-measured tracer concentrations. Data at all the 168 stations are used.

| Method | $R$ | FB | FA2 | FA5 | Source |
|---|---|---|---|---|---|
| FWD_t | 0.54 | 0.71 | 0.21 | 0.48 | True |
| FWD_m | 0.28 | 0.12 | 0.27 | 0.56 | Mean |
| FWD_p | 0.30 | 0.33 | 0.26 | 0.56 | Most prob |

## 6. Conclusion and Discussion

This paper introduces a method to reconstruct the source parameters given a set of measurements. The method combines Bayesian inference (MCMC sampling) and ATM backward simulation and provides the a posteriori probability distributions of the source term. The method has been applied to a tracer experiment (ETEX-I) that occurred in 1994 in Europe. The relationship between the source and receptor is obtained by using the backward run mode of FLEXPART, which reduces the calculation requirement of the likelihood function in a large number of iterative

samplings and improves the calculation efficiency. The reconstructed results are in good agreement with the true parameters of the source term. The position uncertainty was within 1.0°, and the deviation between the release rate and the real rate was within 3 times the standard deviation. After 3000 iterations, the method converges to a steady state, providing not only a single solution but also a posteriori probability distribution. Meanwhile, we find that the validation between the simulation using different source terms and the observation demonstrates that the major uncertainties come from the air dispersion model, including both the meteorological input and the physical process models.

The reduction of these uncertainties can improve the source reconstruction accuracy, which will be addressed in our future work.

## Data Availability

The data used to support the findings of this study are available from the corresponding author upon request.

## Conflicts of Interest

The authors declare that they have no conflicts of interest.

## References

[1] X. Li, H. Li, Y. Liu, W. Xiong, and S. Fang, "Joint release rate estimation and measurement-by-measurement model correction for atmospheric radionuclide emission in nuclear accidents: an application to wind tunnel experiments," *Journal of Hazardous Materials*, vol. 345, pp. 48–62, 2018.

[2] S. Fang, S. Zhuang, and X. Li, "Automated release rate inversion and plume bias correction for atmospheric radionuclide leaks: a robust and general remediation to imperfect radionuclide transport modeling," *Science of The Total Environment*, vol. 754, Article ID 142140, 2019.

[3] L. Robertson and J. Langner, "Source function estimate by means of variational data assimilation applied to the ETEX-I tracer experiment," *Atmospheric Environment*, vol. 32, no. 24, pp. 4219–4225, 1998.

[4] M. Bocquet, "High-resolution reconstruction of a tracer dispersion event: application to ETEX," *Quarterly Journal of the Royal Meteorological Society*, vol. 133, no. 625, pp. 1013–1026, 2007.

[5] S. Sun, H. Li, and S. Fang, "A forward-backward coupled source term estimation for nuclear power plant accident: a case study of loss of coolant accident scenario," *Annals of Nuclear Energy*, vol. 104, pp. 67–74, 2017.

[6] X. Li, S. Sun, and X. Hu, "Source inversion of both long- and short-lived radionuclide releases from the Fukushima Daiichi nuclear accident using on-site gamma dose rates," *Journal of Hazardous Materials*, vol. 379, Article ID 120770, 2019.

[7] E. Yee, I. Hoffman, and K. Ungar, "Bayesian inference for source reconstruction: a real-world application," *International Scholarly Research Notices*, vol. 2014, Article ID 507634, 2014.

[8] G. Kastner and F. Huber, "Sparse Bayesian vector autoregressions in huge dimensions," *Journal of Forecasting*, vol. 39, no. 7, pp. 1142–1165, 2008.

[9] J. Sørensen, H. Klein, and M. Ulimoen, "Source localization by inverse methods," 2020, http://www.nks.org/scripts/getdocument.php?file=111010214696504.

[10] L. Monache, J. Lundquist, and B. Kosović, "Bayesian inference and Markov chain Monte Carlo sampling to reconstruct a contaminant source on a continental scale," *Journal of Applied Meteorology and Climatology*, vol. 47, no. 10, pp. 2600–2613, 2008.

[11] E. Yee, "Automated computational inference engine for Bayesian source reconstruction: application to some detections/non-detections made in the CTBT international monitoring system," *Applied Mathematical Sciences*, vol. 11, no. 32, pp. 1581–1618, 2017.

[12] D. L. Brazidec, J. Bocquet, and M. Saunier, "Quantification of the modelling uncertainties in atmospheric release source assessment and application to the reconstruction of the autumn 2017 Ruthenium 106 source," *Atmospheric Chemistry and Physics*, vol. 4, 2021.

[13] P. Seibert and A. Frank, "Source-receptor matrix calculation with a Lagrangian particle dispersion model in backward mode," *Atmospheric Chemistry and Physics*, vol. 4, no. 1, pp. 51–63, 2004.

[14] W. R. Gilks, S. Richardson, and D. Spiegelhalter, *Markov Chain Monte Carlo in Practice*, Chapman & Hall/CRC Press, London, UK, 1996.

[15] A. Gelman, J. B. Carlin, and H. S. Stern, *Bayesian Data Analysis*, CRC Press, Boca Raton, FL, USA, 3rd edition, 2013.

[16] H. Dop, G. Graziani, and W. Klug, "ETEX: a european tracer experiment," *Large Scale Computations in Air Pollution Modelling*, vol. 57, pp. 137–150, 1999.

[17] S. Eckhardt, A. Stohl, and H. Sodemann, "The Lagrangian particle dispersion model FLEXPART version 8.0," 2020, https://folk.nilu.no/%7Eandreas/flexpart/flexpart8.pdf.

[18] S. Saha, S. Moorthi, and X. Wu, "NCEP climate forecast system reanalysis (CFSR) 6-hour products," *Computational and Information Systems Laboratory*, vol. 93, 2021.

*Research Article*

# Study on Release and Migration of Radionuclides under the Small Break Loss of Coolant Accident in a Marine Reactor

**Zhao Fang** [ID],[1,2] **Zou Shuliang** [ID],[1,2] **Liu Zejun,**[3] **Xu Tao,**[4] **Xu Shoulong,**[1,2] **Huang Yan,**[1,2] **and Feng Jinjun**[3]

[1]*School of Resource Environment and Safety Engineering, University of South China, Hengyang 421001, Hunan, China*
[2]*Hunan Provincial Key Laboratory of Emergency Safety Technology and Equipment for Nuclear Facilities, Hengyang 421001, Hunan, China*
[3]*Nuclear and Radiation Safety Center in China, Beijing 100082, China*
[4]*Science and Technology on Reactor System Design Technology Laboratory, Nuclear Power Institute of China, Chengdu 610213, Sichuan, China*

Correspondence should be addressed to Zou Shuliang; zousl2013@126.com

Using severe accident analysis program MELCOR, the small break loss of coolant accident (SBLOCA) analysis model was established for a marine reactor. The release and migration of radionuclides were analyzed during a severe accident induced by SBLOCA. The analysis of the hydrogen source term release showed that the maximum hydrogen release amount was 248.567 kg, and the hydrogen release amount accounted for less than 4% of the air volume. So, there would be no danger of hydrogen explosion accidents. The research mainly focused on the behaviors of the release, the transport, the retention, and the final distribution of inert gases represented by Xe, volatile gases represented by CsI, and nonvolatile nuclides represented by Ba. The results showed that the reactor core exposed completely with a lagging by 510 s and the initial release time of nuclides was lagged by 1916 s. The release shares of Xe in the primary circuit system, the containment, and the environment were 0.013%, 0.06%, and 32.71%, respectively. Also, Ba shared 0.016%, 0.0032%, and 3.28%, respectively, and CsI shared 0.0145%, 0.0012%, and 2.845%, respectively.

## 1. Introduction

The research on the source term during severe accidents in marine nuclear reactors is still insufficient. During sailing on the sea, ships driven by nuclear reactors may experience a violent rocking collision or other accidents, which may cause severe accidents in the nuclear reactors. Also, due to the small spaces and limited deadweights of the nuclear reactors, their safety facilities are usually not so perfect compared with those for stationary nuclear power plants [1]. Thus, the occurrence probability of severe accidents in marine nuclear reactors is higher than that in land-based nuclear reactors. Therefore, it is necessary to study severe accidents in marine nuclear reactors to clarify their source terms [2].

Xuefeng et al. [3] studied the hydrogen source term during a loss of coolant accident in a marine nuclear reactor and researched the hydrogen risk and the hydrogen control system in the marine nuclear reactor. The hydrogen generation rate and steam release rate are calculated, and the three-dimensional computational fluid dynamics code GASFLOW was employed to simulate the two-dimensional flow field and the transport and distribution of hydrogen in the cabin. Kehan Ouyang et al. [4] analyzed the atmospheric radioactive dispersion caused by a severe accident in a marine nuclear reactor. Based on the Lagrangian particle, a tracking model to simulate atmospheric diffusion of radionuclides above the sea was established. The influences of sea absorption on the atmospheric diffusion of radionuclides emitted at different heights were analyzed. It mainly focuses

on the research on the diffusion of hydrogen source term and fission products outside the cabin. There were few pieces of research on the release and migration of other radionuclides in the ship's reactor cabin.

Zhang et al. [1] and Wang Wei et al. [5, 6] conducted source term analysis during a severe accident induced by large break loss of coolant caused by the whole ship blackout due to the rupture of a tube of the steam generator. They also focus on the release and migration trends of the inert gas Xe and the volatile gas CsI as well as the release share distribution trends in the cabin. Zhan et al. [7] analyzed the radioactive release accident caused by the interruption of power supply and safety valve failure under four operating conditions, which were 1 time, 5 times, 13 times, and reiterative times of the opening of the pressurizer safe valve. The release and migration of radionuclides emitted from a marine nuclear reactor caused by multiple severe accidents and superimposed accidents were mainly studied. But the source term analysis associated with serious accidents caused by a single small breach was not well studied.

This research analyzed a marine reactor by adopting the MELCOR [8–10]. The calculation model of the severe accident in a nuclear reactor was established to study the release and migration characteristics of radionuclides under SBLOCA.

## 2. Methods

### 2.1. Nodalization of Marine Reactor.
The research object was a natural circulation small modular light-water reactor with the thermal power of 330 MW. The marine reactor model mainly included reactor pressure vessel (RPV), the pressure containment vessel (PCV), the containment pool (CP), the passive safety system (PSS), the pressurizer, the steam generator (SG), and the passive decay heat removal system (PDHRS). This model used 40 control volumes and 26 connection channels to simulate the main compartment divisions in the containment, as shown in Figure 1. Nodalization can reflect the release and migration of radionuclides in a marine reactor after the occurrence of an SBLOCA event. The main hydraulic regions in RPV were modeled by different control volumes, which included the reactor core (CV170), the bypass region (CV180), the upper head 1 (CV190), the upper head 2 (CV191), the pressurizer (CV500), the SG primary side (CV230-CV239), the SG secondary side (CV630-CV639), the downcomer (CV240), and the lower head (CV150). Figure 1 shows that the SG primary side and secondary side were divided into 10 nodes each along the flow direction for the detail calculation. Some regions (CV231, CV232, CV603, and CV604) at the inlet of pressurizer and the outlet of SG were also modeled for accurate modeling.

For the main steam system and PDHRS, the main steam head (CV621) and the feedwater head (CV620) were modeled. The volume in PCV consisted of the cavity (CV810) and the containment (CV830). The environment in the area outside the containment was represented by a large control volume (CV950) with constant pressure and temperature. The control volumes were connected by the flow path which is presented by arrows in the Figure 1. The valves such as the safety relief valves (SRVs), the reactor

recirculation valves (RRVs), the reactor venting valves (RVVs), and main steam isolation valves were modeled in the corresponding flow path.

### 2.2. Nodalization of Reactor Core.
More detailed nodalization of the reactor core in the MELCOR was conducted for simulating the complex physical and chemical phenomena. Figure 2 shows the core nodalization for a marine reactor. The lower plenum was simplified as a cylinder and nodalized with the reactor core and the lower head was flat as a platform. The core and lower plenum were divided into 5 concentric radial rings and 16 axial rows. The bottom four axial rows 1 to 4 represented the lower plenum, while the top rows 6 to 15 represented the active core area. Row 5 represented the lower inactive core area, and row 16 represented the higher inactive core region. The fourth row represented the core support plate which is an important key structure in the reactor core because the core support plate has a great influence on the core displacement process. The particular ring and row formed a core node or core cell (for example, node 203 meant the 2nd ring and 3rd row). The lower head of the marine reactor was of steel structure corresponding to the core ring. It was also divided into 5 rings.

### 2.3. Analysis of Accident Progress.
At 500 s, a small break loss of coolant accident occurred. The containment ruptured, and the passive decay heat removal system failed. The pressure in the main system dropped sharply, and the containment pressure increased rapidly. At the same time, the reactor was shut down due to the low pressure in the main system. When the break occurred, the primary circuit system coolant was quickly released to the reactor cabin through the break, resulting in the loss of a large amount of coolant, and a rapid drop of the water level in the reactor core. At 46,900 s, the core active area was completely exposed. After the exposure of the core, the temperature of the fuel elements and the cladding continued to rise, and the gap release phase started.

At 64,400 s, the bottom of the core dried up, and the core support plate began to fail. When the molten core melted through the core support plate, it fell into the lower chamber and contacted the lower head to exchange heat. Then, the lower head crept and broke, and the lower head failed. The core melted and fell into the pit and the release phase outside the pressure vessel started.

The accident was initiated by the SBLOCA in the pressurizer at 500 s. As illustrated in Figure 3, the RPV pressure quickly decreased once the RVV was opened, and the PCV pressure meanwhile increased. Large amount of core materials relocated to the lower plenum after the core support plate in different rings failed. The melt core materials, with decay heat, accumulated in the lower plenum formed a debris bed and interacted with the lower head wall, raising the wall node temperature as shown in Figure 4.

### 2.4. Calculation Model of Radionuclide Release.
Radioactive material may be released from the core. The radionuclides residing in the core (COR) package fuel are
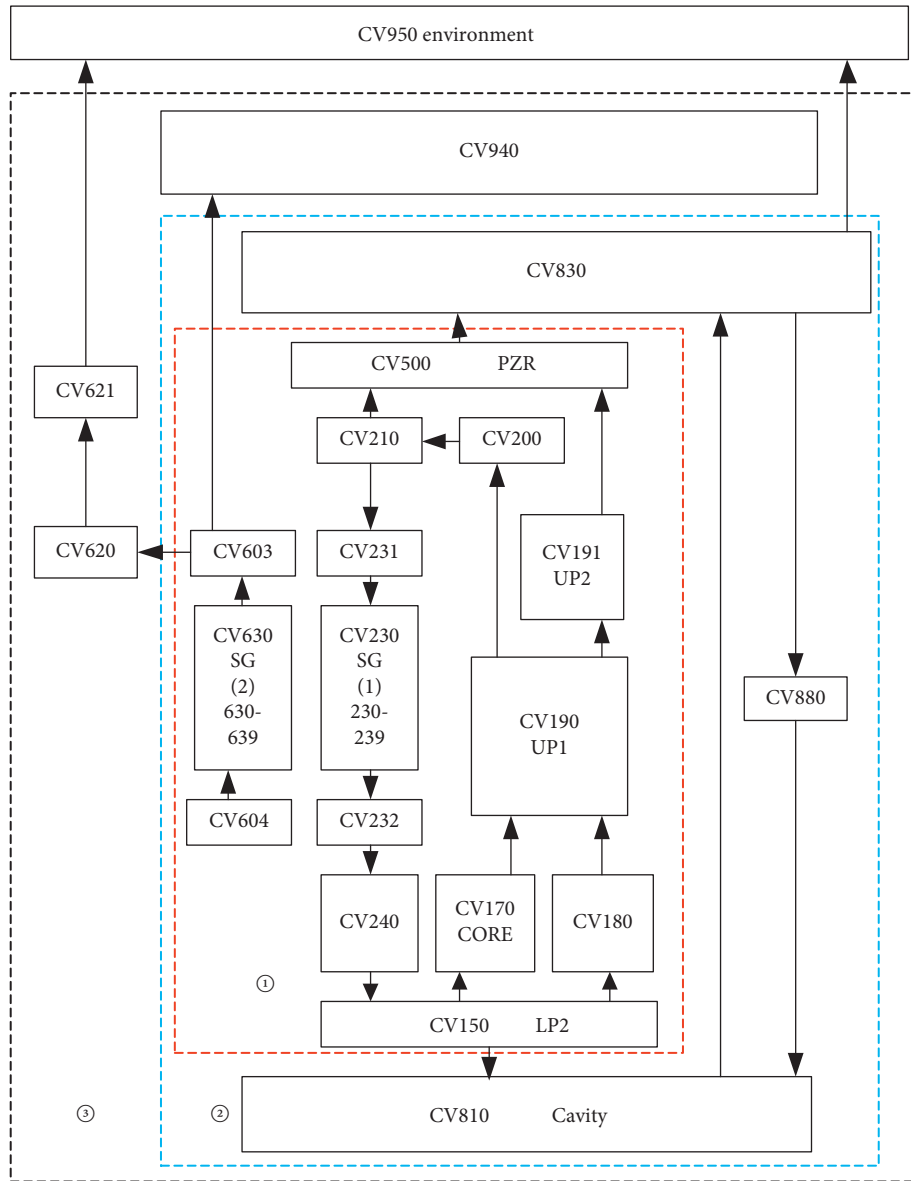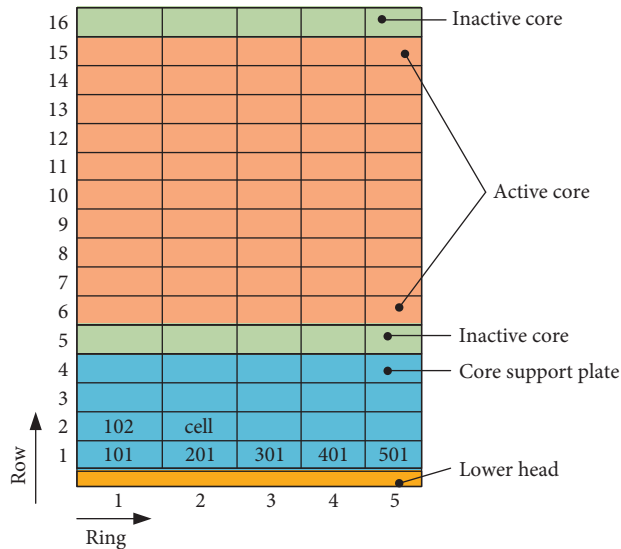
Figure 1: Nodalization of the marine reactor.



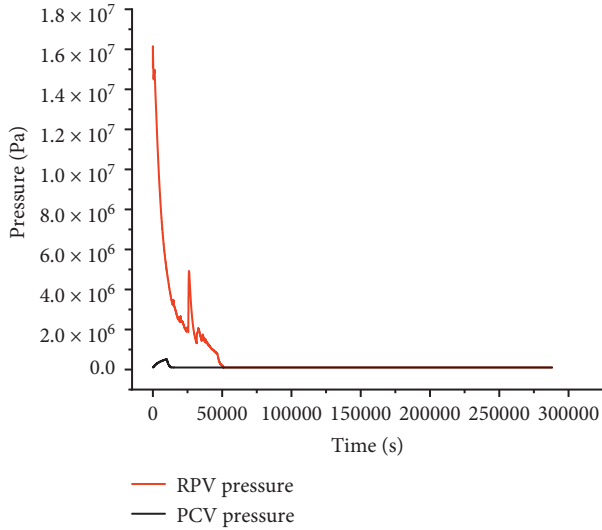Figure 2: Nodalization of the core of the marine reactor.

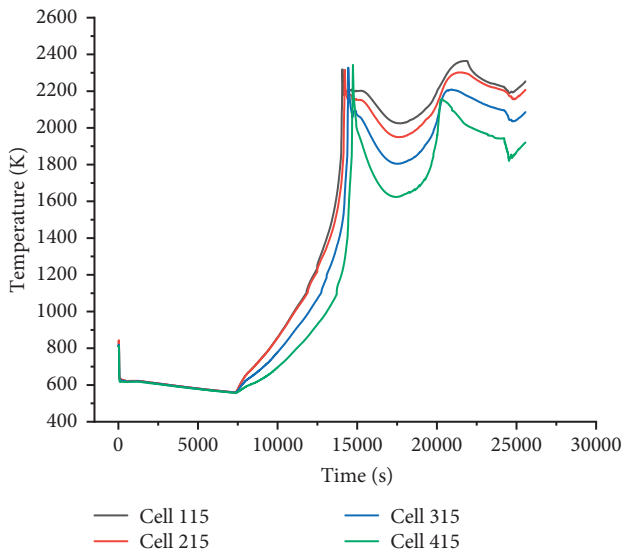FIGURE 3: Pressure in PCV and RPV.



FIGURE 4: The node temperature in the outer layer.

assumed to be in elemental form and therefore to have only radioactive mass (no associated molecular mass). Upon release from fuel, the total class masses are converted to compound form with a corresponding increase in mass from the added nonradioactive material (e.g., the hydroxide mass in CsOH). By default, the release models are used to calculate the release of radionuclides from core fuel material (i.e., $UO_2$) only, which exists in the intact fuel component, in refrozen fuel material or in other components, and in particulate in debris.

Note that, for each core component, the same correlation is used to calculate the release rate for a given class using the individual temperature of that component. That is, the calculation of release of radionuclides from fuel, cladding, canisters, control rods, and particulate debris differs only in the temperature used.

The calculation model of the serious accident analysis program correlates with the fractional release rate in the exponential form [11]:

$$\dot{f} = A \exp(BT) \quad \text{for } T \ge T_i, \qquad (1)$$

where $\dot{f}$ is the release rate (fraction per minute), $A$ and $B$ are empirical coefficients based on experimental data. Different values for $A$ and $B$ are specified for three separate temperature ranges. $T$ is the temperature of the core unit (K) and $T_i$ is the minimum temperature set by the user at the beginning of release, (K).

## 3. Accident Hypothesis and Grouping of Radionuclide

*3.1. Assumptions of Marine Reactor Design Parameters.* The steady-state behavior of the marine reactor severe accident model is an important feature indicating the reliability of the model and the basis of transient accident analysis. According to the design conditions of small-scale marine pressurized water reactors, the key parameters were established to provide the initial conditions for severe accidents. These parameters were in good agreement with corresponding design values demonstrated by a comparative analysis shown in Table 1 [12]. Therefore, this steady-state can be used as the initial condition for the subsequent accident simulation.

*3.2. Assumptions of Accidents.* At the beginning of the accident, it was assumed that SBLOCA with an area of $0.0064 \, \text{m}^2$ occurred in the pressurizer caused by a failure in RVVs. This means that the nuclear reactor malfunctioned at the beginning of the accident. The open pressure for SRVs of PCV was 5 MPa. No operator actions or interventions were considered during the handling of the accident.

According to the information in the output file of the MELCOR code, Table 2 indicates the occurrence sequence of severe accidents [12]. Compared with severe accidents in traditional light-water reactors, some failures in the core support plate and the lower head occurred in the later stage of the accident. It is important to note again that, in the current analysis, operator actions that are beneficial to accident mitigation were not considered.

*3.3. Grouping of Radionuclides.* In a severe accident, the degree of fission products in the reactor core released into the containment, and the environment mainly depends on its physical and chemical properties. The MELCOR divides some elements with similar properties into 16 groups [11] as shown in Table 3 and processed them in groups. Depending on the characteristics of a marine reactor, 13 groups were selected for this study, and 3 groups of elements (boron, water, cement, and no concrete in the reactor pit) were removed.

## 4. Safety Analysis of Marine Reactor

*4.1. Release Analysis of the Hydrogen Source Term.* Combustion and explosion of hydrogen constitute a major threat to the integrity of the containment vessel. Hydrogen

TABLE 1: Key parameters in steady state and design value.

| Key parameters | Designed value | Steady-state value |
|---|---|---|
| Core thermal power (MW) | 330.0 | 330.02 |
| Primary system pressure (MPa) | 12.76 | 12.85 |
| Core inlet temperature (K) | 552.15 | 552.83 |
| Core outlet temperature (K) | 583.15 | 583.42 |
| Core inlet mass flow rate (kg/s) | 1960 | 1977 |
| SG steam pressure (MPa) | 3.5 | 3.501 |
| SG steam temperature (K) | 575.15 | 575.4 |
| SG feedwater temperature (K) | 422.15 | 421.7 |
| Main steam mass flow rate (kg/s) | 140.0 | 140.0 |
| RPV coolant inventory (kg) | 126340.0 | 126346.0 |
| Fuel mass inventory (kg) | 16280.0 | 16280.0 |

TABLE 2: Sequence of severe accident.

| Events | Time (s) |
|---|---|
| SBLOCA, containment pool crack, DHRS failed | 500 |
| Reactor tripped | 500 |
| PCV-SRVs open started | 10204 |
| Active core region actually exposed | 46900 |
| Gap release | 61650 |
| Core bottom dry out | 73095 |
| Core support plate failed | 300358 |
| Lower head breach | 457492 |
| PCV cavity breach | 482958 |
| Running ended | 1000000 |

TABLE 3: Grouping of materials in the MELCOR.

| Class | Name | Representative | Member elements |
|---|---|---|---|
| 1 | Noble gas | Xe | Xe, Kr, Rn, He, Ne, Ar, H, N |
| 2 | Alkali metals | Cs | Cs, Rb, Li, Na, K, Fr, Cu |
| 3 | Alkaline earths | Ba | Ba, Sr, Be, Mg, Ca, Ra, Es, Fm |
| 4 | Halogens | I | I, Br, F, CI, At |
| 5 | Chalcogens | Te | Te, Se, S, O, Po |
| 6 | Platinoids | Ru | Ru, Pd, Rh, Ni, Re, Os, Ir, Pt, Au |
| 7 | Early transition elements | Mo | Mo, Tc, Nb, fe, Cr, Mn, V, co, Ta, W |
| 8 | Tetravalent | Ce | Ce, Zr, Th, Np, Ti, Hf, Pa, Pu, C |
| 9 | Trivalents | La | La, Pm, Sm, Y, Pr, Nd, Al, Sc, Ac, Eu, Gd, Cf, Tb, Dy, Ho, Er, Tm, Yb, Lu, Am, Cm, Bk |
| 10 | Uranium | U | U |
| 11 | More volatile main group | Cd | Cd, Hg, Zn, As, Pb, Sb, TI, Bi |
| 12 | Less volatile main group | Sn | Ga, Ge, Sn, Ag, In |
| 13 | Boron | B | B, Si, P |
| 14 | Water | $H_2O$ | $H_2O$ |
| 15 | Concrete | — | — |
| 16 | Cesium iodide | CsI | CsI, —, — |

in the pressure vessel is mainly produced by zirconium-water reaction. The chemical equation of the zirconium-water reaction is as follows:

$$Zr + 2H_2O \longrightarrow ZrO_2 + 2H_2 + \Delta HR, \qquad (2)$$
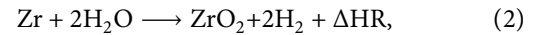
where $\Delta HR$ is the heat per mole generated by zirconium after oxidation.

The time change of hydrogen release in the containment is shown in Figure 5. In the course of the accident, the fuel temperature gradually increased, the fuel rods swelled, and the zircon cladding was oxidized. Hydrogen was produced at around 11,820 s. Zirconium and water reacted slowly, and a small amount of the hydrogen was released during the next 1,500 s. At 46,700 s, the release of hydrogen reached the minimum value of 8.665 kg. At this time, it could be determined that the reactor core was completely exposed. After 46,700 s, the zirconium-water reaction became very violent, and hydrogen production increased rapidly. At the time of 240,250 s, due to the failure in the core support plate, hydrogen release reached the peak value of 248.567 kg. The released hydrogen shared less than 4% of the air volume, so no hydrogen explosion would occur.

*4.2. Research on Radionuclide Release and Migration.* The radioactive fission products such as radioactive iodine, cesium, xenon, and barium will be released from the reactor during a severe accident. This will pose a threat to the lives of the staff and the surrounding public and cause serious pollution to the ecological environment. The personnel in the cabin will be exposed to radiation, and radionuclides will be released into the environment and the ocean. Therefore, three radionuclides having relatively important influences on the radioactive consequences were selected as the research objects. These were the inert gas represented by Xe, the volatile fission products represented by CsI, and the nonvolatile fission products represented by Ba.

*4.2.1. Analysis of Release and Migration of Inert Gases Represented by Radionuclides Xe.* Inert gases such as Xe are chemically stable and do not react with other nuclides. The release and migration behaviors of the radioactive nuclide Xe during the accident were analyzed. The pressure relief valve in the pressure vessel opened, and the reactor core began to be exposed at 10,204 s. The inert gas was mainly released from the reactor core, and the initial release time of radionuclide Xe in the primary circuit system and containment was 12,120 s. The reactor core exposure time was lagged by 1,916 s. Since the inert gas did not deposit on the surface of the thermal components and was insoluble in water, the released inert gas quickly entered the main system pipeline, the containment atmosphere, and the environment through a breach. The release process of radionuclides such as Xe in the primary circuit system, the cavity, and the containment is shown in Figures 6–8.

Xe began to be released in the primary circuit, and the mass of release was 0.298 kg at 12,120 s. Table 2 shows that the full exposure time of the reactor core was 46,900 s, and
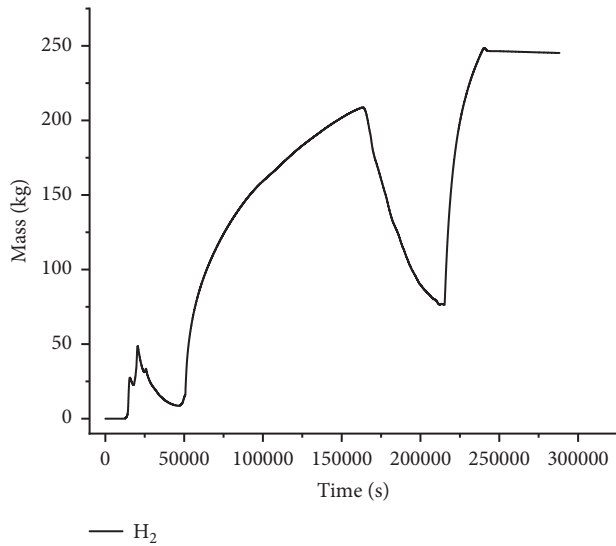
Figure 5: Hydrogen release from containment over time.
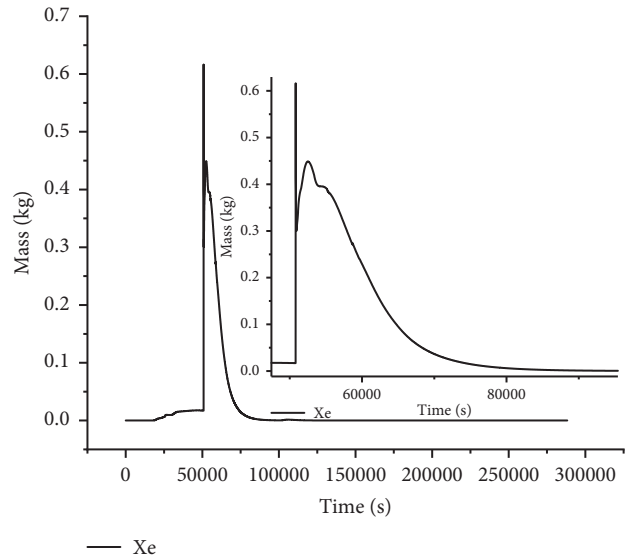


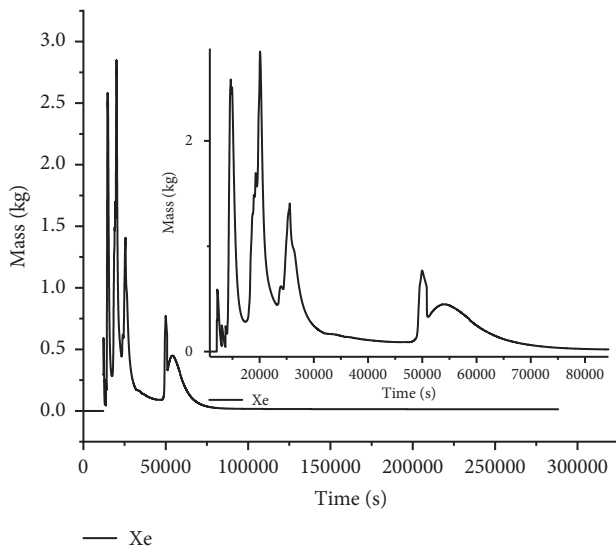Figure 7: Release of Xe in cavity.



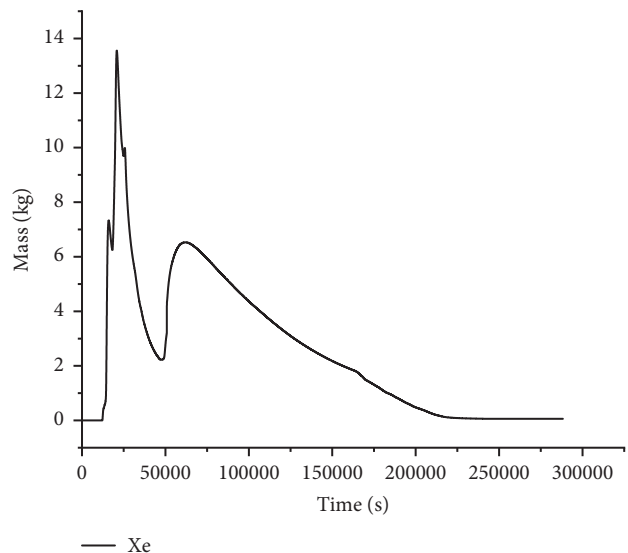Figure 6: Release of Xe in the primary circuit system.



Figure 8: Release of Xe in containment.

Figure 6 shows that the released amount of Xe decreased to the lowest value at 47,410 s. The simulation results showed that the complete core exposure time delay was 510 s. At 12,120 s, Xe was released in the initial containment atmosphere (Figure 8), and the release amount was nearly 0. Xe release decreased to the lowest value, and the reactor core was completely exposed at 47,600 s. Xe began to release in the cavity (Figure 7), and the release amount was very small at the 14,690 s. Because the reactor core was completely exposed, the rupture position was far away from the reactor cavity. The release amount of Xe increased sharply to the peak value of 0.616 kg at 50,820 s and then dropped sharply.

*4.2.2. Analysis of Release and Migration of Volatile Gas Represented by Radionuclide CsI.* The chemical properties of iodine are more active, and it immediately reacts with Cs to form CsI which is easy to volatilize forming aerosols. Almost all the iodine released from the reactor core react with Cs to form CsI [1, 7], and the fraction of the element iodine is extremely small. The release of iodine in the containment is shown in Figure 9, and the comparison between iodine and CsI released in the containment is shown in Figure 10.

The release process of CsI in the primary circuit system and the cavity is shown in Figures 11 and 12. The CsI began to release in the primary circuit system, and the reactor core began to be exposed at 12,120 s. The release rate of CsI in the primary circuit system was high, and the mass of release was large with the peak value of 0.243 kg, until the core was completely exposed and the release dropped to the minimum value (nearly 0).

The total mass of CsI released in the cavity (Figure 12) was much less with the maximum value of 0.0166 kg only.
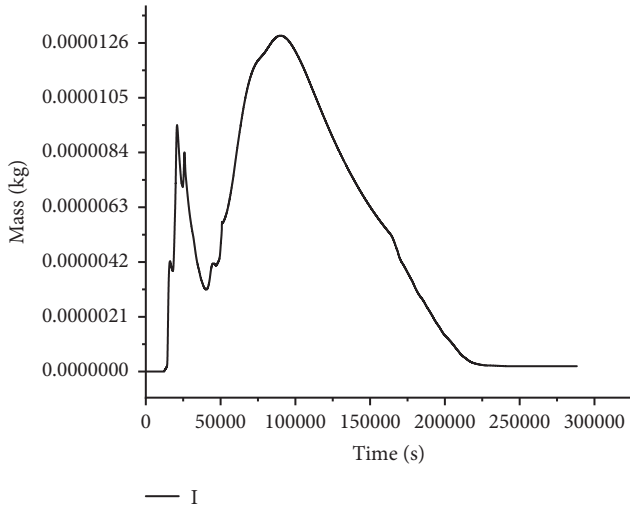
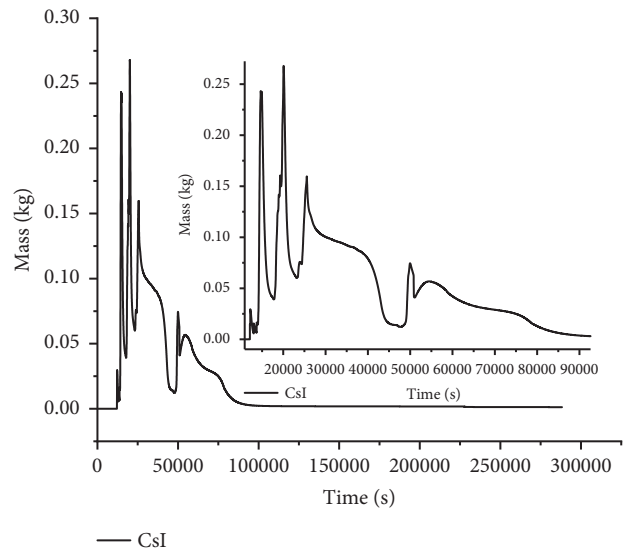Figure 9: Release of I in the containment.



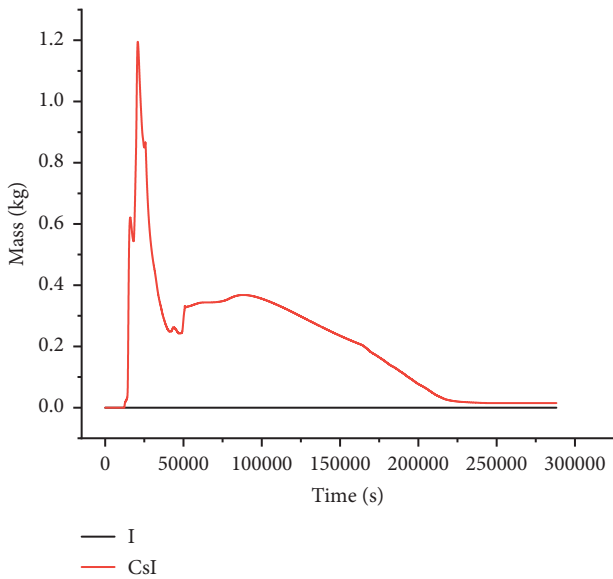Figure 11: Release of CsI in the primary circuit system.



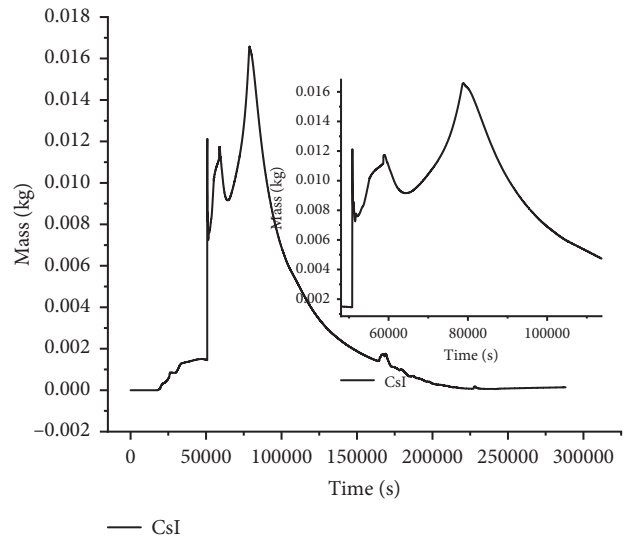Figure 10: Comparison of I and CsI.



Figure 12: Release of CsI in the cavity.

The release of CsI in the containment (Figure 10) sharply increased to the maximum value of 1.195 kg at first and then sharply decreased to the minimum value. The release showed a horizontal curve and remained at about 0.01 kg when the accident sequence was 226,500 s. The main reason was that most of the CsI released into the containment were dissolved in the containment pool in the ionic state. A small part existed in the containment atmosphere in the form of aerosols, and minimal part was adsorbed on the surfaces of the thermal components in the containment. CsI aerosols in the containment atmosphere were gradually settled into the pool.

*4.2.3. Analysis of Release and Migration of Nonvolatile Gases Represented by Radionuclide Ba.* Ba is a representative element of nonvolatile radionuclides. According to

MELCOR's calculation results, the nonvolatile radionuclides are the release amount of Ba. Radionuclide Ba was selected as the representative of nonvolatile fission products to analyze its release and migration behavior. Ba was released in the reactor core during the core damage process at first. The release processes of radionuclide Ba in the primary circuit system, the containment, and the cavity during the accident process are shown in Figures 13–15.

Ba began to be released in the primary circuit system at 12,120 s and reached the maximum value of 0.434 kg at 58,660 s (Figure 13). Then, the release of Ba decreased continuously until dropped to 0.01 kg at 121,390 s. Afterward, the mass of release Ba was extremely small and remained unchanged. Ba began to be released in the containment at 12,120 s (Figure 14). Its released amount increased rapidly and reached the maximum value of 1.48 kg and dropped at a similar rate until the reactor core was
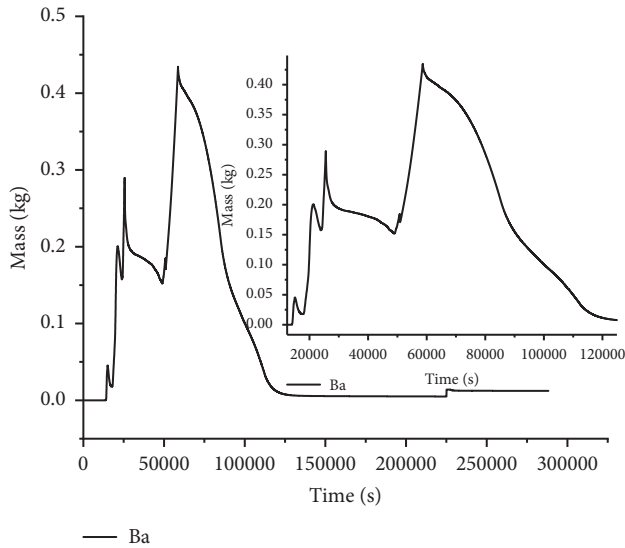
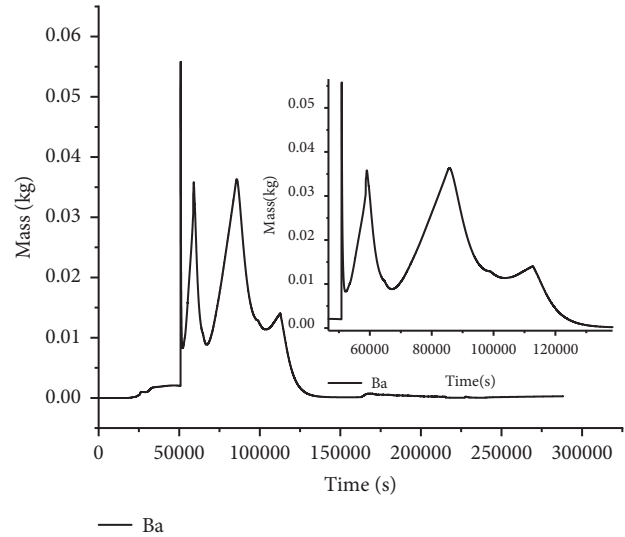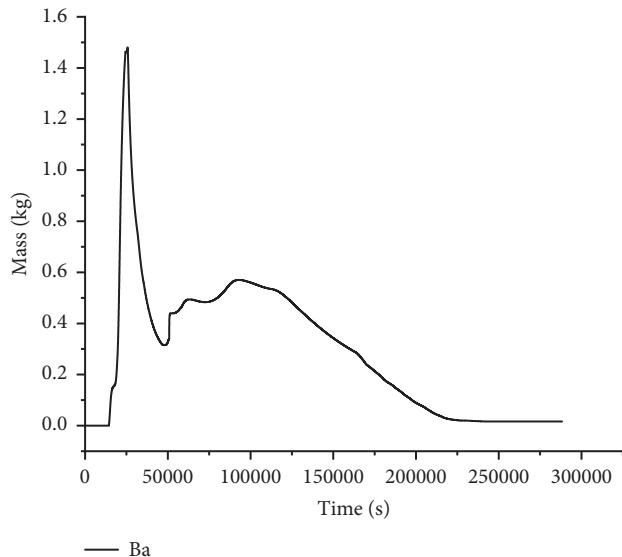FIGURE 13: Release of Ba in the primary circuit system.



FIGURE 14: Release of Ba in the containment.

completely exposed at 48,000 s. Finally, it dropped to the lowest value of 0.31 kg. Due to the failure in the core support plate, the release of radionuclides increased to the peak value of 0.57 kg at 93,420 s and then slowly decreased. Compared with the primary circuit system and the containment, the released amount of Ba in the cavity (Figure 15) was relatively small and the maximum value was 0.0558 kg.

### 4.2.4. Analysis of Release of Xe, CsI, and Ba at Different Locations

*(1) Comparative Analysis of the Releases of Xe, CsI, and Ba in the Primary Circuit System.* The releases of Xe, CsI, and Ba in the primary circuit system (Figures 6, 11 and 13) were



FIGURE 15: Release of Ba in the cavity.

compared and analyzed. These three radionuclides started to be released at the same time in the primary circuit system. Xe and CsI had similar release trends with the accident sequence. Before the reactor core was completely exposed, the releases of Xe and CsI showed a trend of 5 wave peaks, and troughs for the core nodes were divided into 5 radial rings. Assuming that the core was completely exposed at 46,900 s, the wave trough times of the 5th segment released by Xe and CsI in the primary circuit system were 47,410 s and 47,730 s, respectively. However, the release trend of Ba in the primary circuit system was different from those of Xe and CsI because most of Ba was deposited or settled on the surfaces of thermal components in the form of particles, while a small part of Ba was in the water and the minimal part of it was in the form of aerosol in the air.

*(2) Comparative Analysis of the Releases of Xe, CsI, and Ba in the Containment.* A comparative analysis of the releases of Xe, CsI, and Ba in the containment was performed (Figures 8, 10, and 14). The curves showing the time change of the releases of Xe, CsI, and Ba were similar. These three radionuclides showed the same release trends in the containment, and the initial release time was 12,120 s. But the release of Xe was much higher than that of CsI. Figures 8 and 10 show that the releases of Xe and CsI increased rapidly, and the times when they reached the first peak were 15,980 s and 16,030 s, respectively. The peak value of the release at those timing was 7.329 kg and 0.621 kg, respectively. Subsequently, the release continued to increase rapidly reaching the second peak values of 13.557 kg and 1.195 kg at 20,850 s and 20,860, respectively. Figure 14 shows that the release of Ba increased rapidly with time and reached its maximum value at 25,680 s. This release gradually decreased after reaching the maximum value with the continuous release of fission products from the molten core. After 220,000 s, the releases of the three radionuclides reached the minimum value, and the release tended to become the horizontal curves.
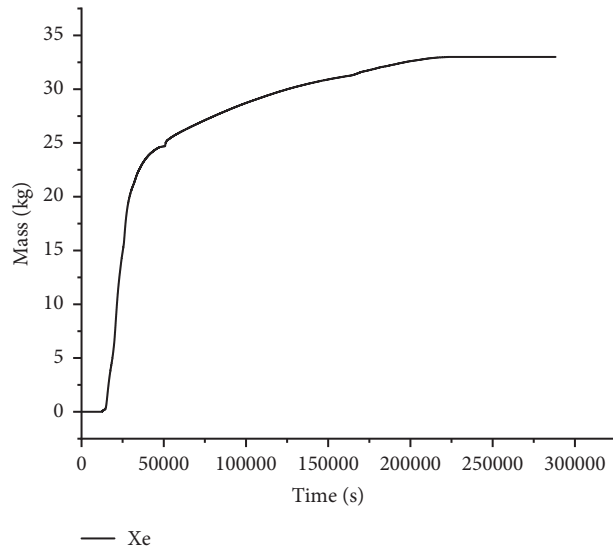
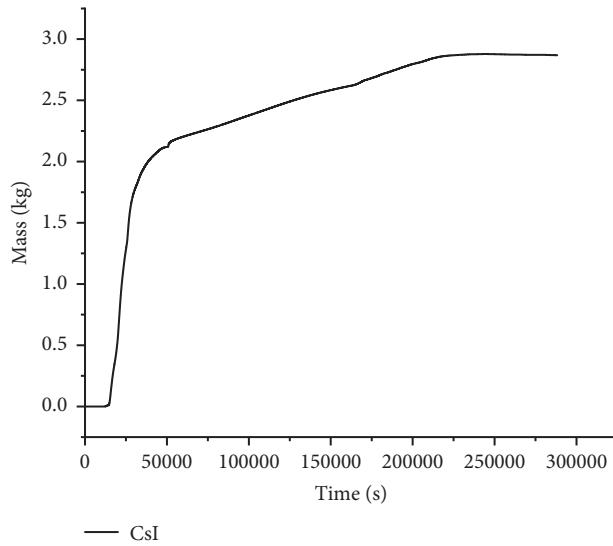Figure 16: Release of Xe in the environment.
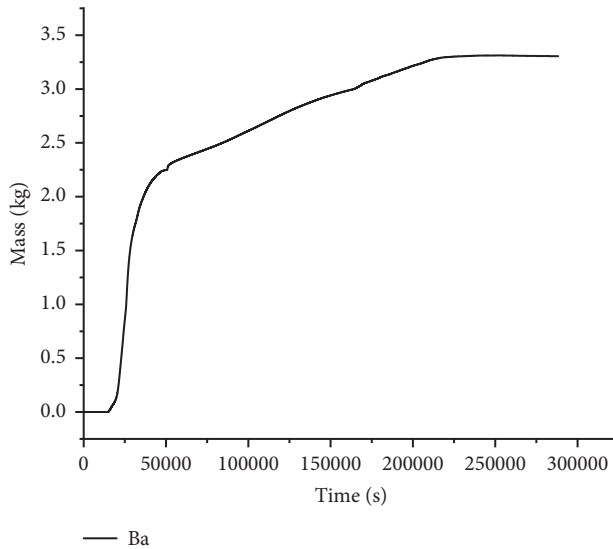


Figure 17: Release of CsI in the environment.



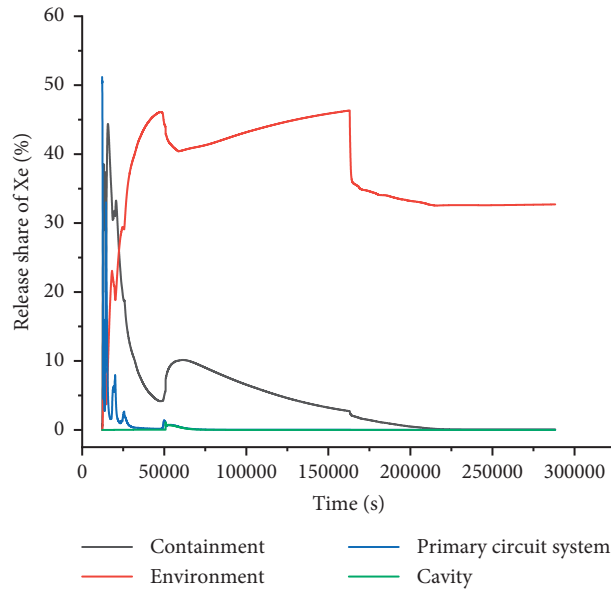Figure 18: Release of Ba in the environment.

FIGURE 19: Distribution of Xe in different position.
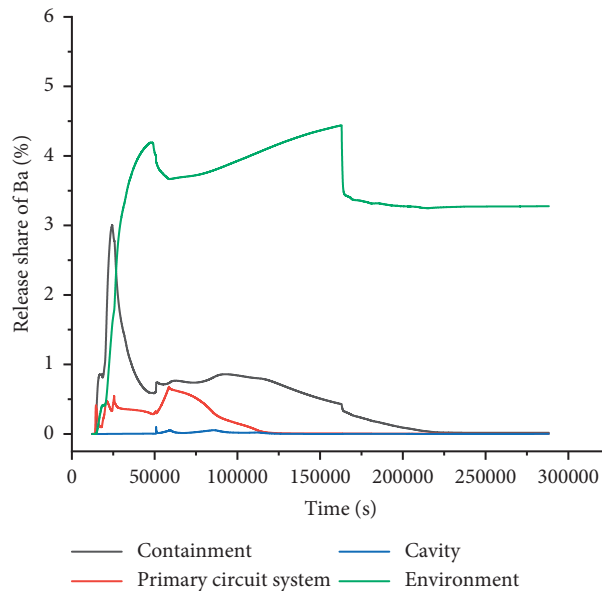


FIGURE 20: Distribution of Ba in different position.

*(3) Comparative Analysis of the Releases of Xe, CsI, and Ba to the Environment.* A comparative analysis of the releases of Xe, CsI, and Ba to the environment was performed (Figures 16–18). The three curves show the same trend, but the release of Xe to the environment was higher than those of CsI and Ba. The releases of these three radionuclides to the environment started at the same time and increased sharply. The three radionuclides simultaneously passed through an inflection point at 50,810 s because the reactor core was completely exposed. The releases of the radionuclides continued to increase slowly because the calculation time was long enough. The releases of the three radionuclides to the environment reached the maximum value at 222,920 s

and came into the horizontal transition state afterward. Almost all of the three radionuclides were released into the environment.

*4.3. Analysis of Release Shares of Xe, CsI, and Ba.* The release shares of Xe, Ba, and Csl in the containment, the reactor cavity, the primary circuit system, and the environment are shown in Figures 19–21, respectively. The results show that the release shares of Xe, CsI, and Ba under the same conditions were similar. At the end of the calculation, the release shares of Xe in the primary circuit system, the containment, and the environment were 0.013%, 0.06% and 32.71%,

FIGURE 21: Distribution of CsI in different position.

TABLE 4: Distribution of radionuclide release share of fully exposed core.
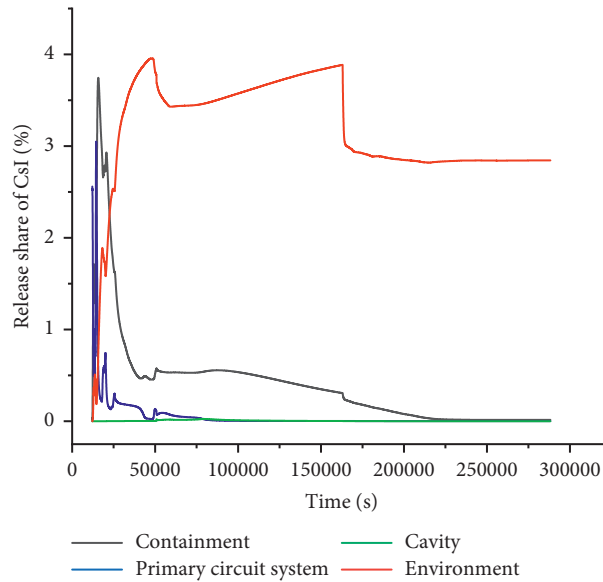
| Radionuclide | Share (%) | | | |
| --- | --- | --- | --- | --- |
| | Containment | Primary circuit system | Cavity | Environment |
| Xe | 4.164 | 0.168 | 1.075 | 43.964 |
| Ba | 0.599 | 0.678 | 0.0296 | 4.005 |
| CsI | 0.454 | 0.0229 | 0.0036 | 3.7 |

TABLE 5: Distribution of maximum radionuclide release share.

| Radionuclide | Share (%) | | | |
| --- | --- | --- | --- | --- |
| | Containment | Primary circuit system | Cavity | Environment |
| Xe | 44.391 | 51.195 | 1.075 | 46.331 |
| Ba | 3.003 | 0.678 | 0.0966 | 4.44 |
| CsI | 3.745 | 3.048 | 0.0252 | 3.957 |

respectively; those of Ba were 0.016%, 0.0032%, and 3.28%, respectively; and those of CsI were 0.0145%, 0.0012%, and 2.845%, respectively. However, the release shares of these three radionuclides in the cavity were almost 0.

To provide useful data for the dose assessment in the cabin during a severe accident, the release share distributions of the three radionuclides in the containment, the cavity, the primary circuit system, and the environment were analyzed for the timing of the complete exposure of the reactor core. The results are shown in Table 4. The distributions of the maximum release shares of the three radionuclides during a severe accident were also analyzed, and the results are shown in Table 5.

Table 5 represents the maximum release share of radionuclides at different locations with the progress of a severe accident. The maximum release share of Xe in the containment at T1 is 44.391%, the maximum release share of Xe in the primary circuit system at T2 is 51.195%, the maximum release share of Xe in the cavity at T3 is 1.075%, and the maximum release share of Xe in the reactor cavity at T4 is 46.331%. T1, T2, T3, and T4 represent different times.

The small break loss of coolant accident in a marine reactor directly resulted in the radioactive hazards to the atmospheric environment and the people inside the ship. The radiation effect in the adjacent cabin was very serious. The staff in this environment absorbed more systemic dose and thyroid dose, which caused serious harm to the human body. However, the radiation consequences in other cabins were less, and the radiation dose less affected the workers' health.

## 5. Conclusion

Based on the analyses on the release, migration, and retention characteristics and the distribution of radionuclides induced by SBLOCA in a marine reactor, the following conclusions are drawn:

(1) The analysis results of hydrogen source term released during a severe accident showed that the hydrogen release reached a peak value of 248.567 kg at 240,250 s due to the failure in the core support plate. But the hydrogen release volume accounted for less than 4% of the air volume, and there would be no possibility of the occurrence of hydrogen explosion accidents.

(2) The releases of Xe, CsI, and Ba in the primary circuit system, the containment, the reactor cavity, and the environment showed similar trends. The release of Xe in the primary circuit system was analyzed using the MELCOR. The results showed that complete core exposure was lagged by 510 s, and the initial release time of the radionuclides was lagged by 1,916 s.

(3) The release shares of Xe, CsI, and Ba in the primary circuit system, the containment, the reactor cavity, and the environment were similar. When the calculation time was long enough, the release shares of these three radionuclides in the environment were the largest, followed by the containment, while the release shares in the primary circuit system and the reactor cavity were almost 0.

(4) The releases of radionuclides reached the minimum values when the core was completely exposed. At that timing, the releases of Xe in the primary circuit system and the containment vessel were 0.0895 kg and 2.22252 kg, respectively; those of Ba were 0.1521 kg and 0.31493 kg, respectively; and those of CsI were 0.0122 kg and 0.24234 kg, respectively.

(5) At the end of the calculation, the release shares of the Xe in the primary circuit system, the containment, and the environment were 0.013%, 0.06%, and 32.71%, respectively; those of Ba were 0.013%, 0.06%, and 32.71%, respectively; and those of CsI were 0.0145%, 0.0012%, and 2.845%, respectively.

## Data Availability

The data used to support the findings of this study are included within the article.

## Conflicts of Interest

The authors declare that they have no conflicts of interest.

## References

[1] Y. Zhang, F. Zhang, X. Zhao, and Y. Zheng, "Source term analysis in severe accident induced by large break loss of coolant accident coincident with ship blackout for ship reactor," *Atomic Energy Science and Technology*, vol. 47, no. 9, pp. 1565–1571, 2013.

[2] B. Wu, M. Jia, and J. Gong, "Character and calculation method of nuclear accident source term of marine reactor," *Journal of Naval University of Engineering*, vol. 15, no. 5, pp. 87–90, 2003.

[3] X. Lyu, S. Liu, K. Ji, Y. Feng, S. Wang, and Z. Huang, "Research on hydrogen risk and hydrogen control system in marine nuclear reactor," *Annals of Nuclear Energy*, vol. 141, p. 107373, 2020.

[4] K. Ouyang, W. Chen, and Z. He, "Analysis of the radioactive atmospheric dispersion induced by ship nuclear power plant severe accident," *Annals of Nuclear Energy*, vol. 127, pp. 395–399, 2019.

[5] W. Wang, L. S. Chen, F. Zhan, and H. P. Liu, "Radioactive analysis on accident of SG-tube rupture coupled with whole ship blackout," *Atomic Energy Science and Technology*, vol. 49, no. 5, pp. 871–876, 2015.

[6] W. Wang, L. Chen, F. Zhan, and Q. Cai, "Source term analysis on blackout accident of marine reactor," *Atomic Energy Science and Technology*, vol. 48, no. 6, pp. 1038–1043, 2014.

[7] F. Zhan, F. Zhan, W. Wang, and L. Yu, "Analysis of accident due to interruption of power supply and safety valve failure," *Journal of Naval University of Engineering*, vol. 26, no. 6, pp. 37–41, 2014.

[8] R. M. Summers, *MELCOR 1.8.1 Computer Code Manual Volume 1: Primer and Package Users Guides, MELCOR Primer*, Sandia National Laboratories, Albuquerque, USA, 1991.

[9] L. E. Poier Baez, J. E. Nunez Mac Leod, and J. H. Baron, "Severe accident improvements for Carem-25 to arrest reactor vessel meltdown sequences," in *Proceedings of the 10th International Conference on Nuclear Engineering*, Arlington, VA, USA, April 2001.

[10] J. C. Kim, G. H. Jung, J. S. Cho, and H. C. Kim, "Severe accident analyses for SMART using MELCOR 1. 8.6 code," in *Proceedings of the KNS autumn meeting*, Daejeon, Republic of Korea, October 2011.

[11] R. M. Summers, *MELCOR Computer Code manuals, Volume 1: RadioNuclide (RN) Package Users' guide*, Sandia National Laboratories, Albuquerque, USA, 2000.

[12] L. Li, T. W. Kim, Y. Zhang et al., "MELCOR severe accident analysis for a natural circulation small modular reactor," *Progress in Nuclear Energy*, vol. 100, pp. 197–208, 2017.

*Research Article*

# Source Term Estimation under the SBLOCA-Induced Severe Accident Condition in the SMART

**Jaehyun Ham** [ID], **Sang Ho Kim, Sung Il Kim, Byeonghee Lee, Jong-Hwa Park, Rae-Joon Park, and Jaehoon Jung**

*Korea Atomic Energy Research Institute, 1045 Daedeok-daero, Yuseong-Gu, Daejeon 34039, Republic of Korea*

Correspondence should be addressed to Jaehyun Ham; jhham@kaeri.re.kr

The SMART is a system-integrated modular reactor in which a nuclear steam supply system with a thermal power of 365 MW is contained inside of the reactor vessel. Although the probability is very low, the reactor core can be damaged during a small break loss-of-coolant accident when both the passive safety injection system and the passive residual heat removal system are completely unavailable. In this work, a total of five cases were analyzed considering the reactor vessel condition and the availability of the radioactivity removal tanks and the ancillary containment spray system as containment condition variables using MELCOR code. It was estimated that there is no containment failure based on pressure, hydrogen mole fraction, and ablation depth, so that the release fractions of the 12 classes of fission products in MELCOR were evaluated considering design leak only for all cases. The overall source term of the case in which the integrity of the reactor vessel is maintained by the early initiation of the cavity flooding system was similar to that of the reactor vessel failure case. While the release fraction of cesium to the environment was analyzed to increase when there is no water in the radioactivity removal tanks, the fraction is small enough at which the radioactivity of the released cesium-137 remains well below 100 TBq, a regulatory limit. Moreover, it was found that the source term can be cut in half if the ancillary containment spray system is available. The results of this study verify the safety performance of the SMART under the small break loss-of-coolant severe accident condition with respect to the source term of interest.

## 1. Introduction

Increasing interest and demand for small modular reactors is driving related practical achievements such as design completion, design certification, and construction. Various types of such reactors have been proposed globally, typically classified according to the type of coolant. Among them, light water-cooled reactors are at the forefront of technology, like conventional large nuclear power plants.

CAREM-25 (Central Argentina de Elementos Modulares) was designed to deliver 27 MW of electrical power with minimum operator feedback control [1]. A CAREM-25 prototype is currently being built by CNEA (Argentine National Atomic Energy Commission) at a site next to the Atucha nuclear power station in Lima, Argentina [2]. China has developed various types of small modular reactors such as the ACPR (Advanced Customer-friendly Practicable

Reliable) series including the ACPR100 for onshore 140 MW plants and the ACPR50S for offshore 60 MW plants of electrical power [2]. The barge-mounted KLT-40S reactor developed by the Russian Federation has already received design approval from the Russian regulatory authority. NuScale, developed by NuScale Power, LLC, is a modular plant designed in the US with 12 reactor modules in a single plant [3] and 160 MW of thermal power per module. The NuScale plant received design certification approval from the US Nuclear Regulatory Commission in August 2020. As a first-of-its-kind project, the first NuScale plant is currently under construction in eastern Idaho and is scheduled to come online in 2029.

In the Republic of Korea, some plant models based on the SMART (System-integrated Modular Advanced Reactor) design have been developed. The standard design approval for the first SMART, with a thermal power of

330 MW, was issued by the Nuclear Safety and Security Commission in Korea in July 2012, representing the first license for an integral reactor in the world. Since then, the 365 MW SMART has been developed with fully passive safety systems, with licensing in preparation.

In the reactor vessel (RV) of the SMART, eight helical steam generators and four reactor coolant pumps are integrated and installed, as shown in Figure 1(a). The thermal energy of the superheated steam generated in the core is transferred to the water in the secondary circuit through once-through steam generator tubes. The canned-motor type reactor coolant pumps are horizontally mounted. On the RV, there is no penetration tube or nozzle larger than 2 in. The reactor containment and auxiliary buildings are combined into one arched roof rectangular containment building, as shown in Figure 1(b). In Section 2, the designs and operations of the systems installed as part of the reactor coolant system and containment are explained in more detail with the modeled control volumes and junctions.

The possibility of a large break loss-of-coolant accident (LOCA) like in general pressurized water reactors is fundamentally excluded because, in the SMART, the main components are embedded in the RV without pipe lines. In addition, the reactor includes several design features to enhance safety such as the passive safety injection system (PSIS) and the passive residual heat removal system (PRHRS), both passive features with which the reactor core and the containment can be protected even under station blackout accident conditions.

While the large break LOCA can be excluded owing to the RV design, there is still a possibility for a small break LOCA (SBLOCA) from a break at the PSIS pipes. Among the possible initiating events, SBLOCA is one of the most conservative accidents (other than containment bypass accidents) in the SMART because the whole volume of gas in the RV can be released following this accident. If the PRHRS and the PSIS are completely unavailable during a SBLOCA, the reactor core can be damaged [4]. Even though this scenario is not likely to occur, it is important to estimate the source terms under this condition to verify safety performance. In particular, the release of cesium (Cs) must be analyzed because of the regulatory rule dictating that the sum of the accident frequencies that can cause a release of Cs-137 exceeding 100 TBq should be less than $1.0E - 6$/ry [5].

To estimate source terms in severe accident conditions, integral codes such as MELCOR (Methods for Estimation of Leakages and Consequences Of Releases) or MAAP (Modular Accident Analysis Program) can be used for analysis [6]. Among these, MELCOR is a fully integrated, engineering-level computer code with a modeling capability of the severe accident progression in light-water reactor nuclear power plants. This code is being developed at Sandia National Laboratories for the US Nuclear Regulatory Commission as a second-generation plant risk assessment tool, as is the successor to the source term code package. MELCOR treats a broad spectrum of severe accident phenomena in pressurized water reactors in a unified framework and also includes the estimation of severe accident source terms [7, 8].

In this study, source term estimation in a severe accident condition induced by a SBLOCA in the SMART was performed using MELCOR code version 2.2. The status of the containment according to the RV condition and the availabilities of the radioactivity removal tanks (RRTs) and the ancillary containment spray system (ACSS) were estimated based on the resulting pressure, hydrogen mole fraction, and ablation depth. As a final result, the release fractions of fission products to the environment were obtained for the source term.

## 2. Analysis Method

*2.1. Source Term Estimation.* The fission product analysis model in MELCOR, the RadioNuclide (RN) package, can calculate the release and transport behavior of fission product vapors and aerosols. This fission product model operates on the basis of material classes, which are groups of elements that have similar chemical properties such as volatility. Release of fission product classes can occur via fuel-cladding gaps following the exceedance of the cladding failure temperature [9]. In this analysis, it was assumed that the cladding ruptures at a surface temperature of 1173 K. When the cladding fails, gap release of fission products to the channel starts. CORSOR-M with the surface to volume ratio option was selected to simulate the amount of fission product release from the damaged core.

The pool scrubbing models, adapted from SPARC90 (Suppression Pool Aerosol Removal Code), include the effects of steam condensation at the pool entrance and aerosol deposition by Brownian diffusion, gravitational settling, and inertial impaction, also subjected to evaporative forces, for the rising bubbles [10]. To simulate the pool scrubbing phenomena in spargers, which are located in the in-containment refueling water storage tanks (IRWSTs) and RRTs, the pool scrubbing model in MELCOR was applied following design data.

The calculation of aerosol agglomeration and deposition processes is based on MAEROS (Multicomponent AERO-Sol), a multisectional and multicomponent aerosol dynamics code that evaluates the size distribution of each type of aerosol mass, or component, as a function of time [11]. To calculate aerosol transport, removal, and release, all of the fission product classes were classified into three components: water, water-soluble particles such as cesium hydroxide (CsOH) and cesium iodide (CsI), and water-insoluble particles. The hygroscopic effect was considered to account for particle growth by water vapor absorption for water-soluble aerosols.

Thermohydraulic and corium conditions of the containment were calculated to determine the break area based on the pressure, hydrogen mole fraction, and ablation depth by molten core-concrete interaction (MCCI) under various containment conditions from the MELCOR analysis results. The rupture area to estimate the amount of released radionuclides to environment was determined for cases in which the containment can be damaged by overpressure or hydrogen burn. The possibility of containment failure was

(a)



ADS: automatic depressurization system
CCWS: component cooling water system
CMT: core makeup tank
CPRSS: containment pressure and radioactivity suppression system
ECT: emergency cooldown tank
ERVC: ex-reactor vessel cooling
HEX: heat exchanger
IRWST: in-containment refueling water storage tank
PMT: PRHRS makeup tank
PRHRS: passive residual heat removal system

PSIS: passive safety injection system
PSV: pressurizer safety valve
PZR: pressurizer
RCP: reactor coolant pump
RCS: reactor coolant system
RRT: radioactive material removal tank
SC: shutdown cooling function
SG: steam generator
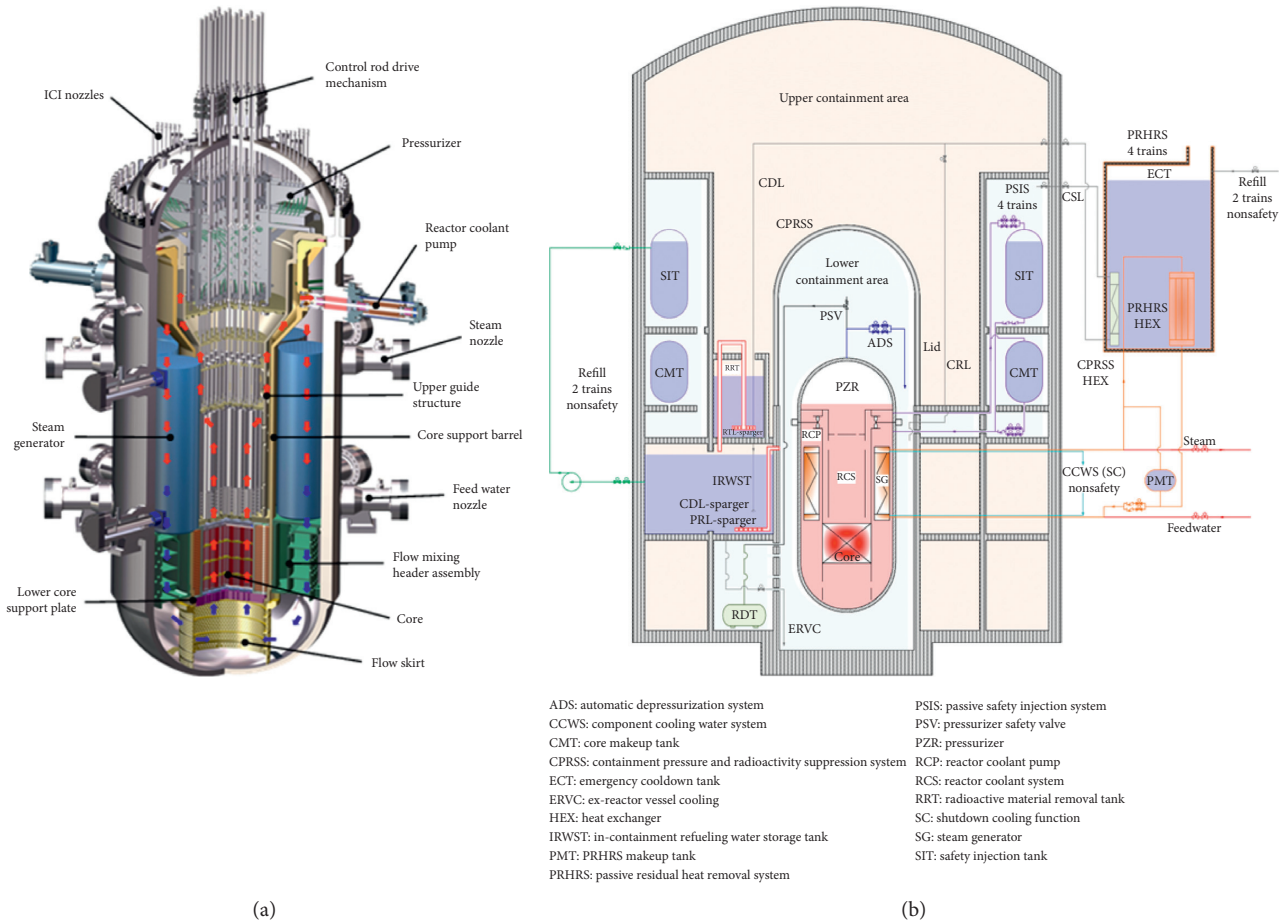SIT: safety injection tank

(b)

FIGURE 1: Schematics of the SMART: (a) reactor vessel and (b) containment.

assumed when the containment pressure exceeded the design pressure or the hydrogen mole fraction reached 10%. For a potential hydrogen burn, it was also checked whether the steam and oxygen mole fractions were sufficient to generate a burn when the hydrogen mole fraction exceeded the critical value. If the RV fails, MCCI was assumed to occur after the molten corium releases into the cavity. In this analysis, the possibility for containment failure was considered via basemat failure when the axial ablation depth exceeds 3 ft.

In cases with no possibility for containment failure, the source term was estimated from the containment natural leak considering design data. The design leak rate from the containment was modeled based on a leak rate of 0.1 volume % per day. This rate corresponds to a break area of about $1.0E - 6 \, \mathrm{m}^2$ from the containment to the environment. The source term is indicated as the release fraction of the 12 fission product classes based on their initial inventories in the SMART. It is assumed that all released iodine (I) gases from the fuel combined to form CsI aerosol following previous studies [12, 13]. The Cs release fraction was highlighted among all fission products to confirm whether the radioactivity of Cs-137 exceeds 100 TBq or not. Source term estimation was performed for 72 h following the occurrence of the initiating event.

*2.2. SMART Core Model.* The SMART was designed as an integral reactor meaning that the steam generators, reactor coolant pumps, and pressurizer are installed in the RV. For MELCOR analysis, control volumes for the RV were constructed as shown in Figure 2(a). The coolant heated in the core region (CV170) flows to the steam generator (CV330–CV339) through the reactor coolant pump (CV211-CV212). After cooling in the steam generator, the coolant goes back to the core region through the lower plenum (CV150). In the RV, the pressurizer (CV500) and the core bypass region (CV180) are located at the top and near the core region, respectively. In the MELCOR analysis, the core model was composed of a total of 16 axial levels and 5 rings, as shown in Figure 2(b). The model was arranged to the core region (CV170) and the lower plenum (CV150) of the RV control volumes. Among the 16 axial levels, a total of 10 axial levels (#6 to #15) contain active fuel with 5 rings. Axial level #5 simulates the core support plate, and axial level #16 is the upper plenum region. Each axial level of the active fuel contains about 1.6 tons of uranium dioxide, about 0.3 tons of zircaloy, about 0.03 tons of steel, and about 0.07 tons of control poison. More than about 14 tons of steel is contained in the lower plenum including the core support plate. In summary, about 16 tons of uranium dioxide, about 4 tons of zircaloy, about 15 tons of steel, and 0.7 tons of
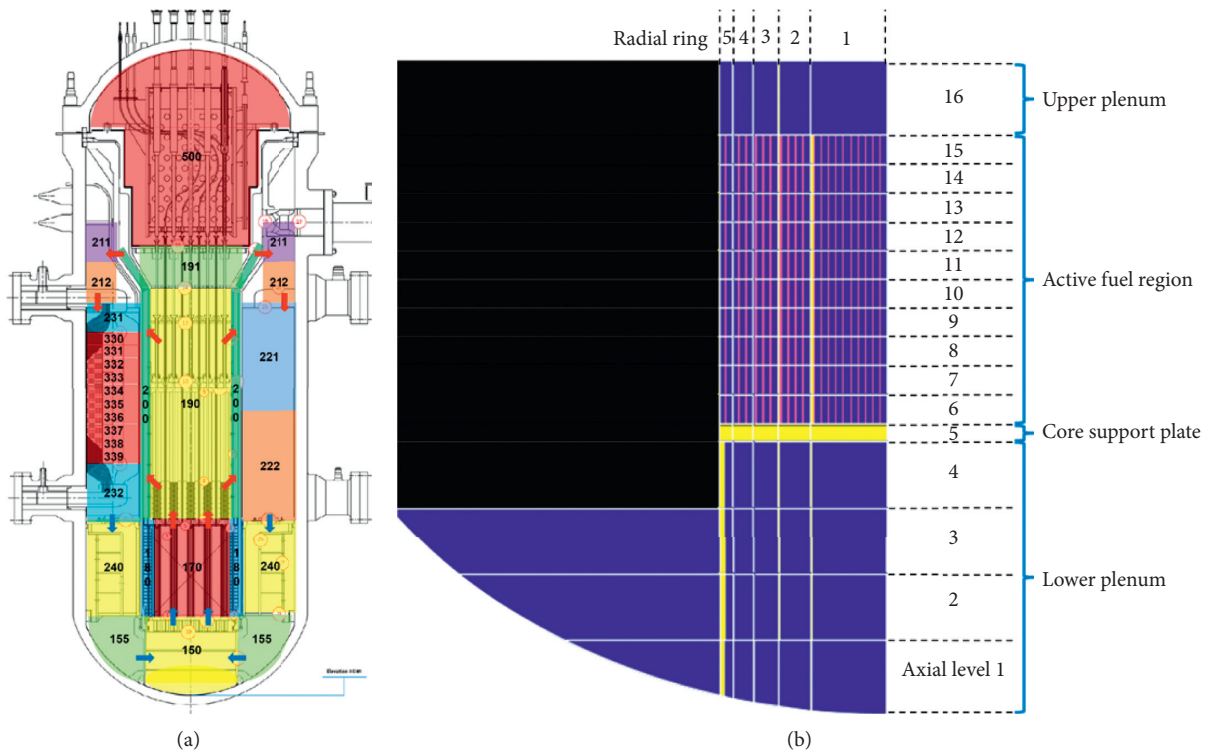
Figure 2: MELCOR nodalization for SMART: (a) reactor vessel and (b) core.

control poison, in total about 36 tons, are contained in the core model for MELCOR analysis. In order to accurately calculate lower head failure, the lower head was divided into 10 segments considering radial and axial nodalization of the fuel. The lower head wall consists of five nodes, with the temperature of the structures and the pressures determining vessel failure.

*2.3. SMART Containment Model.* The containment of the SMART consists of two sections: a lower containment area (LCA) and an upper containment area (UCA). For MEL-COR analysis, the LCA was classified into several control volumes such as upper and lower annulus, cavity, core make-up tank room, and safety injection tank (SIT) room, as shown in Figure 3(a). The UCA is divided into three bulk volumes and a refueling pool. The total volumes of the LCA and the UCA are about 10,000 m$^3$ and 50,000 m$^3$, respectively. In the MELCOR analysis, the initial pressure and temperature of the containment control volumes were assumed as atmospheric pressure and 312 K, respectively.

The LCA is connected to the UCA through the containment pressure and radioactivity suppression system (CPRSS) that envelops the RV. This system consists of (i) four water tanks, namely, two IRWSTs and two RRTs, each of which has a different volume, and (ii) flow paths for water and gas. The water volumes of IRWST1 and IRWST2 are, respectively, about 1,200 m$^3$ and 2,500 m$^3$, and these two tanks are connected via pipelines at the bottom, whereas the two RRTs are not connected. RRT1 and RRT2, respectively, contain water volumes of about 160 m$^3$ and 330 m$^3$. Half of

the RRT pool surface is open to the UCA. The tanks (IRWST1–RRT1 and IRWST2–RRT2) are connected by reversed U-shaped pipelines without valves. In the MELCOR analysis, the initial water temperature of the IRWST and the RRT was conservatively assumed as 322 K.

Likewise, the flow paths connecting the LCA and the IRWSTs are always open; these flow paths are indicated as green lines in Figure 3(a). The CPRSS can maintain UCA pressure below LCA pressure because steam condenses during transportation. As stated in the previous section, aerosol and fission product vapor can be removed by scrubbing within the IRWST and the RRT.

If the pressure in the SIT room located at the top of the LCA exceeds 1.6 bar, operators open the flow paths to transport excessive steam to the IRWSTs through a heat exchanger in an emergency cool-down tank until the core exit temperature meets the entry condition of severe accident management guidance (SAMG); these flow paths are indicated as purple lines in Figure 3(a). Safety relief valves and an automatic depressurization system (ADS) are installed on the upper head of the pressurizer. The safety relief valve is a passive safety valve that prevents the RV from high pressure failure by releasing steam to the cavity when the pressure in the pressurizer exceeds 170 bar.

After SAMG entry, it was assumed that operators open the flow paths connecting the SIT room and the RRT and initiate the ADS, which is an active system to depressurize the RV by releasing gas to the RRT; these flow paths are indicated as red lines in Figure 3(a). The SAMG entry condition was assumed to be satisfied when the core exit gas temperature exceeds 923 K. The operator action time was
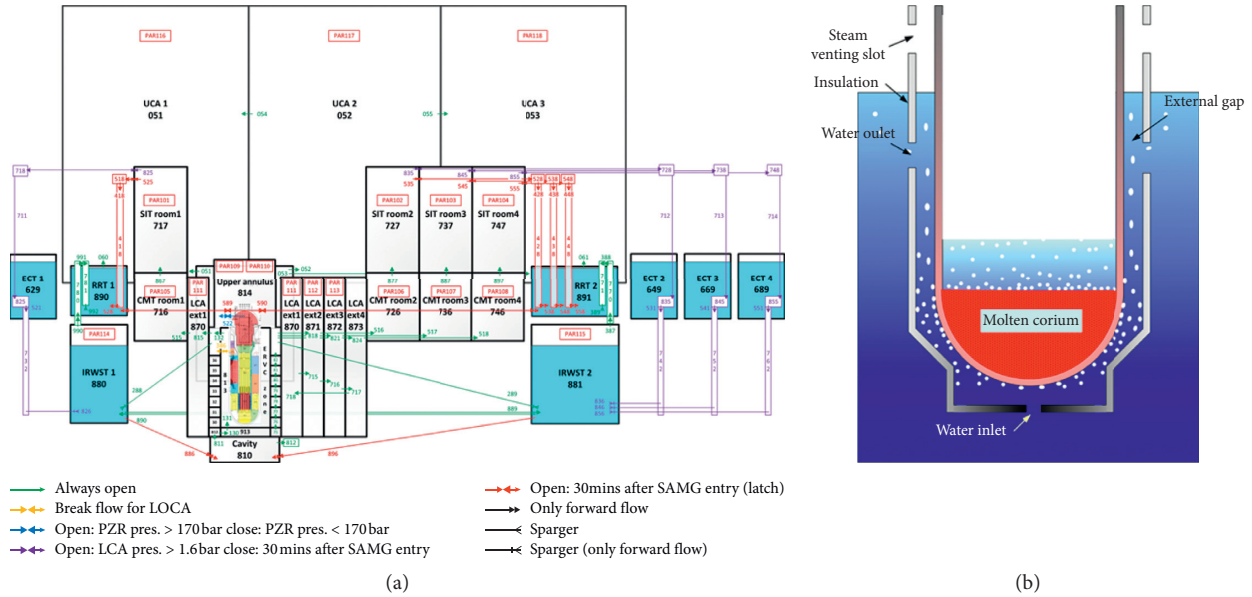
Figure 3: (a) MELCOR nodalization for SMART containment and (b) conceptual view of ex-reactor vessel cooling.

assumed as 30 min for initiating the ADS and opening the flow path connecting the SIT room and the RRT. Passive autocatalytic recombiners (PARs) are installed to prevent hydrogen burn in the LCA, the UCA, and the IRWST, as shown in Figure 3(a). In the MELCOR analysis, an NIS-type PAR was modeled to operate when the hydrogen and oxygen mole fractions reach 2 vol% and 3 vol%, respectively. After both mole fractions fall below 0.5 vol%, the PAR was assumed to stop. Also, operators can initiate the ACSS when available. Located at the top of the UCA, the ACSS uses a water source outside of the containment. Sprayed water accumulates in the refueling pool located at the bottom of the UCA.

In the SMART, ex-reactor vessel cooling (ERVC) is available to prevent RV failure when in-vessel core degradation occurs; Figure 3(b) shows a conceptual view of ERVC. Operators initiate the cavity flooding system (CFS) after SAMG entry to inject coolant into the cavity from the IRWST by gravitational force. The coolant fills up to almost half the height of the LCA annulus, so that boiling occurs in the ERVC zone by the residual heat from the lower head vessel. There is no direct heat transfer from the ERVC zone to the lower annulus, which is located outside the ERVC zone by an insulator. To avoid excessive steam condensation in the MELCOR analysis, the lower annulus was divided into several control volumes to decrease the temperature difference between the steam and water surface by simulating a thermal stratification of the water [14].

*2.4. Accident Condition.* In this research, a 2-in diameter guillotine break SBLOCA in the PSIS was considered as the initiating event; the flow path for the break is indicated as the yellow line in Figure 3(a), representing the coolant inside of the RV discharging to the upper annulus through the break area. It was assumed that the PRHRS and the PSIS are unavailable but the CFS is available during the accident. If safety systems are available, potential severe accidents can be delayed or even arrested. Although the probability is very low, this severe accident scenario was considered to analyze the containment integrity under the most conservatively defined pressurization condition.

The RV condition and the availability of the RRT and the ACSS were considered as containment condition variables. The source term as well as containment safety can be affected by the condition of the RV because fission products are released into the LCA in a SBLOCA. The status of the RV depends on the success of on-time CFS operation when the PSIS and the PRHRS are unavailable. Two different CFS initiation times after SAMG entry were considered for early and late operation: 30 min (case 0, the base case) and 72 h (case 1).

Before environmental release, fission products pass the RRT and the UCA, and thus source terms can be affected by the availability of the RRT and the ACSS. In the two above cases, the RRTs were assumed to be in a normal state with 100% water capacity, while the ACSS was unavailable. On the other hand, two other cases assumed that there is no water in the RRTs following SBLOCA occurrence (cases 3 and 4). To analyze the effect of the containment spray on the UCA condition and the source term, the ACSS was assumed to be available in two cases (cases 2 and 4). Table 1 shows the characteristics of the analysis cases.

## 3. Results and Discussion

*3.1. Source Term Estimation according to RV Condition.* Prior to the accident analysis, the steady state was simulated to validate the MELCOR input model. As shown in Table 2, the result fit well to the SMART design operating conditions. This section covers cases 0 and 1 according to the RV condition; as previously mentioned, cases 0 and 1 represent

TABLE 1: Characteristics of the analysis cases.

| Case | Initiation time of the cavity flooding system | Water capacity of the radioactive removal tank (%) | Availability of the ancillary containment spray system |
| --- | --- | --- | --- |
| 0 | Early | 100 | Unavailable |
| 1 | Late | 100 | Unavailable |
| 2 | Early | 100 | Available |
| 3 | Early | 0 | Unavailable |
| 4 | Early | 0 | Available |

Early: 30 min after SAMG entry; late: 72 h after SAMG entry.

TABLE 2: Comparison of the SMART operating conditions and MELCOR results.

| Parameter | Unit | SMART design value | MELCOR result |
| --- | --- | --- | --- |
| Core heat output | MW | 365 | 365.7 |
| Core inlet coolant flow rate | kg/s | 2507 | 2449 |
| Core inlet temperature | K | 568.7 | 585.4 |
| Core outlet temperature | K | 594.1 | 608.3 |
| Pressurizer pressure | MPa | 1.50 | 1.49 |
| Steam flow rate (per SG) | kg/s | 47.7 | 47.6 |
| Feed water flow rate (per SG) | kg/s | 47.7 | 47.7 |
| SG inlet feed water temperature | K | 503.2 | 503.0 |
| SG outlet steam pressure | MPa | 5.62 | 5.77 |

SG: steam generator.

early and late CFS initiation (30 min and 72 h after SAMG entry), respectively.

Table 3 shows the main event times in the analysis of the SBLOCA-induced severe accident. The reactor tripped by the pressurizer low-level signal following SBLOCA occurrence at 0 h; it was assumed that the reactor coolant pumps and the main feedwater pumps were halted at the same time. The collapsed liquid level in the RV decreased, as shown in Figure 4(a), so that the fuel top was exposed at 0.24 h. The core exit temperature met the SAMG entry condition of 923 K at 2.09 h. Hydrogen and fission products started to release into the containment at 2.2 h and 2.25 h, respectively. The operators initiated the ADS 30 min after SAMG entry to transport the gas inside of the RV to the UCA through the RRTs; early CFS initiation was performed at the same time in case 0. Because of the ERVC, the core support plate failure was delayed about 1 h in case 0, after which the total mass in the RV lower head rapidly increased, as shown in Figure 4(b). But, in case 1, the mass drastically decreased at 19.09 h due to RV failure. At the same time, MCCI started and the late CFS initiation was performed at 74.09 h, which is 72 h after SAMG entry.

Figure 5(a) shows the collapsed liquid level in the LCA annulus and ERVC system. In the figure, the reference level (0 m) corresponds to the bottom of the cavity (CV810 in Figure 3(a)). When operators initiate the CFS, the liquid levels in the LCA annulus and the ERVC system increase to the same level in both cases 0 and 1. The liquid level in the LCA annulus prior to CFS initiation was caused by leakage through the break. In case 1, the liquid level started to decrease due to MCCI after about 19 h. Because of the temperature stratification in the water of the LCA annulus, excessive steam condensation can be prevented in MELCOR, so that the containment pressure can be

realistically estimated. The axial and radial ablation depth of the cavity started to increase at about 36 h after the water in the cavity was depleted in case 1, as shown in Figure 5(b). The ablation stopped after late CFS initiation. As the basemat is located 3 ft below the cavity concrete, it was estimated that damage to the basemat can be prevented even with late CFS initiation.

The UCA pressure remained below the LCA pressure during the accident by the CPRSS, as shown in Figure 6(a). The containment pressure increases right after the SBLOCA occurs. But the LCA pressure decreased drastically at 2.59 h following the transport of massive steam to the UCA through the flow path connecting the SIT room and the RRT 30 min after the SAMG entry. During the transportation, most of the steam condensed in the RRT such that the UCA pressure was barely changed. In case 1, the LCA pressure started to decrease because there was no additional steam supply to the LCA after the lower plenum dry-out at 13.71 h, while the steam condensed to the heat structures and cavity water surface. However, the LCA pressure rapidly increased when the RV failed because of instantaneous water evaporation in the cavity. The final pressures of the LCA and UCA were similar in both cases. As the design pressures of the LCA and UCA are 350 kPa and 190 kPa, respectively, sufficient safety margin exists for containment failure by overpressurization.

As shown in Figure 6(b), the maximum hydrogen mole fraction in case 0 was analyzed to be about 3% in the LCA. Over time, the mole fraction decreased as the hydrogen transported to the UCA. In case 0, because the molten corium was successfully retained in vessel by the ERVC, the mole fraction was maintained in the containment until 72 h. But, in case 1, the maximum hydrogen mole fraction exceeded the critical value, 10%, in the LCA. After the water

TABLE 3: Main event times from MELCOR analysis for the small break loss-of-coolant accident in the SMART.

| Main event | Case 0 (hours) | Case 1 (hours) | Case 2 (hours) | Case 3 (hours) | Case 4 (hours) |
|---|---|---|---|---|---|
| SBLOCA occurrence | 0.00 | 0.00 | 0.00 | 0.00 | 0.00 |
| Reactor, reactor coolant pump, and main feedwater pump trip | 0.04 | 0.04 | 0.04 | 0.04 | 0.04 |
| Fuel top exposure | 0.24 | 0.24 | 0.24 | 0.23 | 0.23 |
| Fuel bottom exposure | 2.00 | 2.00 | 2.00 | 2.04 | 2.04 |
| SAMG entry | 2.09 | 2.09 | 2.09 | 2.24 | 2.24 |
| Oxidation start | 2.20 | 2.20 | 2.20 | 2.28 | 2.28 |
| Gap release start | 2.25 | 2.25 | 2.25 | 2.32 | 2.32 |
| Candling start | 2.47 | 2.47 | 2.47 | 2.62 | 2.62 |
| ADS initiation | 2.59 | 2.59 | 2.59 | 2.74 | 2.74 |
| CFS initiation (early) | 2.59 | N/A | 2.59 | 2.74 | 2.74 |
| ACSS initiation | N/A | N/A | 4.09 | N/A | 4.24 |
| Core support plate failure | 9.19 | 8.02 | 9.69 | 8.01 | 9.57 |
| Lower plenum dry-out | 16.88 | 13.71 | 18.95 | 16.64 | 16.40 |
| RV failure | N/A | 19.09 | N/A | N/A | N/A |
| MCCI start | N/A | 19.09 | N/A | N/A | N/A |
| CFS initiation (late) | N/A | 74.09 | N/A | N/A | N/A |
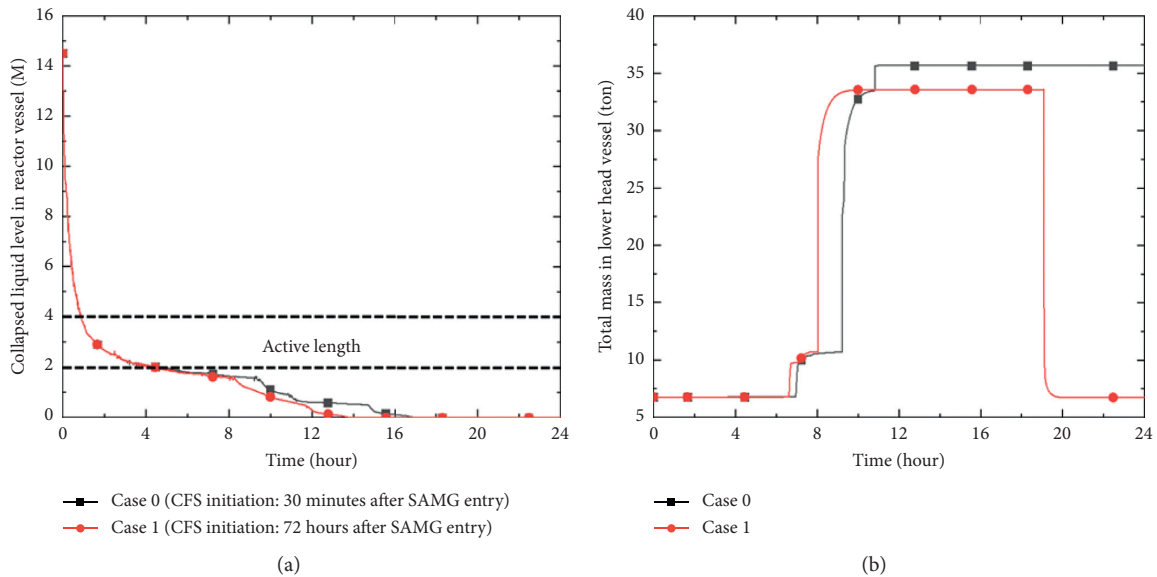


FIGURE 4: (a) Collapsed liquid level in the reactor vessel and (b) total mass in the lower head vessel.

in the cavity depleted, metals such as zirconium and steel started to oxidize, which in turn started to increase the mole fractions of hydrogen and carbon monoxide at about 36 h, as shown in Figure 6(c). Although the peak hydrogen mole fraction was about 11%, it is estimated that a hydrogen burn is very unlikely to occur because the oxygen mole fraction is too low and the steam mole fraction is too high in the LCA. The operational condition for the PARs was satisfied only in the UCA of case 1, as shown in Figure 6(d). Because the oxygen mole fraction is too low, the PAR did not operate in the LCA. Following reaction with the metals, carbon dioxide also started to increase at about 48 h when the molten corium converted from the heavy mixture (with a higher density than the metallic phase) into the light oxide (with a lower density than the metallic phase).

The results demonstrate that containment failure can be prevented considering the pressure, hydrogen mole fraction, and ablation depth. Therefore, only the design leak was considered to estimate the source term. Figure 7 shows the release fractions of the 12 classes to the environment in cases 0 and 1. The noble gases were continuously released such that their release fractions were the largest among all fission products. For all other fission products (except the noble gases), the release fractions to the environment increased until 12 h and then were maintained. The release fractions of Cs, tellurium, and CsI showed the highest values excluding the noble gases, and the values were similar in both cases. The metallic fission products that are low volatile radionuclides, such as cerium and ruthenium, were released when the gas in the RV transported to the cavity by the RV failure in case 1. Additional release of metallic fission products
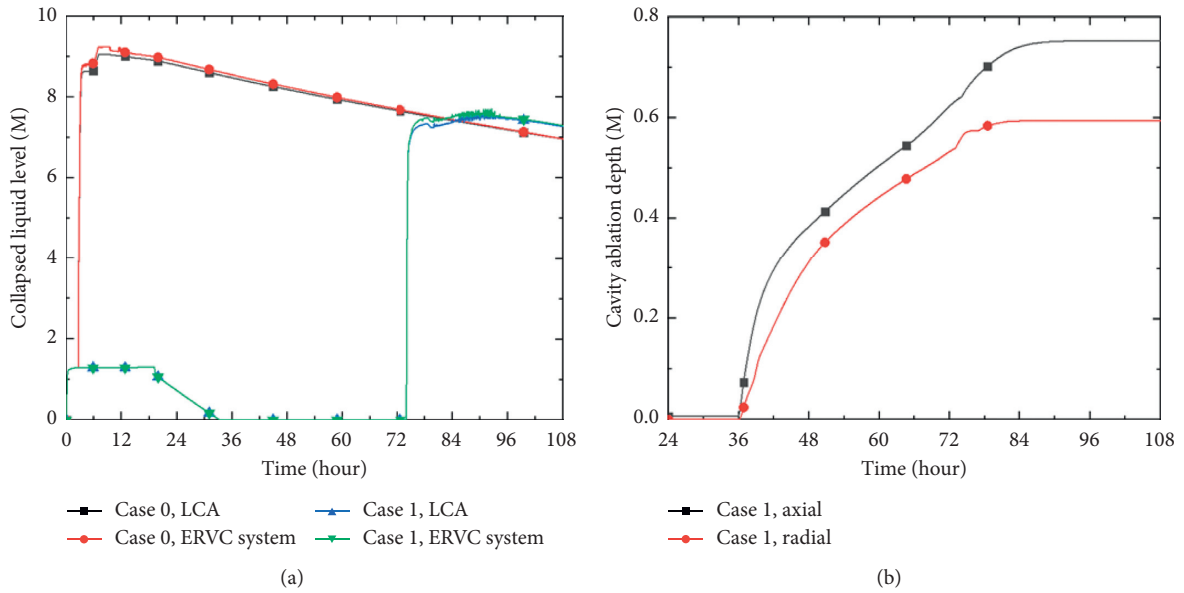
(a)



(b)

FIGURE 5: (a) Collapsed liquid level (0 m = bottom of the cavity) in the lower containment area and ex-reactor vessel cooling system; (b) ablation depths of the cavity.
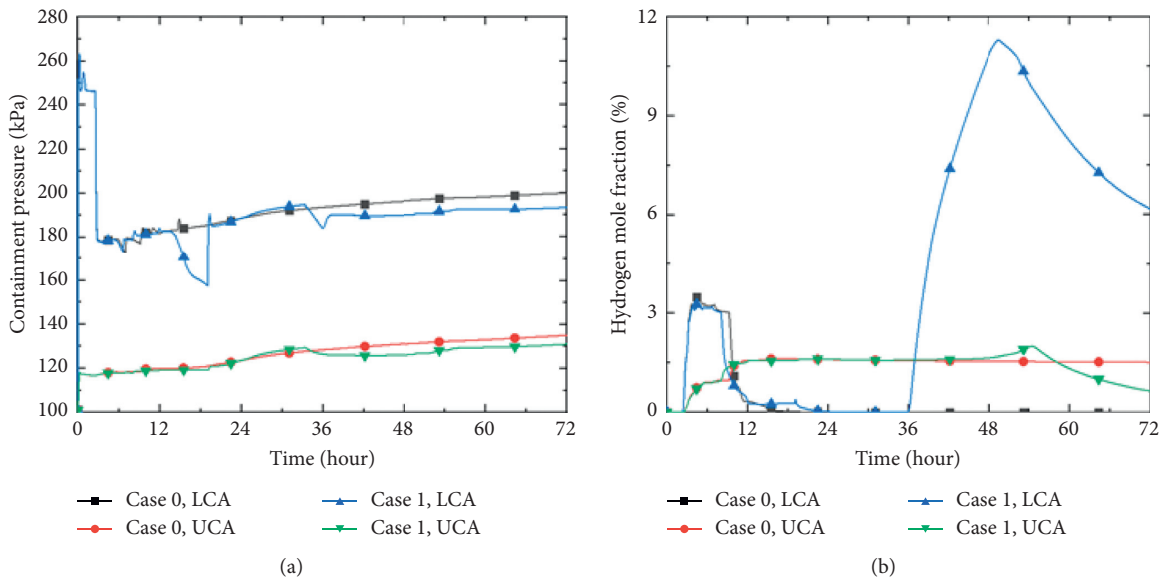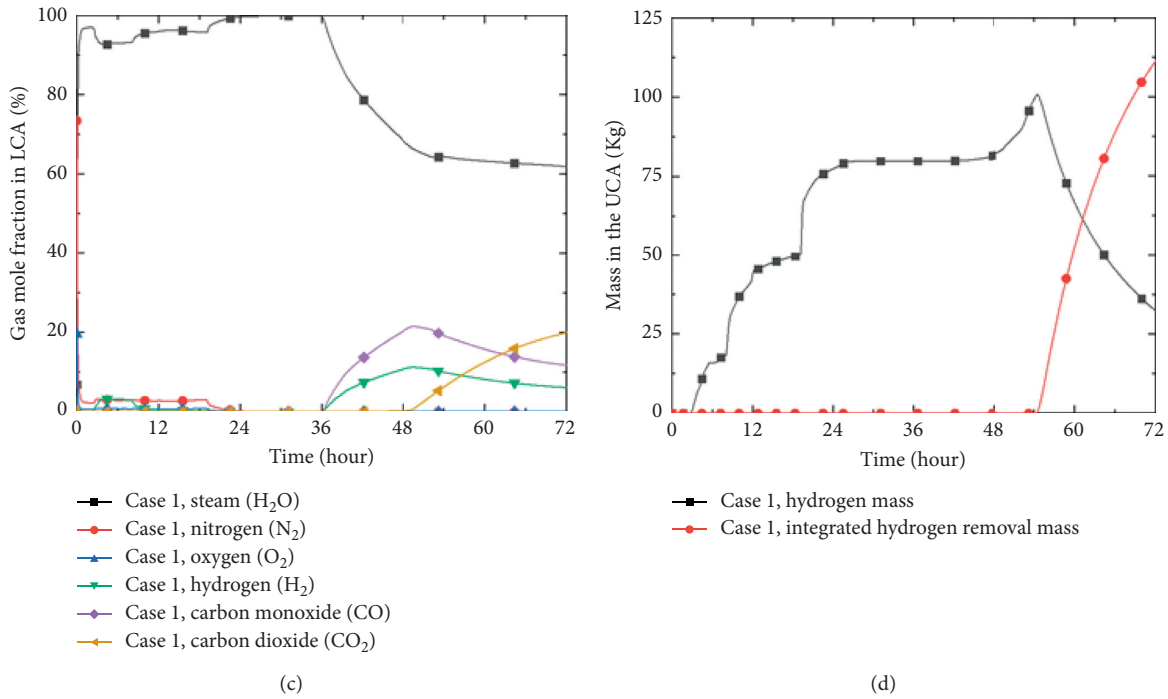


(a)



(b)

FIGURE 6: Continued.

(c)



(d)

FIGURE 6: Containment properties from the MELCOR analysis: (a) pressure, (b) hydrogen mole fraction, (c) gas mole fraction in the lower containment area, and (d) hydrogen mass and integrated hydrogen removal mass in the upper containment area.
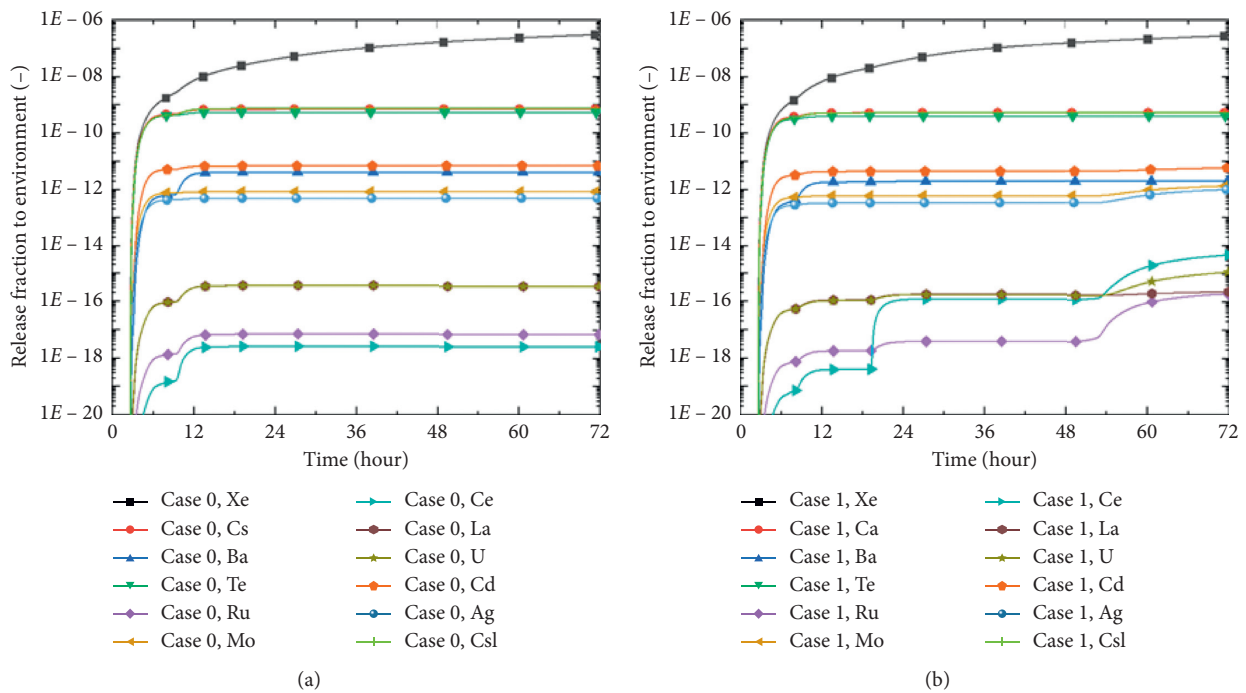


(a)



(b)

FIGURE 7: Release fraction to the environment: (a) case 0 and (b) case 1.

started after the molten corium changed to light oxide at about 48 h.

Figure 8 shows the in-containment Cs release fractions. In both cases, the release fraction to the UCA could be maintained below that to the LCA because of the RRTs. The release fraction to the LCA was higher than the release fraction to the RRTs because the accumulated total flow through the break area was larger, since the gap release started at about 2 h, as shown in Figure 9(a). The flow rate increased when the RV pressure increased in both cases, as shown in Figure 9(b). This
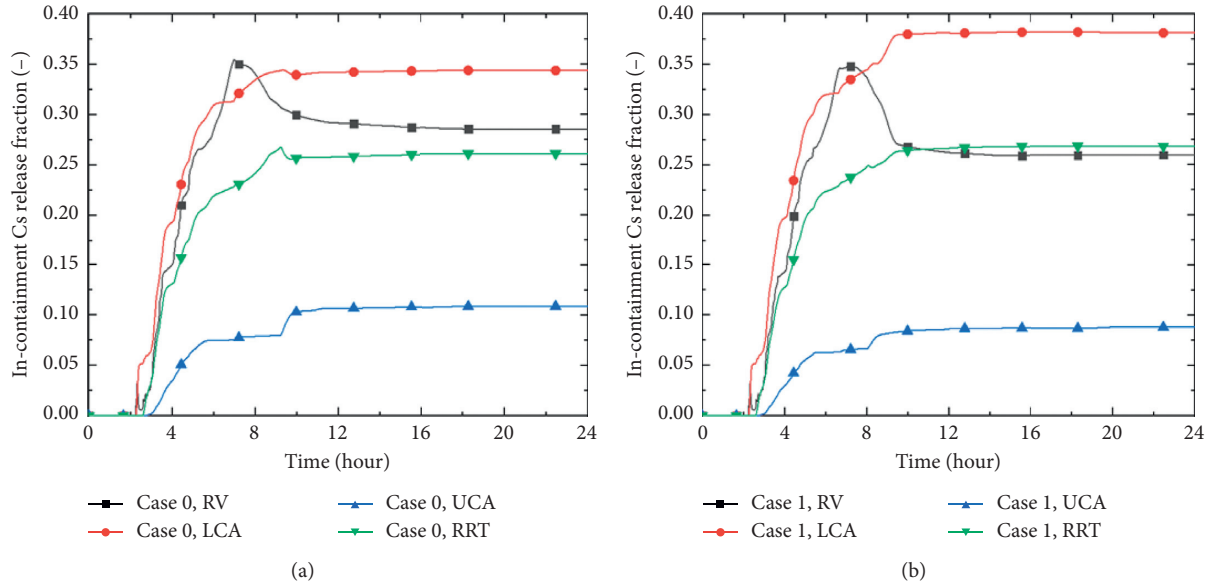
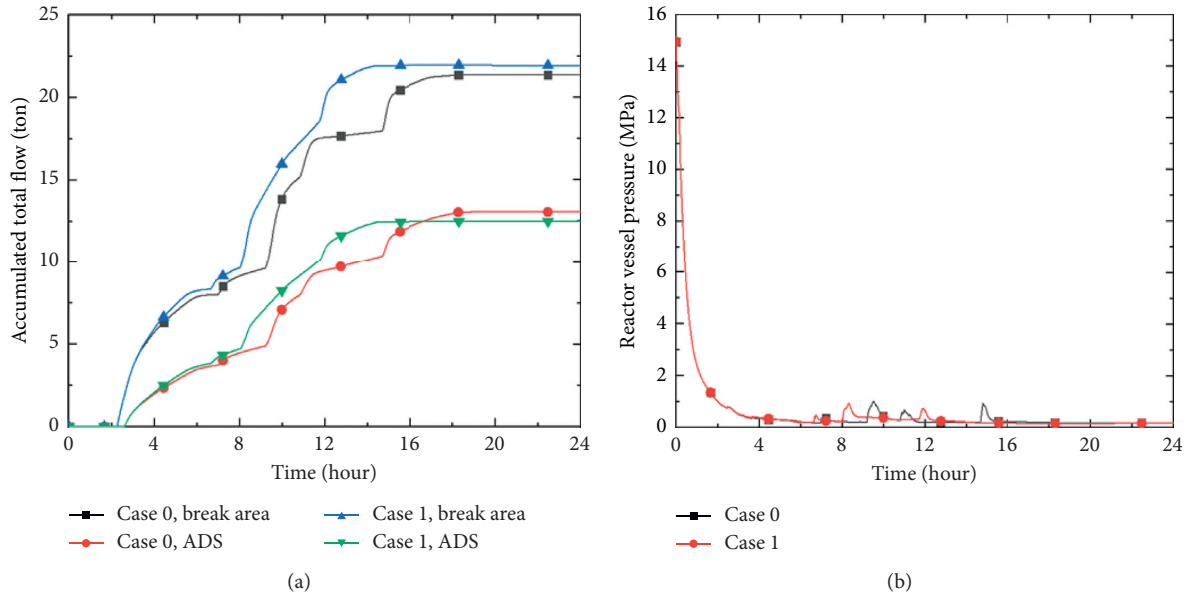Figure 8: In-containment cesium release fraction: (a) case 0 and (b) case 1.



Figure 9: (a) Total accumulated flow through the break area and the automatic depressurization system from the reactor vessel from the start of gap release; (b) pressure in the reactor vessel.

is because the steam mass in the RV increases when the core support plate fails, and convective heat transfer from the molten pool increases by degradation. About 25% of the Cs was scrubbed in the RRTs, which verifies its performance in suppressing the release of fission products.

### 3.2. Source Term Estimation according to RRT and ACSS Availability.

In this section, cases 0, 2, 3, and 4 are covered according to the availability of the RRT and the ACSS as

shown in Table 1. In cases 2 and 4, it was assumed that operators initiate the ACSS 2 h after SAMG entry, with two-hour cyclic operation assumed for the ACSS (in other words, operation cycles of two hours per cycle every two hours). In cases 3 and 4, depletion of the RRT water was assumed following accident occurrence. Due to the absence of the RRT water, the amount of residual heat removal by the IRWST increased, so that the core exit temperature can be delayed in these cases. Early CFS operation was assumed for all four cases in this section.
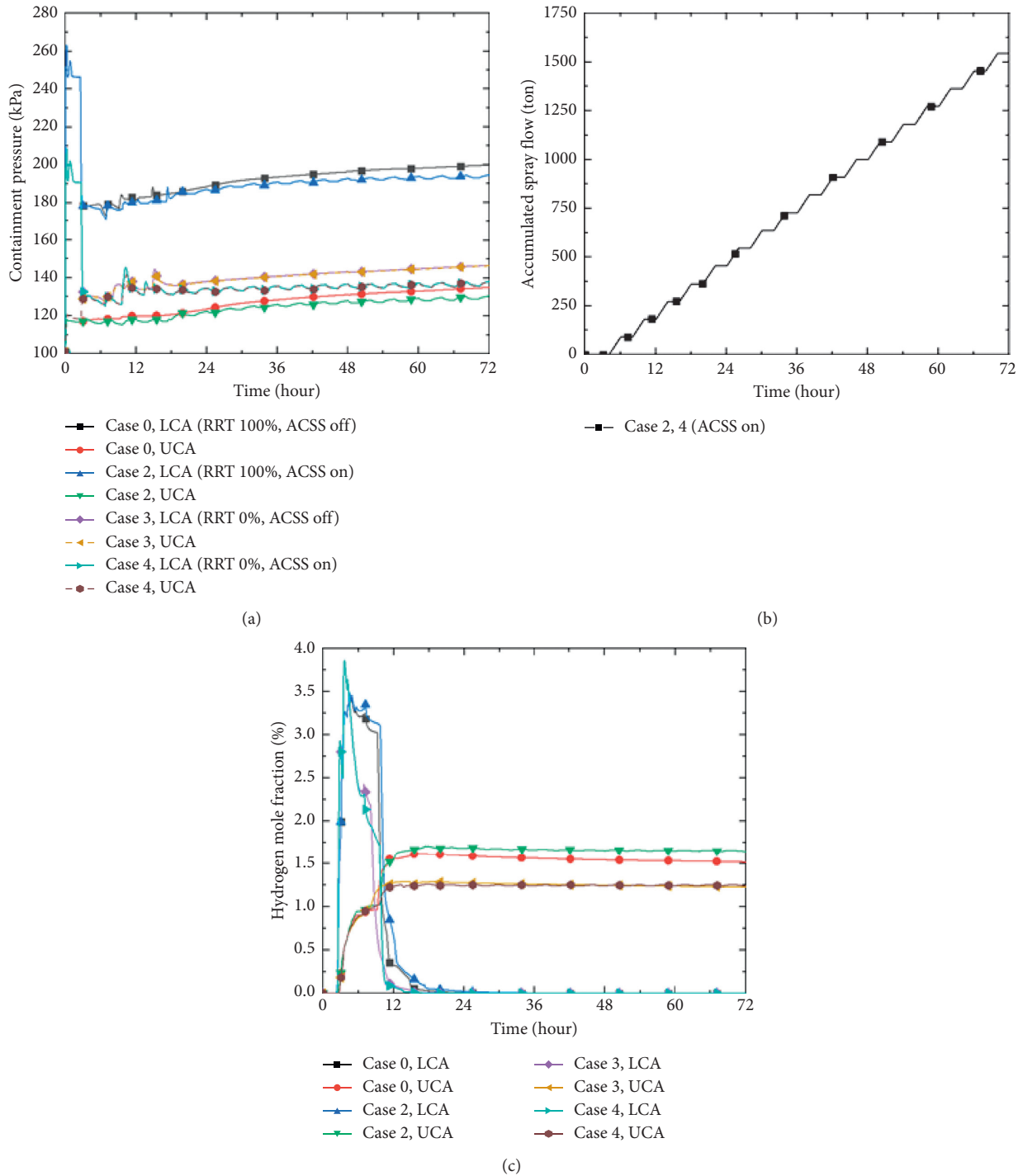
(a)

(b)



(c)

Figure 10: Containment properties from the MELCOR analysis: (a) pressure, (b) accumulated spray flow by the ancillary containment spray system, and (c) hydrogen mole fraction.

As shown in Figure 10(a), the pressures in the LCA and the UCA were the same in cases 3 and 4 because there was no water in the RRTs, which are passages between the two areas. In cases 2 and 4, as shown in Figure 10(b), the final pressure lowered with fluctuation because of ACSS operation, from which about 1,500 tons of spray flow was accumulated. The overall hydrogen mole fractions in the LCA and UCA were similar in all four cases (0, 2, 3, 4), as shown in Figure 10(c). Also, the PARs did not operate in the containment in any of these cases because the operational condition was not satisfied. As sufficient safety margins exist for containment pressure and hydrogen mole
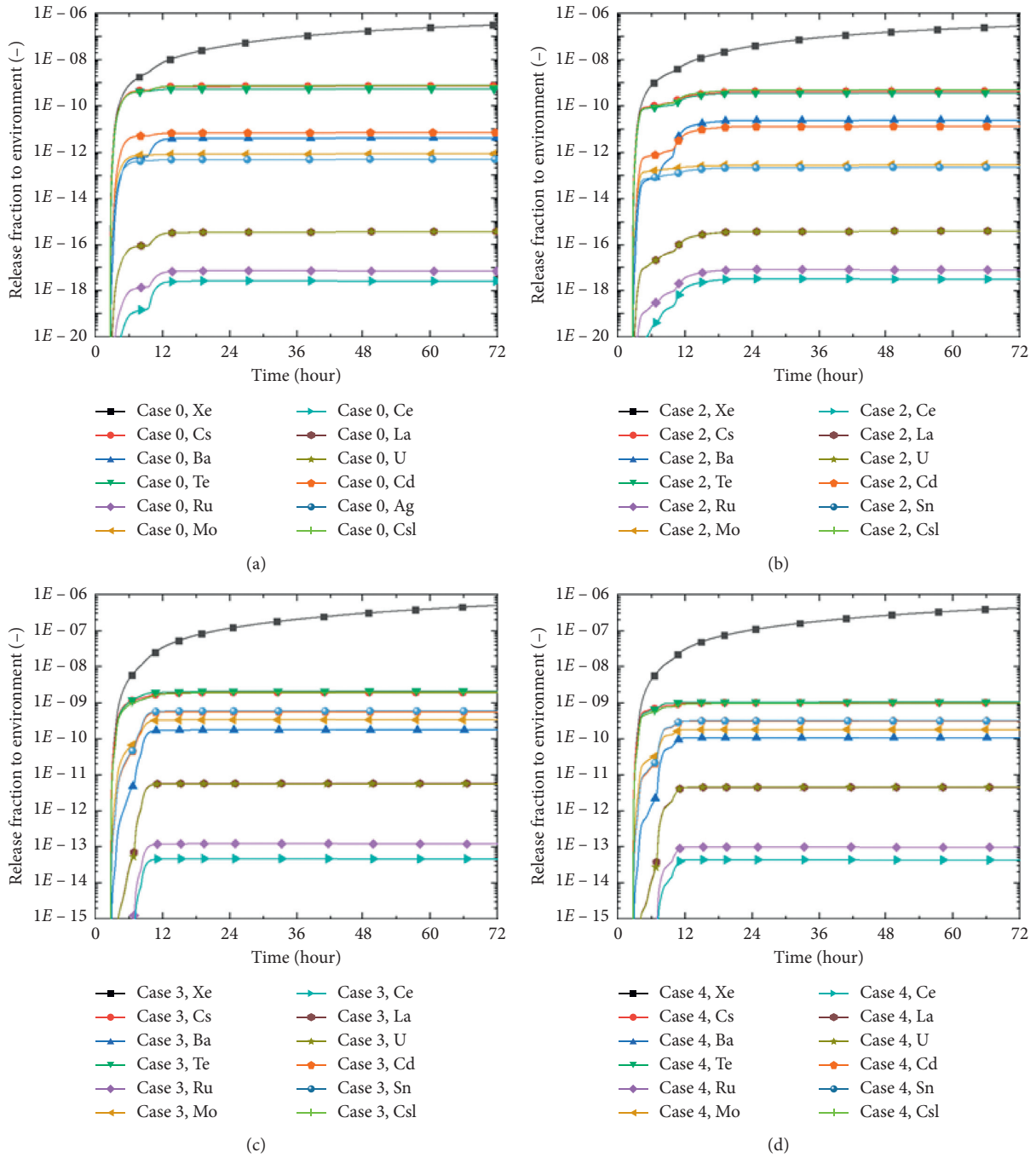
Figure 11: Release fractions to the environment: (a) case 0, (b) case 2, (c) case 3, and (d) case 4.

fraction without RV failure, containment failure can be prevented in these cases.

Figure 11 shows the release fractions of the 12 classes to the environment in cases 2–4. The behaviors of the release fractions in cases 2–4 were similar to that in case 0. The release fractions increased until 12 h and remained in all cases. The Cs release fraction in case 3 had the largest value compared to case 0—the release fraction more than doubled

in case 3. However, the release fraction can be halved if the ACSS is available. Figure 12 shows the in-containment Cs release fractions for cases 2–4. In cases 3 and 4, the release fraction to the UCA includes the release fraction to the RRTs. The in-containment Cs release fractions according to ACSS availability do not significantly differ because the sump of the sprayed water is the refueling pool located at the bottom of the UCA.
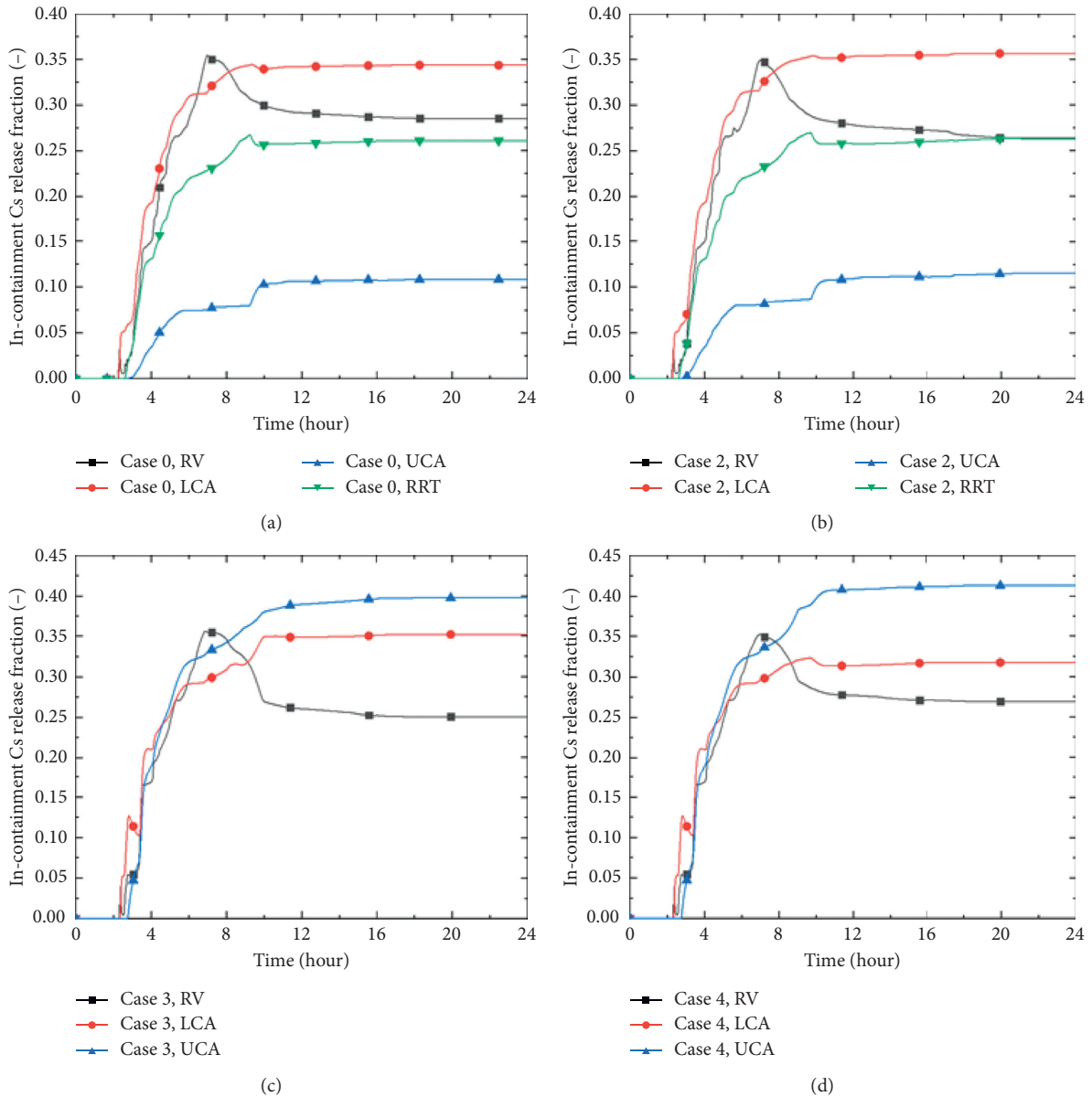
Figure 12: In-containment cesium release fractions: (a) case 0, (b) case 2, (c) case 3, and (d) case 4.

## 4. Conclusion

In this study, source term estimation under the SBLOCA-induced severe accident condition in the SMART was performed using MELCOR. First, the source term according to the RV condition was estimated. When early CFS initiation is possible (case 0 in this work), the integrity of the RV can be maintained by the ERVC for 72 h. If operators initiate the CFS 72 h after SAMG entry (case 1), MCCI occurs after RV failure. However, the integrity of the basemat can be maintained even with late CFS initiation. It was estimated that containment failure does not occur in either of these cases. Although the peak value of the hydrogen mole fraction exceeded the critical value on account of the MCCI, the oxygen mole fraction was too low and the steam mole fraction was too high to generate a hydrogen burn.

Accordingly, the source term was estimated only with the design leak. Among the 12 classes, the release fractions of those with Cs, tellurium, and CsI as representative isotopes were the highest (excluding the noble gases). Metallic fission products were additionally released by the gas transportation to the cavity when the RV fails, and the release fraction of these materials increased again, since the molten corium changed to light oxide in case 1. Although the release fractions of the metallic fission products were different, the overall source terms were similar in both cases because the release fractions of the metallic fission products are negligible compared to the release fractions of the noble gases, Cs, tellurium, and CsI. The Cs release fraction to the RRTs was about 25% in both cases.

Second, the source term according to the availability of the RRTs and the ACSS was estimated. For all cases, there

was no containment failure because the pressures and hydrogen mole fractions were lower than the critical values. The release fraction of Cs to the environment increased more than two times from the base case when there was no water in the RRTs. However, the source term could be cut in half if the ACSS is available. Accordingly, the reduction effect that the RRT and the ACSS have on the release fraction was verified through the analysis results in Section 3.2.

The maximum release fraction of Cs to the environment was analyzed to be about $2.0E-9$ when there is no water in the RRTs and the ACSS is unavailable. Based on this value, the maximum released activity of Cs-137 was calculated with the maximum core fission product inventories of SMART obtained from another study. The result was evaluated to be well below the regulatory limit of 100 TBq. As a result, this study verified that the SMART can maintain safety under the SBLOCA-induced severe accident condition. As further studies, estimation of the emergency planning zone and the radiation dose to the public based on the source term result found here can be conducted.

## Data Availability

Data used to support this study are available from the corresponding author upon request.

## Conflicts of Interest

The authors declare that they have no conflicts of interest.

## Acknowledgments

## References

[1] H. B. Delmastro, M. Markiewicz, E. Lopasso et al., "CAREM project status," *Science and Technology of Nuclear Installations*, vol. 2011, p. 1, Article ID 140373, 2011.

[2] World Nuclear Association Website, *Small Nuclear Power Reactors*, World Nuclear Association Website, London, UK, 2020, https://www.world-nuclear.org/information-library/nuclear-fuel-cycle/nuclear-power-reactors/small-nuclear-power-reactors.aspx.

[3] D. T. Ingersoll, Z. J. Houghton, R. Bromm, and C. Desportes, "NuScale small modular reactor for co-generation of electricity and water," *Desalination*, vol. 340, pp. 84–93, 2014.

[4] J. Ham, "Accident sequence analysis of a SBO in SMART100 using MELCOR," in *Proceedings of the International Workshop on Post-Fukushima Challenges on Severe Accident Mitigation and Research Collaboration*, Hotel INTERCITI, Daejeon, South Korea, November 2019.

[5] H. C. Kim, K. S. Ha, S. J. Kim et al., "Development of a Korean roadmap for technical issue resolution for fission product behavior during severe accidents," *Nuclear Engineering and Technology*, vol. 49, no. 8, pp. 1575–1588, 2017.

[6] K. Sunnevik, *Comparison of MAAP and MELCOR and Evaluation of MELCOR as a Deterministic Tool within RASTEP*, Uppsala Universitet, Uppsala, Sweden, 2014.

[7] SAND2017-0445O, *MELCOR Computer Code Manuals, Vol. 1: Primer and Users' Guide*, U.S. Nuclear Regulatory Commission, Rockville, MD, USA, 2018.

[8] SAND2017-0445O, *MELCOR Computer Code Manuals, Vol. 2: Reference Manual*, U.S. Nuclear Regulatory Commission, Rockville, MD, USA, 2018.

[9] NUREG/CR-4173, *CORSOR User's Manual*, U.S. Nuclear Regulatory Commission, Rockville, MD, USA, 1985.

[10] NUREG/CR-5765, *SPARC-90: A Code for Calculating Fission Product Capture in Suppression Pools*, U.S. Nuclear Regulatory Commission, Rockville, MD, USA, 1991.

[11] NUREG/CR-1391, *MAEROS User Manual*, U.S. Nuclear Regulatory Commission, Rockville, MD, USA, 1982.

[12] NUREG-1465, "Accident Source Terms for Light-Water Nuclear Power Plants," *U.S. Nuclear Regulatory Commission*, Rockville, MD, USA, 1995.

[13] SAND2013-6886J, *MELCOR Simulations of the Severe Accident at Fukushima Unit 3*, Sandia National Laboratories, Livermore, CA, USA, 2014.

[14] J. Ham, "Analysis on severe accident sequence in SMART100 using MELCOR," in *Cooperative Severe Accident Research Program technical review Meeting and MELCOR Code Assessment Program Meeting*, International Nuclear Information System, Vienna, Austria, August 2020.

*Research Article*

# Analysis of Fission Products' Release in Pebble-Bed High-Temperature Gas-Cooled Reactor Fuel Elements Using a Modified FRESCO II Numerical Model

**Chao Fang,**[1,2,3,4] **Chuan Li** [1,2,3] **Jianzhu Cao,**[1,2,3] **Ke Liu,**[1,2,3] **and Sheng Fang** [1,2,3]

[1]*Institute of Nuclear and New Energy Technology, Tsinghua University, Beijing 100084, China*
[2]*Collaborative Innovation Center of Advanced Nuclear Energy Technology, Beijing 100084, China*
[3]*The Key Laboratory of Advanced Reactor Engineering and Safety, Ministry of Education, Beijing 100084, China*
[4]*Lab for High Technology, Tsinghua University, Beijing 100084, China*

Correspondence should be addressed to Sheng Fang; fangsheng@tsinghua.edu.cn

The radiation safety design and emergency analysis of an advanced nuclear system highly depends on the source term analysis results. In modular high-temperature gas-cooled reactors (HTGRs), the release rates of fission products (FPs) from fuel elements are the key issue of source term analysis. The FRESCO-II code has been established as a useful tool to simulate the accumulation and transport behaviors of FPs for many years. However, it has been found that the mathematical method of this code is not comprehensive, resulting in large errors for short-lived nuclides and large time step during calculations. In this study, we used the original model of TRISO particles and spherical fuel elements and provided a new method to amend the FRESCO-II code. The results show that, for long-lived radionuclides (Cs-137), the two methods are perfectly consistent with each other, while in the case of short-lived radionuclides (Cs-138), the difference can be more than 1%. Furthermore, the matrix method is used to solve the final release rates of FPs from fuel elements. The improved analysis code can also be applied to the source term analysis of other HTGRs.

## 1. Introduction

Modular high-temperature gas-cooled reactors (HTGRs) are generally considered to have the technical characteristics of a Generation IV (Gen-IV) nuclear energy system [1]. When analyzing the emergency action and safety principles of an HTGR, it is crucial to know the source term under normal and accident conditions. Source term analysis could provide the generation, quantity, release, and radiation hazard of radionuclides in a nuclear power plant. Owing to the use of high performance fuel elements and TRISO particles, the fission products (FPs) can be effectively retained in the reactor core [2]. However, after decades of operation of the reactor, many FPs may escape from the fuel elements (with a lifetime of approximately 3 years) through permeation and diffusion effects, which has contributed to the main source of radioactivity in the primary circuit and other parts of the nuclear power plant [3, 4].

In order to calculate the amount of FPs in the primary circuit, the numerical simulation code FRESCO-II was developed at Forschungszentrum Jülich in Germany in the early 1980s by Krohn and Finken [5]. This code has been used for decades in HTGRs at Germany, China, and other countries; the results have been compared in many benchmark calculations and have been validated through experiments [6]. Based on the FRESCO-II code and other codes (FRESCO-I, PANAMA, SPATRA, and so on), the uniform and integrated code package STACY (Source Term Analysis Code System) was developed by Allelein et al. in 2010 [7]. Recently, the new simulation package FRAT for prediction and evaluation of full core fission product release was developed by Li et al. at Tsinghua University (China) [8].

All of these simulation codes are based on Fick's law of diffusion [9, 10], and the results are obtained based on different discrete methods and numerical simulation processes. After using the original model and method of the

FRESCO-II code, it has been found that there is a small error in the expression of the process coefficient. Consequently, the model is nonphysical when considering nuclide decay terms, resulting in large errors for short-lived nuclides and large time steps. In this study, all coefficients were strictly derived on the basis of the modified model. Additionally, the simulation results of the new and old models are compared herein.

## 2. Features of HTGR Fuel

The fuel element used in a HTGR is coated spherical fuel particles with a graphite substrate [11]. The research and design of coated fuel particles have gone through two stages. In the initial design, the coated fuel particle structure is of Bi-isotropic (BISO) type, i.e., a loose and a dense pyrolytic carbon layer on the outer coating of the active core. However, after many irradiation experiments and safety tests, the BISO fuel particle gradually exposed its structural shortcomings; these were mainly reflected in the high level of heavy metal contamination during the coating deposition and the low retention ability for certain metal FPs (such as strontium). Based on the BISO fuel particle, the tri-isotropic (TRISO) fuel particle is designed. The main advantage of TRISO fuel particles is their excellent retention ability for various radioactive FPs. Experiments have shown that the integrity of the TRISO structure can be maintained at temperatures below 1600°C.

Considering a pebble-bed modular HTGR as an example, a spherical fuel element with a diameter of 60 mm was used (shown in Figure 1). Each fuel element contains approximately 12,000 TRISO fuel particles consisting of five parts: (1) an enriched UO2 kernel surrounded by subsequent layers, (2) a loose pyrolytic carbon (buffer) layer, (3) an inner pyrolytic carbon (IPyC) layer, (4) silicon carbide (SiC), and finally, (5) an outer pyrocarbon (OPyC) layer [11].

## 3. Transport Model of FPs

The main transport process of FPs in the fuel elements is their diffusion in various materials (shown in Figure 2) [9]. For intact TRISO fuel particles, FPs must diffuse through all coating layers and then through the graphite matrix before entering the coolant. For the failure particles, the FPs can enter the graphite matrix directly. In addition, the FPs produced by uranium contamination in graphite grains are considered to be the same as failure particles.

If the fuel element, TRISO particles, and graphite grains are regarded as uniform spheres, the diffusion of FPs in these media can be described by the same equation. According to Fick's diffusion law, the release fractions of FPs from the spherical fuel elements can be calculated using the following diffusion equation [12]:

$$\frac{\partial c}{\partial t} = D(T)\left(\frac{\partial^2 c}{\partial t^2} + \frac{2}{r} \cdot \frac{\partial c}{\partial t}\right) + Q - \lambda C, \qquad (1)$$

where $C$ is the FP concentration in the diffusion medium (in atoms/cm$^3$) and can be obtained from the inventory, $t$ is the
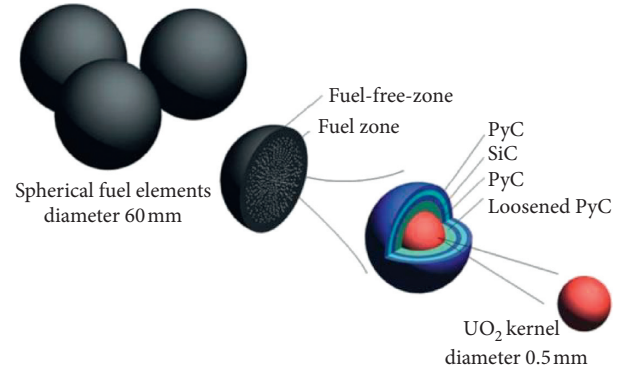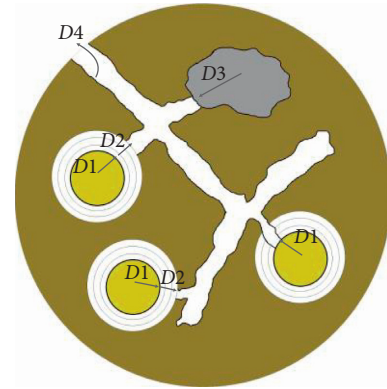


Figure 1: The spherical fuel element of HTGR.



$D1$: diffusion in UO$_2$ kernel
$D2$: diffusion in coating layer
$D3$: diffusion in graphite grains
$D4$: diffusion in graphite matrix

Figure 2: Diffusion model of FPs.

time (in s), $r$ is the spatial coordinate (in cm), $Q$ is the production rate of FPs (in atom/cm$^3$ • s), $\lambda$ is the decay constant of nuclide (in s$^{-1}$), and $D(T)$ is the diffusion coefficient (in cm$^2$/s) depending on temperature $T$ (in K) and activation energy $E$ (in J/mol) given by the following equation:

$$D(T) = D_0 \cdot \exp\left(-\frac{E}{R \cdot T}\right), \qquad (2)$$

where $R$ is the ideal gas constant ($R = 8.3143$ J/(mol·K)) and $D_0$ is the diffusion frequency factor (in cm$^2$/s). The corresponding boundary condition can be expressed as

$$-D\frac{\partial c}{\partial r}\bigg|_{r=r_p} = \beta\left(C_{rp} - C_{gr}\right), \qquad (3)$$

where $\beta$ is the interface diffusion between different materials, $C_{rp}$ is the concentration of FPs on the surface of the fuel element, and $C_{gr}$ is the average concentration of FPs in the helium outside the fuel element.

## 4. Numerical Simulation

Theoretically, the concentration at any time and position can be obtained by solving equations (1)–(3). However, the

explicit expression of $C(r,t)$ is usually very complex and difficult to solve [13].

To address this challenge, the numerical simulation method is used in the FRESCO-II code and other related codes [14]. In this method, the whole sphere is divided into $N$ thin layers of spherical shell with a volume of $V_i$ ($i = 1/2, \dots N$) (presented in Figure 3(a)).

Considering that the concentration at the $i^{\text{th}}$ spherical shell is $C_i$ and assuming that the concentration is a linear function of radius $r$, the concentration between two adjacent spherical shells can be expressed as follows (shown in Figure 3(b)):

$$c = c_i + \frac{c_{i+1} - c_i}{r_{i+1} - r_i}(r - r_i). \quad (4)$$

In particular, assuming that the concentration distribution is a quadratic curve for the central sphere because the concentration gradient is zero at the central point, the concentration can be derived as follows:

$$c = c_N - 2\frac{c_{N+1} - c_N}{r_N}(r - r_N) - \frac{c_{N+1} - c_N}{r_N^2}(r - r_N)^2, \quad (5)$$

where $c_{N+1}$ represents the concentration at the central point. For the $i^{\text{th}}$ spherical shell, the mass conservation equation is as follows:

$$\frac{d}{dt}\int_{V_i} c \cdot dV = Q \cdot V_i - \lambda \int_{V_i} c \cdot dV - J_i \cdot F_i + J_{i+1} \cdot F_{i+1}, \quad (6)$$

where the left side of this equation represents the concentration change during $dt$ time. The right side represents the various sources of concentration change, i.e., the generation of fission with rate $Q$, the disappearance of decay, and the diffusion from the inner layer into the target layer and from the target layer into the outer layer, respectively. According to Fick's first diffusion law, the diffusion rate per unit area $J$ can be expressed as

$$J_i = -D_i\frac{c_{i+1} - c_i}{r_{i+1} - r_i}, \quad (i \neq N),$$
$$J_N = -2D_N\frac{c_{N+1} - c_N}{r_{N+1} - r_N}, \quad (i = N). \quad (7)$$

Then, we can discretize the mass conservation equation (6) using the average change rates instead of instantaneous change rates. For the left side of equation (6), it can be approximated by replacing $dt$ with $\Delta t$ as follows:

$$\frac{d}{dt}\int_{V_i} c \cdot dV = \frac{1}{\Delta t}\left[\int_{V_i} c^{k+1} \cdot dV - \int_{V_i} c^k \cdot dV\right], \quad (8)$$

where the superscript index $k$ represents the time step; a larger value corresponds to a later time point.

It should be emphasized that, until this step, all the symbols and equations are the same as the ones in FRESCO-II code. However, the next derivation proposes amendments to the FRESCO-II code for the right side of equation (6). In the FRESCO-II code, the concentration appearing on the right side is set to be a future time value, i.e., the top index is

$k + 1$. Obviously, this assumption is nonphysical because the concentrations in each spherical shell are all changing dynamically. Therefore, a new method is proposed through using the time average concentrations instead of future time concentrations; this is also consistent with the treatment of the left side of equation (6). Then, the expression is derived as follows:

$$Q \cdot V_i - \lambda \int_{V_i} c \cdot dV - J_i \cdot F_i + J_{i+1} \cdot F_{i+1}$$
$$= Q \cdot V_i - \frac{\lambda}{2}\left(\int_{V_i} c^{k+1} \cdot dV + \int_{V_i} c^k \cdot dV\right) \quad (9)$$
$$- \frac{1}{2}\left(J_i^{k+1} + J_i^k\right) \cdot F_i + \frac{1}{2}\left(J_{i+1}^{k+1} + J_{i+1}^k\right) \cdot F_{i+1}.$$

From the combination of equations (6)–(9), the new equation can be reorganized as

$$a_{i+1}c_i^{k+1} + b_{i+1}c_{i+1}^{k+1} + d_{i+1}c_{i+2}^{k+1} = e_{i+1}, \quad (i = 1, 2, 3, \dots, N-1). \quad (10)$$

The coefficients are given as follows:

$$a_{i+1} = \gamma_i\left(1 + \frac{1}{2}\lambda\Delta t\right) + \frac{1}{2}D_i\frac{F_i}{V_i}\frac{\Delta t}{r_{i+1} - r_i}, \quad (11)$$

$$b_{i+1} = (1 - \gamma_i) \times \left(1 + \frac{1}{2}\lambda\Delta t\right) - \frac{1}{2}D_i\frac{F_i}{V_i}\frac{\Delta t}{r_{i+1} - r_i}$$
$$- \frac{1}{2}D_{i+1}\frac{F_{i+1}}{V_i}\frac{\Delta t}{r_{i+2} - r_{i+1}}, \quad (12)$$

$$d_{i+1} = \frac{1}{2}D_{i+1}\frac{F_{i+1}}{V_i}\frac{\Delta t}{r_{i+2} - r_{i+1}}, \quad (13)$$

$$e_{i+1} = \left[\gamma_i\left(1 - \frac{1}{2}\lambda\Delta t\right) - \frac{1}{2}D_i\frac{F_i}{V_i}\frac{\Delta t}{r_{i+1} - r_i}\right]c_i^k$$
$$+ \left[(1 - \gamma_i)\left(1 - \frac{1}{2}\lambda\Delta t\right) + \frac{1}{2}D_i\frac{F_i}{V_i}\frac{\Delta t}{r_{i+1} - r_i}\right.$$
$$\left. + \frac{1}{2}D_{i+1}\frac{F_{i+1}}{V_i}\frac{\Delta t}{r_{i+2} - r_{i+1}}\right]$$
$$\cdot (1 - \gamma_i)c_{i+1}^k - \frac{1}{2}D_{i+1}\frac{F_{i+1}}{V_i}\frac{\Delta t}{r_{i+2} - r_{i+1}}c_{i+2}^k + Q_i\Delta t, \quad (14)$$

$$\gamma_i = 1 - \frac{3}{r_{i+1}^3 - r_i^3} \cdot \frac{1}{r_{i+1} - r_i}\left[\frac{r_{i+1}^4 - r_i^4}{4} - \frac{r_{i+1}^3 r_i - r_i^4}{3}\right]. \quad (15)$$

Notably, equation (15) must be identical to that in the FRESCO-II code; nevertheless, the incorrect subscript index i-1 of the radius cubic in the rightmost fraction appeared in the FRESCO-II code.

The two boundary conditions for the outermost shell contact with the environment and the central shell can be expressed as follows:
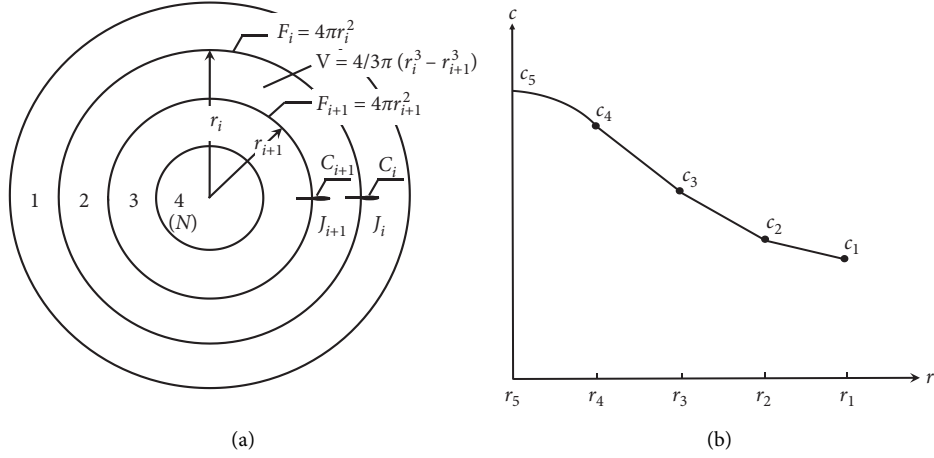
FIGURE 3: (a) $N$ layers of thin spherical shell and (b) concentration distributions.

$$-D_1 \frac{c_2^{k+1} - c_1^{k+1}}{r_2 - r_1} = \beta\left(c_1^{k+1} - c_{\text{env}}\right)$$

$$\Longrightarrow \left(\beta - \frac{D_1}{r_2 - r_1}\right)c_1^{k+1} + D_1 \cdot \frac{1}{r_2 - r_1} \cdot c_2^{k+1}$$

$$\Longrightarrow b_1 c_1^{k+1} + d_1 c_2^{k+1} = e_1,$$

$$a_{N+1} = \gamma_N\left(1 + \frac{1}{2}\lambda\Delta t\right) + \frac{1}{2}D_N \frac{F_N}{v_N} \cdot \frac{2\Delta t}{-r_N},$$

$$b_{N+1} = (1 - \gamma_N)\left(1 + \frac{1}{2}\lambda\Delta t\right) - \frac{1}{2}D_N \frac{F_N}{v_N},$$

$$d_{N+1} = 0,$$

$$e_{N+1} = \left[\gamma_N\left(1 - \frac{1}{2}\lambda\Delta t\right) - \frac{1}{2}D_N \frac{F_N}{v_N} \frac{2\Delta t}{-r_N}\right]c_N^k$$

$$+ \left[(1 - \gamma_i)\left(1 - \frac{1}{2}\lambda\Delta t\right) + \frac{1}{2}D_N \frac{F_N}{v_N} \frac{2\Delta t}{-r_N}\right]c_{N+1}^k$$

$$+ Q_N \Delta t,$$

$$\gamma_N = 0.6.$$

$$(16)$$

Equation (10) is a recurrence relation for both time and space dimensions and can be further represented in the matrix form as follows:

$$\mathbb{M} \cdot \mathbb{C}^{k+1} = \mathbb{E}^k, \qquad (17)$$

$$\mathbb{M} = \begin{bmatrix} b_1 & d_1 & 0 & & & & \\ a_2 & b_2 & d_2 & \cdots & & & 0 \\ 0 & a_3 & b_3 & & & & \\ \vdots & & & \ddots & & & \vdots \\ & & & & b_{N-1} & d_{N-1} & 0 \\ 0 & & \cdots & & a_N & b_N & d_N \\ & & & & 0 & a_{N+1} & b_{N+1} \end{bmatrix}, \qquad (18)$$

TABLE 1: Parameters of fuel particles in HTR-PM.

| Parameter | Normal data |
|---|---|
| Diameter of kernel | $500\,\mu\text{m}$ |
| Thickness of buffer layer | $95\,\mu\text{m}$ |
| Thickness of OPyC layer | $40\,\mu\text{m}$ |
| Thickness of IPyC layer | $40\,\mu\text{m}$ |
| Thickness of SiC layer | $35\,\mu\text{m}$ |
| Diameter of graphite grain | $15\,\mu\text{m}$ |
| Failure fraction of TRISO at objective burn-up | $2.60E - 04$ |
| Natural uranium contamination of fuel elements | $7.00E - 07$ |

TABLE 2: Diffusion coefficients.

| | Kernel | Buffer layer | IPyC | SiC | OPyC |
|---|---|---|---|---|---|
| $D_0$ (cm²/s) | $5.6E - 04$ | $1.0E - 08$ | $6.3E - 04$ | $1.0E - 14$ | $6.3E - 04$ |
| $E$ (J/mol) | $2.1E + 05$ | $0$ | $2.2E + 05$ | $1.0E + 05$ | $2.2E + 05$ |

$$\mathbb{C}^{k+1} = \left(c_1, c_2, \ldots, c_{N+1}\right)^{\text{T}}, \qquad (19)$$

$$\mathbb{E}^k = \left(e_1, e_2, \ldots, e_{N+1}\right)^{\text{T}}. \qquad (20)$$

Equation (17) has a unique solution because the matrix $\mathbb{M}$ is full rank. Furthermore, the elements of the matrix $\mathbb{M}$ are all time independent, i.e., they are only related to the space index and can be determined by geometric parameters. The vector $\mathbb{E}^k$ is a function of the space index and the concentrations in past time points. The unknown vector $\mathbb{C}^{k+1}$ is our target concentration in the future time point, which can be obtained by solving the matrix equation (17) as follows:

$$\mathbb{C}^{k+1} = \mathbb{M}^{-1} \cdot \mathbb{E}^k. \qquad (21)$$

This equation indicates that any concentrations in any future time point can be recursively solved when an initial concentration state is given.

Table 3: Comparison of two methods for Cs-137 fractional release rates from a pebble.

| Temperature (°C) | 600 | 700 | 800 | 900 | 1000 | 1100 | 1200 | 1300 | 1400 | 1500 | 1600 |
|---|---|---|---|---|---|---|---|---|---|---|---|
| FRESCO-II ($s^{-1}$) | $3.9192E - 16$ | $1.7100E - 15$ | $6.5096E - 14$ | $6.3373E - 13$ | $2.4107E - 12$ | $2.3764E - 10$ | $1.5134E - 09$ | $3.9838E - 09$ | $7.1964E - 09$ | $9.7246E - 09$ | $1.0717E - 08$ |
| FERRA ($s^{-1}$) | $3.9198E - 16$ | $1.7096E - 15$ | $6.5130E - 14$ | $6.3414E - 13$ | $2.3990E - 12$ | $2.3774E - 10$ | $1.5145E - 09$ | $3.9864E - 09$ | $7.2005E - 09$ | $9.7284E - 09$ | $1.0718E - 08$ |
| Ratio | 0.9998 | 1.0002 | 0.9995 | 0.9994 | 1.0049 | 0.9996 | 0.9993 | 0.9993 | 0.9994 | 0.9996 | 0.9999 |

TABLE 4: Comparison of two methods for Cs-138 fractional release rates from a pebble.

| Temperature (°C) | 600 | 700 | 800 | 900 | 1000 | 1100 | 1200 | 1300 | 1400 | 1500 | 1600 |
|---|---|---|---|---|---|---|---|---|---|---|---|
| FRESCO-II $(s^{-1})$ | $1.6609E-15$ | $2.1412E-14$ | $1.6480E-13$ | $7.8264E-13$ | $2.3831E-12$ | $5.3521E-12$ | $1.0020E-11$ | $1.6930E-11$ | $3.1376E-11$ | $8.9169E-11$ | $3.0714E-10$ |
| FERRA $(s^{-1})$ | $1.6609E-15$ | $2.1412E-14$ | $1.6480E-13$ | $7.8264E-13$ | $2.3831E-12$ | $5.3521E-12$ | $1.0027E-11$ | $1.7014E-11$ | $3.1707E-11$ | $8.9918E-11$ | $3.0952E-10$ |
| Ratio | 1.0000 | 1.0000 | 1.0000 | 1.0000 | 1.0000 | 1.0000 | 0.9993 | 0.9951 | **0.9896** | 0.9917 | 0.9923 |

## 5. Results and Discussion

The numerical simulation method introduced in Section 4 has been implemented in Python and is named Fuel Element Release Rate Analysis (FERRA) Code. Considering the HTR-PM (high-temperature gas-cooled reactor-pebble bed modules) fuel element as an example, a series of comparative calculations are performed in this study. The main parameters of the HTR-PM are listed in Table 1 [2].

The kernel and the four-layer coating materials are separated into 39 thin spherical shells in both the FRESCO-II and FERRA codes. Two cesium isotopes, Cs-137 and Cs-138 (with a decay constant of approximately $7.3E - 10\,\mathrm{s}^{-1}$ and $3.6E - 04\,\mathrm{s}^{-1}$, respectively), were used as an example to compare the differences between the results of the two methods. The diffusion coefficients of Cs in each material are listed in Table 2 [11].

Based on these parameters, after a 25,400 h burn-up (3 years average life time of fuel element), the fractional release rates of Cs-137 and Cs-138 from a pebble over the temperature range from 600°C to 1600°C are calculated and presented in Tables 3 and 4.

The results show that, for the long-lived radionuclide Cs-137, the two methods are perfectly consistent with each other at all temperatures with an error less than 1%. However, the case for the short-lived radionuclide Cs-138 is slightly different. A maximum of more than 1% error occurred when the temperature was higher than 1200°C. Furthermore, the release rates are overall underestimated in the FRESCO-II code; this can be attributed to the underestimation of the interlayer transport rates.

## 6. Conclusions

Thus far, the FRESCO-II code and its successor provided powerful simulation tools for handling the FP release rates in HTGR. Based on reliable release rates, the source term analysis could be credible and safety design and emergency evaluation could be performed.

In order to improve the reliability of the source term analysis codes, we used the original model and derivation process of the FRESCO-II code. An index error has been identified, and a new treatment for transport rates is proposed. After the code implementation, the new simulation code FERRA is developed, and a series of tests are performed. The results show that the FRESCO-II and FERRA codes are perfectly consistent with each other for both long-lived and short-lived radionuclides. Another valuable finding is that the release rates are overall underestimated in the FRESCO-II code, which suggests that the FERRA results are more conservative. As a conclusion, continuous improvements to computing tools can make a great contribution to the design of pebble-bed HTGRs.

## Data Availability

All the data used to support the findings of the study are obtained from open source literatures and all the references cited within the article.

## Disclosure

The contents of this manuscript are not now under consideration for publication elsewhere.

## Conflicts of Interest

The authors declare that they have no conflicts of interest.

## Authors' Contributions

All authors of this manuscript have directly participated in planning, execution, and/or analysis of this study.

## Acknowledgments

## References

[1] C. Fang, R. Morris, and F. Li, "Safety features of high temperature gas cooled reactor," *Science and Technology of Nuclear Installations*, vol. 2017, Article ID 9160971, 3 pages, 2017.

[2] Z. Zhang, Y. Dong, F. Li et al., "The Shandong Shidao Bay 200 MW e high-temperature gas-cooled reactor pebble-bed module (HTR-PM) demonstration power plant: an engineering and technological innovation," *Engineering*, vol. 2, no. 1, pp. 112–118, 2016.

[3] A. F. Michael, E. D'Agata, and X. Raepsaet, "Is tritium an issue for high temperature reactors?" *Nuclear Engineering and Design*, vol. 306, pp. 160–169, 2016.

[4] Y. Liu and C. Jianzhu, "Fission product release and its environment impact for normal reactor operations and for-relevant accidents," *Nuclear Engineering and Design*, vol. 218, no. 1, pp. 81–90, 2002.

[5] H. Krohn and R. Finken, "FRESCO-II: a computer program for analysis of fission product release from spherical HTR fuel element in irradiation and annealing experiments," Internal Report JUEL-SPEZ--212, Forschungszentrum Jülich, Jülich, Germany, 1983.

[6] K. Verfondern, J. Cao, T. Liu, and H.-J. Allelein, "Conclusions from V&V studies on the German codes PANAMA and FRESCO for HTGR fuel performance and fission product release," *Nuclear Engineering and Design*, vol. 271, pp. 84–91, 2014.

[7] H.-J. Allelein, S. Kasselmann, A. Xhonneux, and S.-C. Herber, "Progress on the development of a fully integrated HTR code package," *Nuclear Engineering and Design*, vol. 251, pp. 400–406, 2012.

[8] J. Li, D. She, and L. Shi, "Status of development of an integrated source term analysis code package for HTGR," in *Proceedings of the HTR 2018*, Warsaw, Poland, October 2018.

[9] J. Crank, *The Mathematics of Diffusion*, Oxford University Press, London, UK, 1956.

[10] W. Jost, *"Diffusion in Solids, Liquids, Gases" (3rd Printing with Addendum)*, Academic Press, New York, NY, USA, 1960.

[11] IAEA, "Fuel performance and fission product behavior in gas cooled reactors," Report IAEA-TECDOC-978, International Atomic Energy Agency, Vienna, Austria, 1997.

[12] C. Yang, C. Fang, J. Zhang et al., "Study on cumulative fractional release of radionuclides in HTGR fuel particles,"

*Nuclear Science and Techniques*, vol. 63, no. 3, Article ID 032802, 2014.

[13] C. Tian, L. Sun, and C. Fang, "Exact solutions to the diffusion process of fission products in the TRISO fuel particles of pebble bed HTRs: case study of137Cs and134Cs," *Nuclear Science and Engineering*, vol. 175, no. 2, pp. 204–211, 2013.

[14] H. Krohn and R. Finken, "FRESCO-II: Ein Rechenprogramm zur Berechnung der Spaltprodukt freisetzung aus Kugelförmigen HTR-Brennelementen in Bestrahlungs- und Ausheizexperimenten," Jül-Spez-212, Jülich Research Center, Julich, Germany, 1983.